ERDC/CERL CR-18-1

US Army Corps
of Engineers®
Engineer Research and
Development Center

ERDC
INNOVATIVE SOLUTIONS
for a safer, better world

DoD Corrosion Prevention and Control Program

Laboratory Investigation of Natural Cementation Road Surfacing for Corrosion Control of Aluminum on Army Vehicles

Contractor's Supplemental Report for Project F10-AR06

Phillip S.K. Ooi and Michelle K. Coskey

April 2018

Construction Engineering
Research Laboratory

The U.S. Army Engineer Research and Development Center (ERDC) solves the nation's toughest engineering and environmental challenges. ERDC develops innovative solutions in civil and military engineering, geospatial sciences, water resources, and environmental sciences for the Army, the Department of Defense, civilian agencies, and our nation's public good. Find out more at www.erdc.usace.army.mil.

To search for other technical reports published by ERDC, visit the ERDC online library at http://acwc.sdp.sirsi.net/client/default.

Laboratory Investigation of Natural Cementation Road Surfacing for Corrosion Control of Aluminum on Army Vehicles

Contractor's Supplemental Report for Project F10-AR06

Phillip S.K. Ooi and Michelle K. Coskey

University of Hawai'i at Manoa
Department of Civil and Environmental Engineering
2540 Dole Street
Honolulu, HI 96822

Final report

Prepared for Office of the Secretary of Defense (OUSD(AT&L))
3090 Defense Pentagon
Washington, DC 20301-3090

Under Agreement W9132T-09-2-0022 "Laboratory Investigation of Natural Cementation Road Surfacing for Corrosion Control of Aluminum on Army Vehicles"

Monitored by Construction Engineering Research Laboratory
U.S. Army Engineer Research and Development Center
Champaign, IL 61822

Abstract

The Department of Defense (DoD) operates a massive fleet of ground vehicles in many corrosive environments. Rutting and erosion of unpaved roadways in training areas damage vehicles and contribute to dust brownouts. Moisture, soil, and grit deposits on surfaces and undercarriages accelerate corrosion and increase maintenance requirements. These problems could be greatly mitigated by advanced road stabilization materials and practices. A geopolymer material was studied for demonstration and validation on unpaved military roads at Pohakuloa Training Area (PTA), HI, under DoD Corrosion Prevention and Control Project F10-AR06. To support that work, the University of Hawai'i at Manoa performed a series of laboratory tests to characterize the geopolymer and its constituent materials, such as fly ash and slag, and the resulting cementitious material when blended with lime, soda ash, basalt aggregate, and water.

Material characterization and mechanical testing was performed to assess the basalt aggregate. Geopolymer mechanical properties were then measured in unconfined compression and four-point bending tests. Microstructural and mineralogical characteristics of the constituents and geopolymer were characterized using x-ray fluorescence, scanning electron microscopy with energy dispersive spectroscopy, and x-ray diffraction. The 28-day geopolymer unconfined compressive strengths averaged about 2,000 psi and the modulus of rupture averaged about 290 psi.

TABLE OF CONTENTS

LIST OF FIGURES

LIST OF TABLES

Foreword

An important function of soil binding and stabilization mixtures is to suppress flying debris and dust clouds during military training operations using unsurfaced roadways and aircraft pads. Depending on the local soil characteristics, airborne debris and particulates can be highly corrosive to exposed metals on vehicle undercarriages and nearby equipment. Thick dust clouds created by rotary-wing aircraft can also erode corrosion-resistant coatings on exposed metals and create respiratory hazards for nearby personnel. The U.S. Army Engineer Research and Development Center funded a series of laboratory studies by the University of Hawai'i at Manoa, Honolulu, in support of Department of Defense Corrosion Prevention and Control Project F10-AR06, "Natural Cementation for Unsurfaced Road at Pohakuloa Training Area, Hawaii." The study objectives were to

- characterize the material properties of all individual components of an ERDC-developed cement-free geopolymer, incorporating materials naturally occurring at the project site
- determine the compressive and flexural strength of cylinders and beams, respectively, fabricated from the blended and set geopolymer
- examine the mineralogy of the blended geopolymer concrete components using x-ray fluorescence, x-ray diffraction, scanning electron microscopy, and energy dispersive spectroscopy.

A cement-free soil-stabilization material of this type provides important potential benefits compared with similar market-available products. First, it could reduce the costs of logistics, construction, and maintenance of unsurfaced pavements in areas of operation by substituting indigenous materials found directly onsite for commercial cement or soil binders. Second, as an effective alternative to Portland cement, it could help the Army reduce its carbon footprint by as much as 1,000 kg of carbon emissions for every 1,000 kg of cement that would otherwise needed for a project.

The ERDC technical point of contact for this report is:

Sean W. Morefield, Project Manager

Construction Engineering Research Laboratory
Engineer Research and Development Center
Champaign, IL

Preface

This laboratory investigation was conducted by the University of Hawai'i at Manoa under Agreement W9132T-09-2-0022, "Laboratory Investigation of Natural Cementation Road Surfacing for Corrosion Control of Aluminum on Army Vehicles." The work was conducted for the Office of the Secretary of Defense (OSD) under the Department of Defense (DoD) Corrosion Prevention and Control (CPC) Program. The project monitor was Sean W. Morefield, CEERD-CFM.

The work was performed by the University of Hawai'i Department of Civil and Environmental Engineering and monitored by the Materials and Structures Branch of the Facilities Division (CEERD-CFM), U.S. Army Engineer Research and Development Center, Construction Engineering Research Laboratory (ERDC-CERL). At the time of publication, Vicki L. Van Blaricum was Chief, CEERD-CFM; Donald K. Hicks was Chief, CEERD-CF; and Michael K. McInerney (CEERD-CFM) was the ERDC CPC Program Coordinator. The Interim Deputy Director of ERDC-CERL was Michelle J. Hanson, and the Interim Director was Dr. Kirankumar Topudurti.

The Commander of ERDC was COL Bryan S. Green and the Director was Dr. David W. Pittman.

[This page intentionally blank.]

CHAPTER 1. INTRODUCTION

1.1 What is a Geopolymer?

Geopolymer is a term used to cover a class of synthesized inorganic polymeric materials consisting of alumino-silicates. The term geopolymer was first coined by Joseph Davidovits in 1978, although similar materials were studied in Belgium since 1940 while the former Soviet Union have been using them since the 1950s. Back then, they were known as 'soil cements'. In a geopolymer, Portland cement is not the primary cementitious agent as in concrete.

Geopolymer cements are typically alkali-activated alumino-silicate cements, and are also referred to as zeolitic or polysialate cements (Kosmatka et al., 2002). Geopolymers have a wide variety of technological uses including coatings and adhesives, new binders for fiber composites, waste encapsulation and new cement for concrete (Davidovits, 2008). In order to be considered a geopolymer cement, it must set at ambient temperature without requiring heat.

1.2 Project Background

The United States Army operates a fleet of vehicles that are constantly driven over unbound roads in the Pohakuloa Training Area (PTA) on the island of Hawaii. Moisture, soil and grit tend to accumulate on the undercarriages of their vehicles, thereby accelerating corrosion and increasing maintenance requirements. Aluminum components, such as radiator fins, are particularly susceptible to corrosion exacerbated by dust contamination from the unpaved soil. Military vehicles would greatly benefit from a corrosion prevention program to keep the vehicles in good operating condition with

minimal maintenance.

There are a vast number of Army roads in the PTA that are unpaved, but traveled heavily. The production of dust from these roads can also be a serious safety issue due to a reduction in visibility during movement of troop convoys. The military is currently using dust palliatives such as magnesium and calcium chloride to control the dust. The presence of moisture and chlorides is highly corrosive to exposed metal on the grill and undercarriage of the traversing vehicles.

1.3 Motivation for Research

It is well known that production of greenhouse gases can exacerbate global warming, which will lead to future sea level rise. It is also well known that the manufacture of Portland cement is very energy intensive and generates enormous carbon dioxide (CO_2) emissions. Portland cement results from the calcination of limestone (calcium carbonate) and silico-aluminous material as follows:

$$5CaCO_3 + 2SiO_2 \quad \Longrightarrow \quad 3CaO{\cdot}SiO_2 + 2CaO{\cdot}SiO_2 + 5CO_2$$

Traditionally, roughly one tonne (= 1 metric ton = 1000 kg) of CO_2 emission is generated for every tonne of Portland cement produced. With an increase in development in two of the most populated countries, namely China and India, CO_2 pollution has been increasing exponentially since the 1970s (Figure 1). In 2005, China alone produced 800 million tonnes of Portland cement, which is 33% of the world's cement production (Davidovits, 2008).

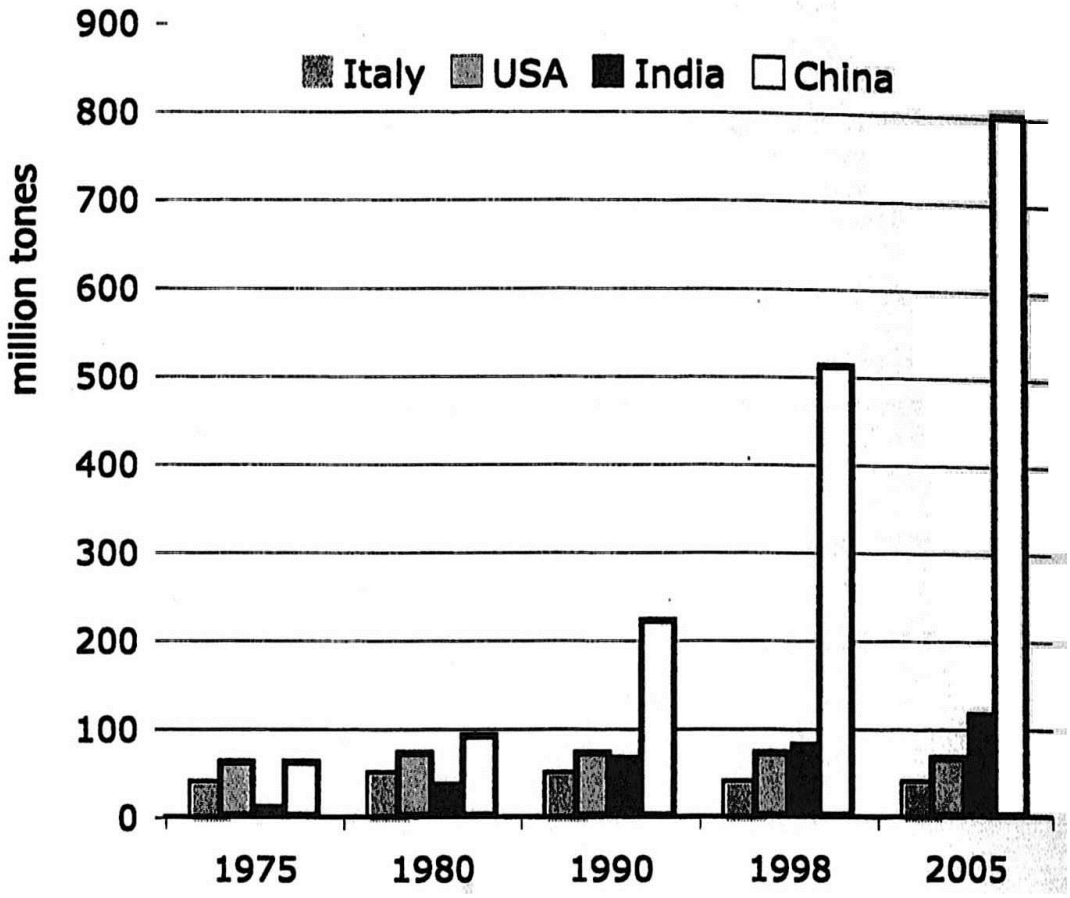

Figure 1. Cement production for China, India, Italy and USA in millions of tonnes (Davidovits, 2008)

In light of this, there has been a push to use cementless products in construction wherever feasible. This is also the impetus to mitigate the corrosion and dust/visibility problems at the PTA. Namely, treating the unpaved roads at PTA using a cementless mix and roller compacting will result in greener roads that will eliminate or at the very least reduce generation of fugitive dust.

1.4 Geopolymer Ingredients and Chemistry

The US Army Corp of Engineers has done extensive research on geopolymers and provided the following recipe for our research as summarized in Table 1.

.

Table 1. Geopolymer ingredients and their source

Ingredient	Percent by Weight (%)	Source
Basalt sand	22.59	West Hawaii Concrete , Waimea, HI - Aggregate from Waimea Quarry on the slopes of Mauna Kea which is one mountain range over from PTA
0.75-inch basalt aggregate	22.59	
1.5-inch basalt aggregate	22.59	
Hydrated Lime	4.07	Graymont Western US Inc., Salt Lake City, UT
Fly ash	4.07	Coal-fired power station operated by AES in Kapolei, HI
Slag Grade 120 [1]	4.07	Diversified Minerals, Inc., O xnard, CA
Soda ash Grade 100 [2]	8.13	FMC Wyoming Corporation, Philadelphia, PA
Water	11.89	Tap water
Total	100.00	-

Notes: 1) According to AASHTO M302 or ASTM C989, a Grade 120 slag has a high activity index; i.e.; it has a high level of reactivity.
2) According to FMC Chemicals (http://www.fmcchemicals.com/TechDataSheetsMSDS/SodaAsh.aspx, 2012), a Grade 100 soda ash has a light density with absorptive properties.

The basalt, fly ash and slag are rich in silicates and contain some aluminum. In an aqueous environment, the lime reacts with the silicates present to form a hardening compound consisting of calcium silicate hydrates and possibly some alumino-silicates. The soda ash (Na_2CO_3) serves as an alkali activator to facilitate this reaction. When the dosage is low, soda ash serves as an accelerator of hydration, but acts as a retarder when the dosage is high.

1.5 Objectives and Scope of Work

To investigate the geopolymer cementation further, the following objectives were

formulated for this research:

(1) Characterize the as-received basalt in terms of gradation, specific gravity, L.A. abrasion, minimum and maximum dry densities, sand equivalent and coarse aggregate void content;

(2) Perform unconfined compressive strength tests on specimens prepared by two ASTM standard procedures;

(3) Measure the flexural strength of geopolymer beams in four-point bending; and

(4) Examine the mineralogy of the geopolymer ingredients including the native soil and the geopolymer itself after blending using X-Ray fluorescence (XRF), X-Ray Diffraction (XRD) and Scanning Electron Microscopy (SEM) with Energy Dispersive Spectroscopy (EDS).

A key step of this study was to make the geopolymer cylinders and beams. A soda ash solution was prepared by separately mixing the seventh and eighth ingredients listed in Table 1. After mixing the first six ingredients in a concrete mixer, the soda ash solution was added to the concrete mixer. Then, twelve 6-inch-diameter cylinders of geopolymer were made in accordance with ASTM C1435 by vibrating plastic molds of the geopolymer mix on a shake table. The geopolymer cylinders were compacted in 3 lifts using a flat top weight as shown in Figure 2.

Figure 2. Compaction of the geopolymer cylinders using molds affixed to a shake table

Using a similar mix but in a separate batch, the geopolymer concrete was also poured onto a 4-ft x 4-ft x 0.5-ft deep formwork and tamped with a flat-plate vibratory compactor (Figure 3) in accordance with ASTM D1632-07 and ASTM C192-07. This work was performed on the ground floor of Holmes Hall, the Engineering building at the University of Hawaii, which has a roof cover but no walls. So the geopolymer slab was allowed to set for 2 days technically outdoors but without exposure to the sun and the rain. On the second day, eight 24-inch x 6-inch x 4.5-inch deep beams were saw cut and eight 2.25-inch-diameter cylinders were cored from the same slab. The beams and cylinders were only 4.5 inches thick as opposed to the intended 6-inches as a result of compaction and/or shrinkage of the geopolymer. These cylinders and beams were then allowed to cure outdoors with no roof cover to simulate exposure to actual Hawaiian weather prior to testing.

Figure 3. Compaction of the geopolymer slab using a flat plate vibratory compactor

The cylinders were tested in unconfined compression in accordance with ASTM D1633. The beams were tested in flexure in accordance with ASTM D1635. Some of the 6-inch-diameter cylinders were also equipped with a compressometer-extensometer to measure Poisson's ratio prior to failure. Unconfined compression and flexure tests were performed at 7, 14, 28 and 56 days ± 1 day.

1.6 Thesis Overview

Chapter 2 summarizes a brief literature review of geopolymers, fly ash and slag. In Chapter 3, the results of index testing on the basalt sand and aggregate are presented. Chapter 4 contains the results of the unconfined compressive and flexure strengths of the cylinders and beams, respectively. Results of the mineralogical analyses on the geopolymer and its constituents are discussed in Chapter 5. Chapter 6 summarizes the findings and conclusions.

CHAPTER 2. LITERATURE REVIEW

Natural pozzolans have been used for centuries. The term "pozzolan" comes from a volcanic ash mined at Pozzuoli, a village near Naples, Italy, following the 79 AD eruption of Mount Vesuvius. It is a material that when combined with lime becomes cementitious. However, the use of volcanic ash and calcined clay dates back to 2000 BC and earlier in other cultures. Many of the Roman, Greek, Indian, and Egyptian pozzolan structures can still be seen today, attesting to the durability of these materials (Kosmatka et al., 2002).

It is desirable for the construction industry to replace or reduce the use of Ordinary Portland Cement (OPC) with something that has a smaller carbon footprint to manufacture or better still with a waste product; e.g.; slag and/or fly ash. Numerous articles and papers have been written about the vast subject of geopolymers. Some of the topics addressed include how the amount of alumino-silicates, such as slag and fly ash, affect the geopolymerization differently and how geopolymer cements differ from OPC (Davidovits, 2008).

An alkali of some kind needs to be added to the geopolymer for the alkali-activation to take place. According to Shi et al. (2006), sodium carbonate (Na_2CO_3) or soda ash can be used as an accelerator of cement hydration and has also proven to be a good activator for a lot of cementing reactions involving lime with fly ash, ground granulated blast furnace slag (GGBFS), etc.

2.1 Fly ash

Fly ash is generated in large quantities as a by-product of the combustion of pulverized coal in electric power generating plants. During combustion, the coal mineral impurities (such as clay, feldspar, quartz, and shale) go in suspension and are carried away from the combustion chamber by the exhaust gases. During this process, the fused material cools and solidifies into spherical glassy particles called fly ash. The fly ash is then collected from the exhaust gases by electrostatic precipitators or bag filters (Kosmatka et al., 2002).

Fly ash is primarily silicate glass containing silicon, aluminum, iron, and calcium, but also minor amounts of magnesium, sulfur, sodium, potassium, and carbon. (Kosmatka et al., 2002). It is a potential raw material for geopolymers due to the presence of silica and alumina (Davidovits, 2008).

In accordance with ASTM 618, fly ash can be categorized as either Class C (> 10% CaO) or Class F (< 10% CaO). Class C fly ash exhibits both cementitious and pozzolanic properties whereas Class F fly ash is pozzolanic but requires the addition of lime to be cementitious (Kosmatka et al., 2002). The fly ash used in this study is from AES Hawaii, Inc., which operates a 180 MW net circulating fluidized bed coal and alternative fuel-fired generation facility. This fly ash is neither Class C nor F as it contains anywhere between 5-22% CaO according to AES Hawaii, Inc.

Fly ash can be regarded as containing three different types of constituents: crystalline minerals (quartz, mullite, spinel etc.), unburnt carbon particles, and non-crystalline alumino-silicate glass. Because of its poorly ordered atomic structure, porous nature, and overall abundance, the alumino-silicate is usually the main constituent involved in chemical reactions associated with fly ash utilization, such as in the cement and concrete

industry, or in geopolymer and zeolite production (Ward and French, 2005).

Fly ash is the most widely used supplementary cementitious material in Portland cement concrete. Fly ash was initially used in concrete, not only as a pozzolan and to enhance rheological properties, but also for the reduction of alkali-silica reaction (ASR) because of its rapid reaction with alkalis present in cement (Davidovits, 2008). ASR is a harmful chemical reaction that can develop between some siliceous mineral phases within the aggregate particles and the alkali hydroxides (K^+ or Na^+ OH^-) in the concrete pore solution (Fournier, 2010).

In ASR, the "reactive" silica within the aggregate particles progressively transforms into a secondary reaction product called "alkali-silica gel". Localized differences in free energy would then induce water and various ionic species in the pore fluid to flow into the gel. Since the gel is able to spread freely and is expansive, tensile stresses can build-up. Cracking occurs when the pressure generated at localized sites exceeds the tensile strength of the aggregate particles and the cement paste. Once extensive micro-cracking occurs, the gel spreads out freely through the cracks (Fournier, 2010).

Fournier (2010) stated that the effectiveness of fly ash in preventing ASR is a function of five key principles: (1) the composition of the ash, (2) the fineness of the ash, (3) the proportion of ash used as cement replacement, (4) the reactivity level of the aggregates and (5) the total alkali in the system. Fournier (2010) also found that the expansion in concrete that contained GGBFS decreased with increasing proportion of slag in the system.

2.2 Ground Granulated Blast Furnace Slag

Ground granulated blast furnace slag (GGBFS), also called slag cement, is a by-product of the iron production industry. GGBFS is a non-metallic hydraulic cement consisting essentially of silicates and alumino-silicates of calcium developed in a molten condition during iron production in a blast furnace. The molten slag at a temperature of about 1500°C (2730°F) is rapidly chilled by quenching in water to form a glassy sand-like granulated material (Kosmatka et al., 2002).

Puertas and Fernandez-Jimenez (2002) stated that Smith and Osborne, and Bijen and Waltje investigated cements made from a combination of 60% finely ground blast furnace slag and 40% fly ash activated by a 7% sodium hydroxide solution. Smith and Osborne found that the early strength properties were good but there was little gain in strength beyond 28 days though improved strengths can be obtained by varying the proportions of slag and fly ash or by increasing the fineness of the slag. Bijen and Waltje found that this type of geopolymer carbonated much faster than a reference made of slag cement and ordinary Portland cement. This carbonation process was accompanied by substantial reduction in compressive strength. Puertas and Fernandez-Jimenez (2002) also stated that Shi and Day studied the strength development and hydration of two types of fly ash/slag/lime mixtures activated by NaOH and sodium silicate. They concluded that the two types of mixtures produce different strength gain depending on the type of activator used. Also, the addition of a small amount of hydrated lime significantly increased the early-age strength but slightly decreased the later-age strengths.

Puertas et al. (2000) studied the strength behavior and hydration products of fly ash/slag pastes activated with NaOH. The fly ash/slag ratio is the most relevant factor

on the strength development. The main reaction product is a calcium silicate hydrate (CSH) gel, with high amount of Al in its structure (Puertas and Fernandez-Jimenez, 2002). Using X-ray diffraction (XRD), Puertas and Fernandez-Jimenez (2002) found that mineralogical characterization of the lime/slag/fly ash paste indicated crystalline reaction products of $CaCO_3$ (calcite) and hydrotalcite ($Mg_6Al_2CO_3(OH)_{16}\cdot 4H_2O$).

According to Puertas and Fernandez-Jimenez (2002), for a paste of 50%:50% fly ash/slag ratio by weight mixed with an activator solution of NaOH 10 M at a liquid to solid ratio of 0.35 and cured at 22°C, the average unconfined compression strengths at 7 and 28 days were 31.9 MPa and 63.5 MPa, respectively. The average flexure strengths at 7 and 28 days were 6.3 MPa and 13.5 MPa, respectively.

The main reaction products of the geopolymerization of fly ash and GGBFS, has been characterized by Kumar et al. (2009) using XRD and SEM with EDS as alumino-silicate-hydrate (ASH) and calcium-silicate-hydrate (CSH) gels. During geopolymerization, alumino-silicates dissolve in alkali solution to form free SiO_4 and AlO_4 tetrahedral units.

CHAPTER 3: INDEX TESTS ON BASALT AGGREGATE

3.1 Grain Size Distribution

The geopolymer aggregate consists of equal weight proportions of the following: basalt sand, ¾-inch basalt aggregate, and 1½-inch basalt aggregate. The overall gradation of the aggregate was determined by sieving each of the three gradations separately. Prior to sieving, the basalt sand, ¾-inch basalt aggregate, and 1½-inch basalt aggregate were each separately oven dried at 110°C. Then, a representative sample of each material was dry-sieved in accordance with ASTM D 6913. The gradations of all three materials and the estimated overall gradation curve are shown in Figure 4. The overall gradation was determined by using one third of the percent passing for each sieve size of aggregate in the geopolymer mix. This overall gradation curve formed the basis of reconstituting samples for some of the index tests.

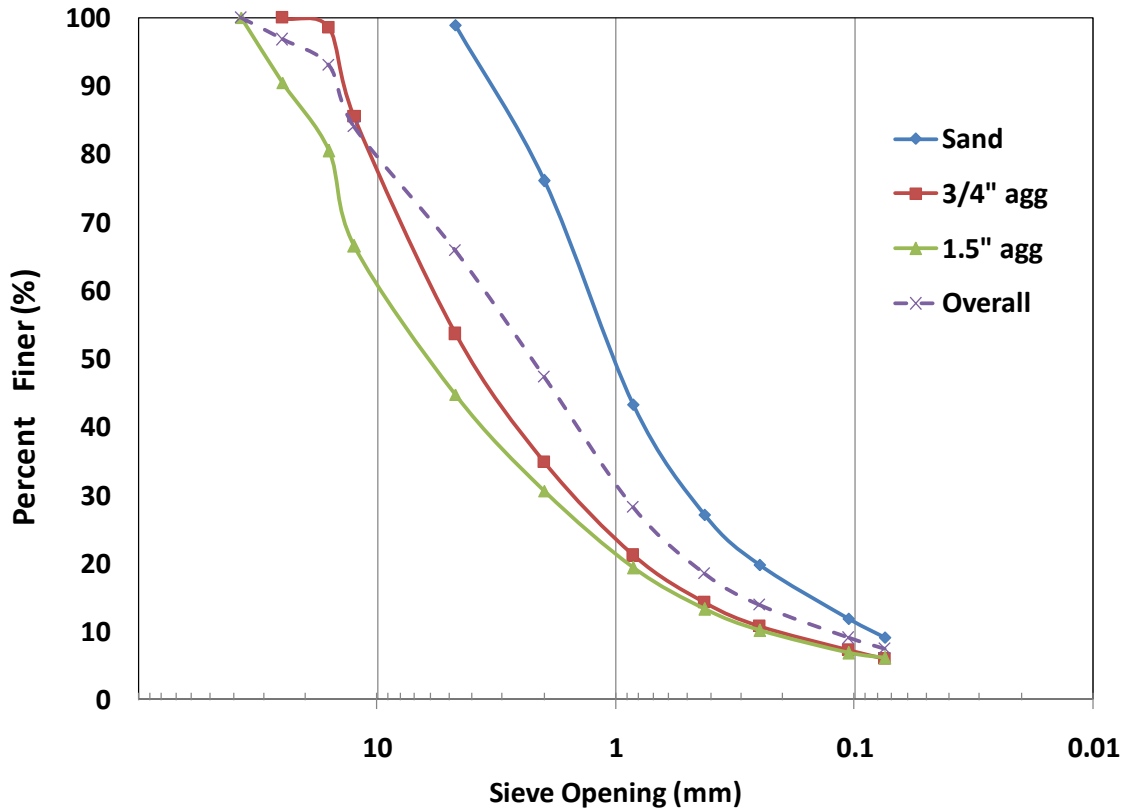

Figure 4. Grain size curves for the three aggregate sizes and the overall gradation curve for the geopolymer aggregate.

3.2 Specific Gravity and Absorption

Specific gravity and absorption were measured in accordance with AASHTO T84 and AASHTO T85 for fine (passing a No. 4 sieve) and coarse (retained on a No. 4 sieve) aggregates, respectively. The fine and coarse aggregates were prepared by first sieving the three aggregates into their respective individual sizes and then blending them. The test results are summarized in Table 2. From this table, it can be seen that the fine aggregate has lower specific gravities and higher absorptions than the coarse aggregate.

The results also meet the State of Hawaii Department of Transportation or HDOT (2005) specifications requirement for coarse aggregate used in concrete mixes, which requires a maximum absorption of 6%. HDOT has no absorption requirements for fine aggregate.

Table 2. Specific gravity and absorption

	Bulk Specific Gravity	Bulk Specific Gravity (SSD)	Apparent Specific Gravity	Absorption (%)
Coarse Aggregate Passing 3/4”	2.55	2.62	2.75	2.76
Coarse Aggregate Passing 1.5”	2.40	2.50	2.65	3.97
Fine Aggregate Sand	2.29	2.39	2.55	4.42
Fine Aggregate Passing 3/4”	2.15	2.32	2.59	7.82
Fine Aggregate Passing 1.5”	2.19	2.36	2.63	7.68

3.3 L.A. Abrasion

L.A. abrasion tests were conducted in accordance with AASHTO T96 to provide a measure of the aggregate’s durability to impact loading. L.A. abrasion was measured for two different gradings: A and B. The ¾-inch and 1½-inch aggregates were combined to prepare both gradings A and B in accordance with their proportions in the overall gradation curve. The test results are shown in Table 3. This meets the State of Hawaii Department of Transportation (2005) specifications requirement that for aggregate used in concrete mixes, the maximum allowable L.A. abrasion is 40%.

Table 3. L.A. abrasion test results for basalt

Material	Grading	Weight after test (g)	Weight before test (g)	Percent of weight loss (%)
¾” and 1 ½” basalt	A	3480	4992	30.3
¾” and 1 ½” basalt	B	3653	4991	26.8

3.4 Minimum and Maximum Dry Densities

Minimum and maximum dry density tests were conducted on the overall gradation in accordance with ASTM D 4254 and ASTM D 4253, respectively. Method A was used for the minimum dry density test. The minimum dry density test is used to determine the loosest condition a cohesionless, free-draining soil can attain. The test was performed three times to account for any error that many have occurred and to see if the results are repeatable. The minimum dry density (ρ_{dmin}) and minimum dry unit weight (γ_{dmin}) values are summarized in Table 4.

Table 4. Minimum dry density test results

Minimum Dry Density	ρ_{dmin} (g/cm³)	γ_{dmin} (kN/m³)
Trial 1	1.90	18.7
Trial 2	1.76	17.3
Trial 3	1.71	16.8

Method 1A was used for the maximum dry density test. The maximum dry density test is used to determine the densest condition a cohesionless, free-draining soil can attain. The maximum dry density (ρ_{dmax}) and maximum dry unit weight (γ_{dmax}) results are summarized in Table 5.

Table 5. Maximum dry density test results

Maximum Dry Density	ρ_{dmax} (g/cm³)	γ_{dmax} (kN/m³)
Trial 1	2.07	20.3
Trial 2	1.99	19.5

3.5 Sand Equivalent

Sand equivalent (SE) tests were performed in accordance with ASTM D 2419. The SE is used to determine the characteristics of the finer grained portion of cohesionless soils. These characteristics are found by performing a sedimentation test. The fraction of sand that passes the No. 4 sieve is placed into a cylinder with a water and flocculent mix, shaken and allowed to rest for twenty minutes. The sand settles onto the bottom of the cylinder at a height, h, the clay material is suspended above the sand with a distinct height, H, above which is clear water. The sand equivalent is then calculated as SE = H/h. If SE > 30%, the material is not plastic. If SE < 20%, the fines are clayey. Typically, clays have sand equivalents between 0% and 5%, silty clays between 6% and 10%, clayey silts between 11% and 30%, clayey fine sands between 30% and 40%, and silty fine sands above 40%. The higher the SE, the higher the percentage of sand and silt size particles. The SE value for the basalt sand and aggregate was measured to be 72%. This meets the State of Hawaii Department of Transportation (2005) specifications minimum SE requirement for fine aggregate used in concrete mixes of 70%.

3.6 Coarse Aggregate Void Content

Coarse aggregate void content tests were conducted in accordance with AASHTO TP56-99. The void content provides an indication of the aggregates' angularity, sphericity and surface texture. Aggregate that is more rounded, spherical or smooth surfaced generally has a lower void content. The ¾-inch and 1 ½-inch aggregate was combined to represent the overall gradation curve of the coarse aggregate in the

geopolymer mixture and was tested twice to provide an average. The measured coarse aggregate void contents are shown in Table 6.

Table 6. Void content of geopolymer aggregate

	Trial 1	Trial 2	Average
Uncompacted Void Content %	48.3	46.6	47.5

CHAPTER 4. STRENGTH AND FLEXURE TESTS

Unconfined compression tests to measure the strength and Poisson's ratio and 4-point flexure tests to measure the modulus of rupture of the geopolymer at different days after casting were performed. Details of the specimen preparation, tests and results are presented in this chapter.

4.1 Strength Tests

Tests were performed on both 2.25-inch- and 6-inch-diameter cylinders to determine the compressive strength at different curing times. The small cylinders were cored from a 4.5-inch-thick slab of geopolymer that was tamped using a flat plate vibratory compactor (Figure 3). The 6-inch-diameter cylinders were compacted in individual cylindrical molds using a shake table and a weight to consolidate the geopolymer in accordance with ASTM D1632-07 and ASTM C192-07 (Figure 2). The cylinders were intentionally left outside the University of Hawaii at Manoa Structures lab to cure to simulate exposure to typical Hawaiian weather and humidity for up to 8 weeks. The 6-inch-diameter cylinders remained inside the molds with only the top exposed to the elements until the test date whereas the 2.25-inch-diameter specimens were cored 2 days after the pour and the entire specimen was exposed to the elements. Prior to testing, the specimen density was determined since the compressive strength is a function of both age and density, which is a reflection of the degree of compaction. Age is an important factor as well since the strength increases with time due to continued hydration of the geopolymer.

Prior to testing, all cylinders were capped with a molten sulfur compound to create smooth and flat ends (Figure 5). The capping compound used was Basolit Sulfur Cement No. 600 manufactured by Sauereisen. The strength of the capping compound far exceeds those of the geopolymer and thus, the capping compound should not have any influence on the measured geopolymer cylinder strengths.

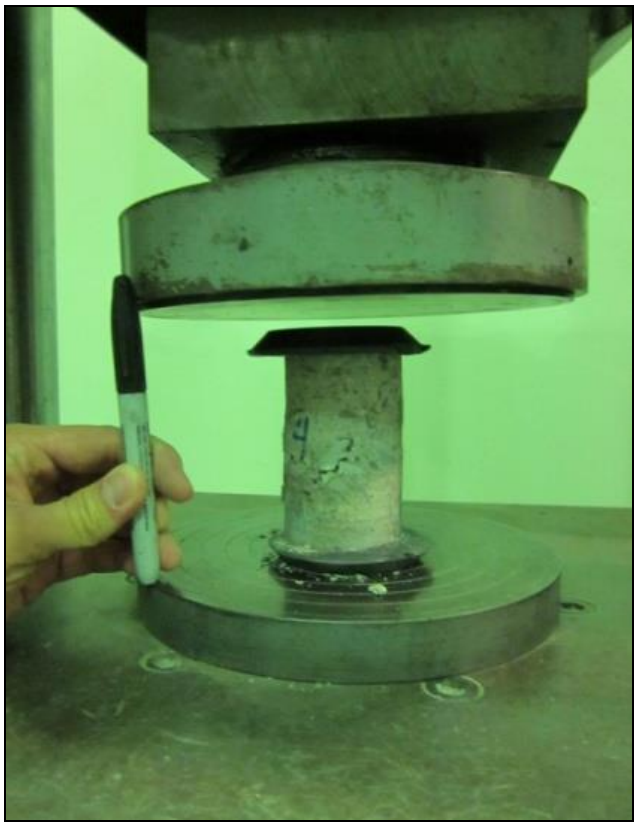

Figure 5. Sulfur compound caps at the ends of a 2.25-inch-diameter geopolymer. Picture taken after testing.

Compression tests of the 2.25-inch- and 6-inch-diameter cylinders were conducted using a Riehle Hydraulic 318BJ loading frame in accordance with ASTM D 1633. All specimens had a height to diameter ratio of at least 2.

4.1.1 2.25-inch-diameter Cylinder Test Results

Results of the compression tests are summarized in Table 7 and Figure 6. Because the 2.25-inch diameter cylinders had irregular ends, their densities were determined by: (1) weighing each cylinder prior to capping; (2) measuring the volume of the geopolymer by filling a graduated cylinder with 400 cc of water, placing the geopolymer inside and noting the increase in volume = volume of cylinder; and (3) calculating the density as the mass divided by the volume. Then, the specimens were capped. A total of 2 specimens were tested on each test date.

Table 7. Compressive strength and density at different ages of curing for the 2.25-inch-diameter specimens

Specimen No.	Age (Days)	Density (lb/ft^3)	Density (g/cm^3)	Strength fc' (psi)
1	8	137.2	2.198	1193
2	8	135.8	2.176	1491
3	14	138.5	2.220	2025
4	14	136.9	2.194	1444
5	29	134.5	2.156	2136
6	29	132.1	2.117	1889
7	56	140.1	2.245	2269
8	56	139.0	2.228	1636

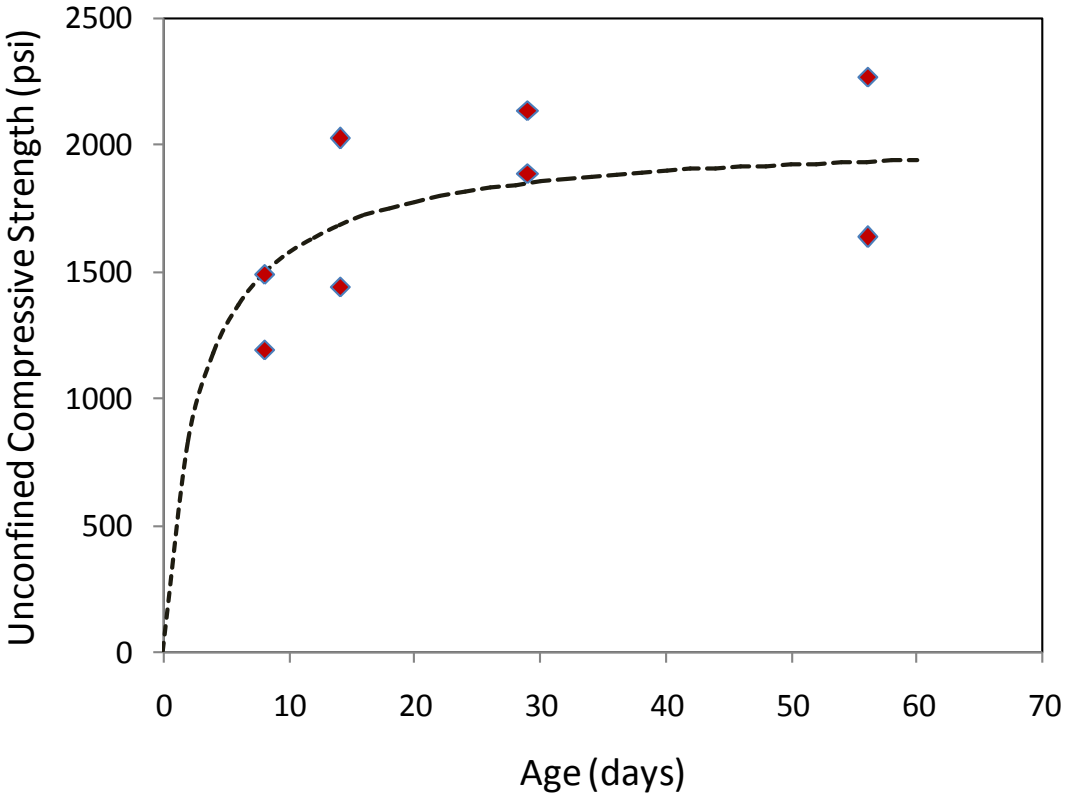

Figure 6. Unconfined compressive strengths of the 2.25-inch-diameter geopolymer as a function of age

29-day compressive strengths of the geopolymer ranged from 1889 to 2136 psi with an average of 2013 psi. This strength range represents 47% to 53% (average = 50%) of regular construction grade concrete having a 28-day design compressive strength of 4000 psi. The tests were not performed at exactly 7, 14, 28 and 56 days for both the small and large cylinders as ideally would be the case because of holidays and weekends.

To reduce scatter, the unconfined compressive strength divided by the density of the geopolymer cylinder was plotted versus time as seen in Figure 7. There was a slight decrease in the scatter with the modified y-axis.

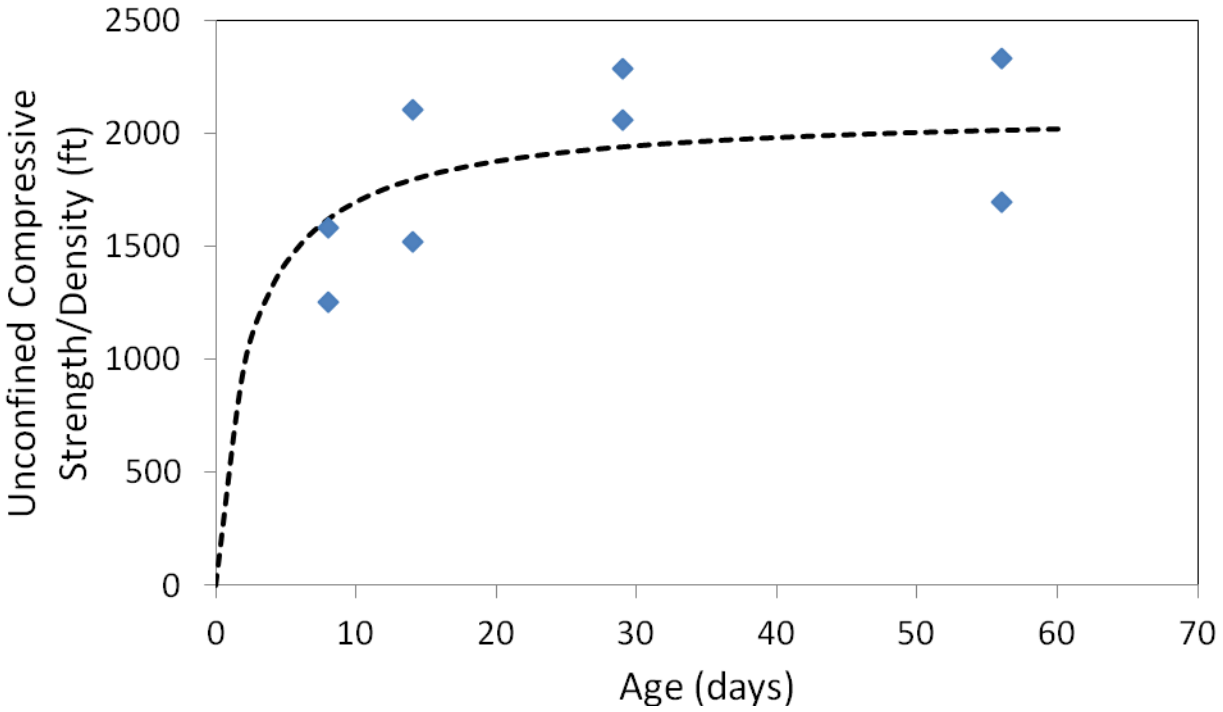

Figure 7. Unconfined compressive strength divided by density of the 2.25-inch-diameter geopolymer as a function of time

4.1.2 6-inch-diameter Cylinder Test Results

Prior to measuring the compressive strength of the 6-inch-diameter geopolymer cylinders, the density of the specimens was measured. Since these cylinders have right ends, the procedure is as follows: (1) weigh the specimen after extracting from the mold; (2) measure the diameter and height to calculate the volume; and (3) divide the mass by the volume. The specimens were then capped as shown in Figure 8 prior to unconfined compression testing. Capping was necessary in this case to ensure completely smooth and level ends. A total of three specimens were tested on each test date. The results of the compression tests are summarized in Table 8.

.

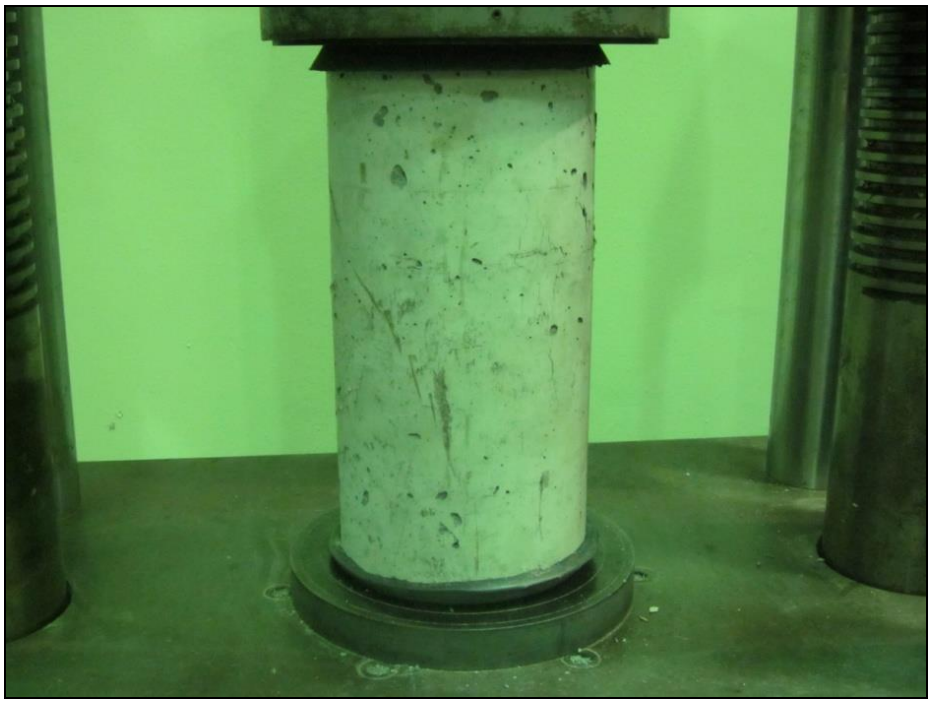

Figure 8. Sulfur compound caps at the ends of a 6-inch-diameter geopolymer. Picture taken prior to testing.

Table 8. Compressive strength and density at different ages of curing for the 6-inch-diameter specimens

Specimen No.	Age (Days)	Density (lb/ft^3)	Density (g/cm^3)	Strength fc' (psi)
1	7	139.8	2.243	1683
2	7	134.3	2.156	1631
3	7	136.6	2.193	1497
4	15	142.4	2.286	2184
5	15	132.3	2.123	1302
6	15	126.4	2.029	1229
7	28	139.3	2.236	2618
8	28	128.8	2.068	1154
9	28	136.4	2.189	2007
10	57	139.4	2.237	2720
11	57	124.9	2.005	1229
12	57	133.7	2.147	1778

28-day compressive strengths of the geopolymer ranged from 1154 to 2618 psi with an average of 1926 psi. This strength range represents 29% to 65% (average = 48%) of regular construction grade concrete having a 28-day design compressive strength of 4000 psi.

Concrete is known for its strength increase with time due to continued cement hydration. Overall, the geopolymer also exhibits this trend as seen in Figure 9 although there is scatter at each test date.

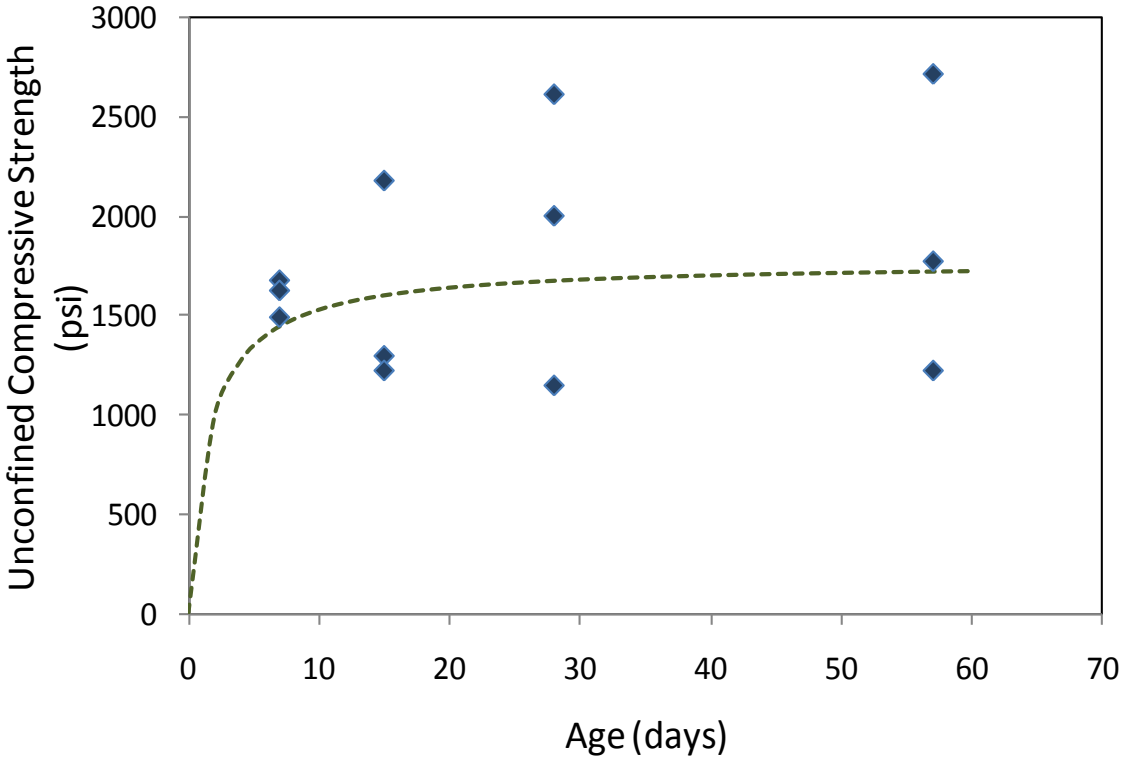

Figure 9. Unconfined compressive strengths of the 6-inch-diameter geopolymer as a function of age

To reduce scatter, the unconfined compressive strength divided by the density of the geopolymer cylinder was plotted versus age as seen in Figure 10. There was a slight decrease in the scatter as a result.

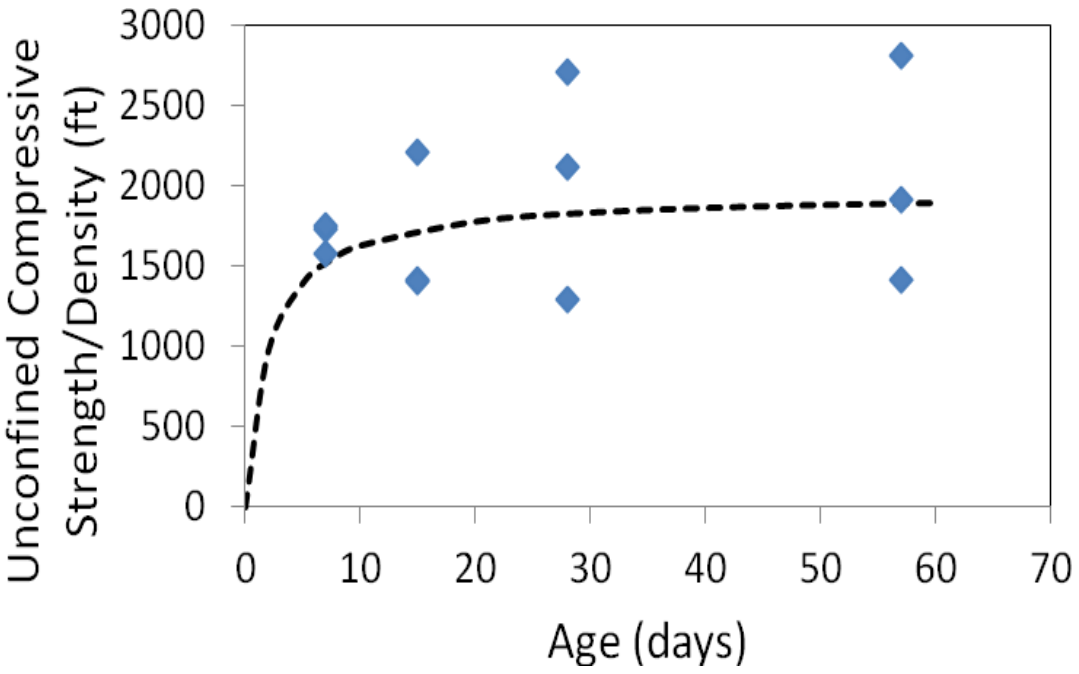

Figure 10. Unconfined compressive strength divided by density of the 6-inch-diameter geopolymer as a function of age

4.1.3 Combined Test Results

Figure 11 shows the combined unconfined compressive strengths of the 2.25-inch- and 6-inch-diameter cylinders with respect to time. The unconfined compressive strength divided by the density of the geopolymer cylinder was plotted versus age as seen in Figure 12 to reduce the scatter. This improvement was deemed not accurate enough for use to predict this geopolymer strength.

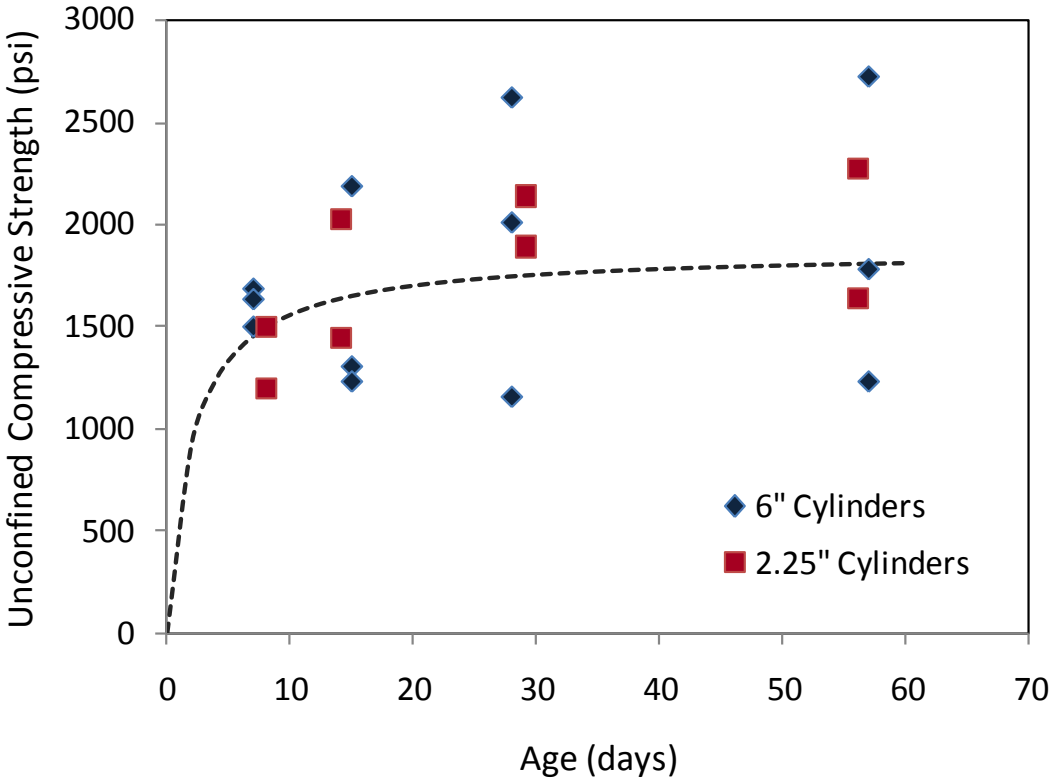

Figure 11. Unconfined compressive strengths of both the 2.25-inch- and 6-inch-diameter geopolymer as a function of age

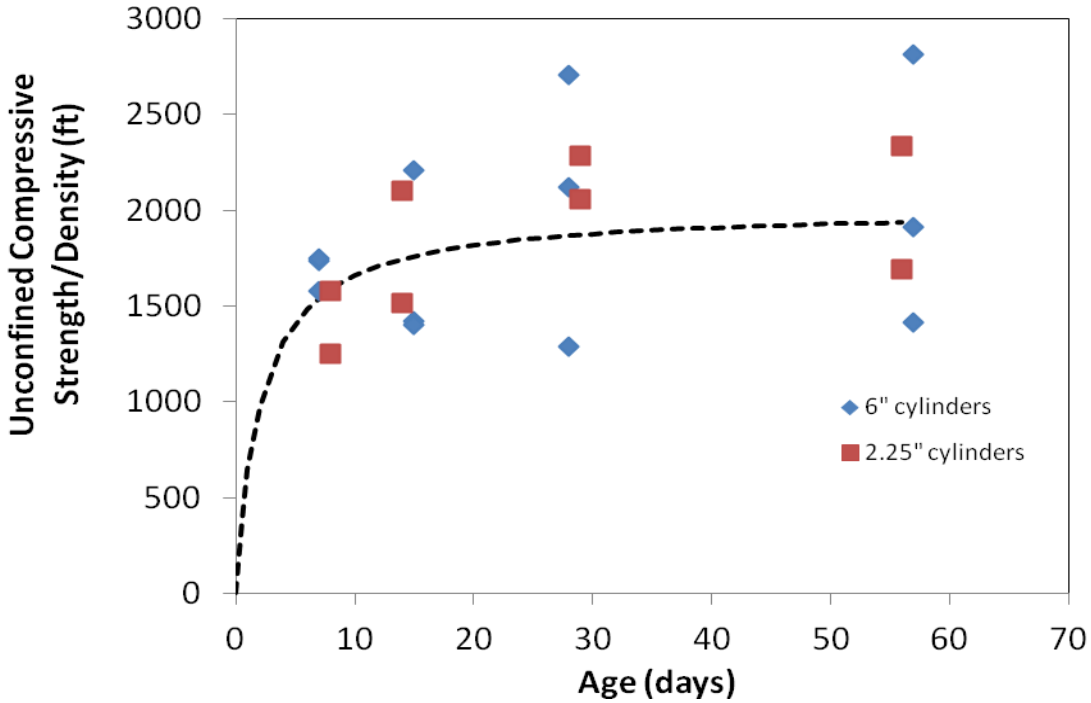

Figure 12. Unconfined compressive strength divided by density of both the 2.25-inch- and 6-inch-diameter geopolymer as a function of age

An improved but yet simple hyperbolic model can be derived to fit the test data as follows:

$$f_c^{'} = \frac{t}{a + (b\frac{\gamma}{\gamma_w} + c)t} \qquad (4.1)$$

where f_c' (psi) = compressive strength at age t (days), γ = unit weight of the geopolymer, γ_w = unit weight of water and a, b and c are constants. Using ordinary least squares regression, the constants were found to be a = 0.0015, b = -0.00141 and c = 0.00356. The predicted versus measured f_c' is shown in Figure 13 together with a line of equality and the goodness of fit equation,

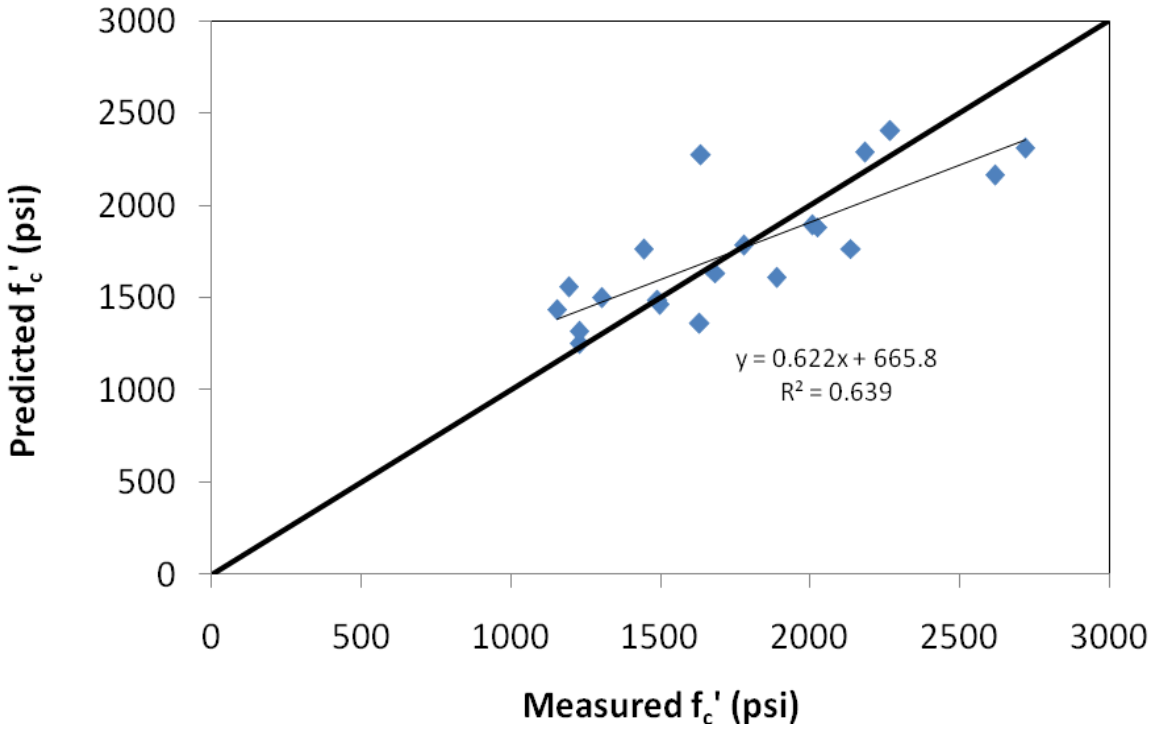

Figure 13. Predicted versus measured compressive strengths of both the 2.25-inch- and 6-inch diameter geopolymer using the hyperbolic function in Equation 4.1

It can be seen that overall, the model yields a reasonable fit to the data.

4.1.4 Poisson's Ratio

When a cylinder is loaded in compression, it shortens and at the same time develops a lateral strain or bulge. The ratio between the lateral and axial strains is called Poisson's ratio, μ. (Kosmatka et al., 2002).

$$\mu = - \frac{\varepsilon_D}{\varepsilon_L} \qquad (4.2)$$

where μ = Poisson's ratio, $\varepsilon_D = \Delta D/D$ = strain perpendicular to the load direction and $\varepsilon_L = \Delta L/L$ = strain along the load direction. Figure 14 illustrates the deformations that occur during axial loading.

A compressometer-extensometer shown in Figure 15 was used to measure the Poisson's ratio in the 6-inch-diameter geopolymer specimens only and not the smaller ones since the device is usually used for testing Poisson's ratio of concrete cylinders of the same size. It can measure both vertical and radial displacements. The vertical displacement is measured over the middle 9 inches of the cylinder.

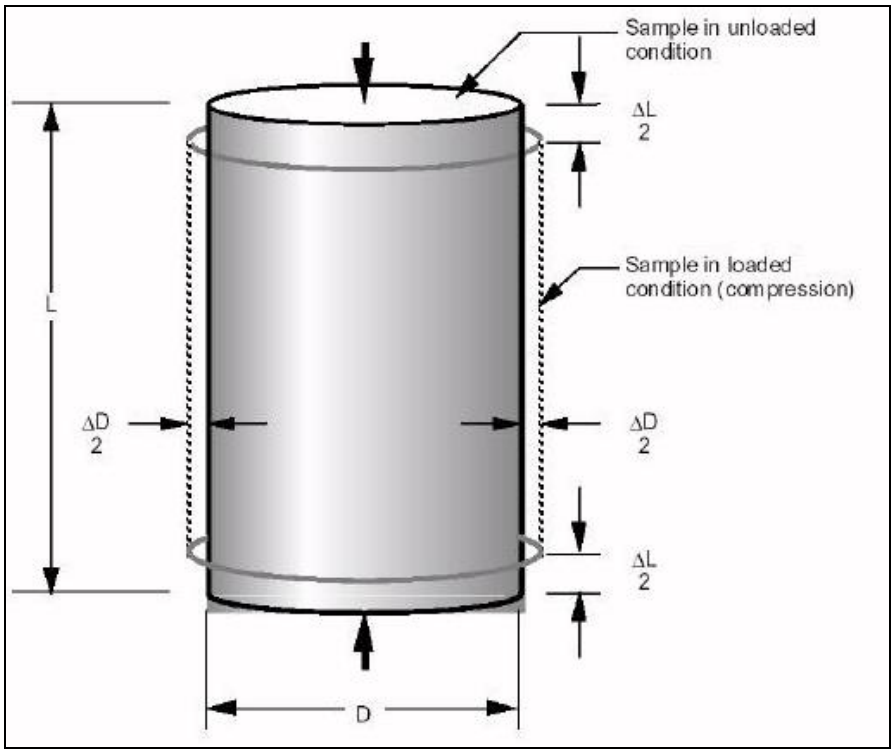

Figure 14. Dimensions needed to calculate Poisson's ratio

Figure 15. Compressometer-extensometer used to measure the Poisson's ratio in the 6-inch-diameter geopolymer specimens

Poisson's ratio was measured at 7, 15, 28 and 57 days. On each test date, the procedure is as follows:

1. Measure the diameter of each specimen.
2. Load one of the three specimens to failure.
3. Measure the vertical and lateral deformations in the other two specimens during two load-unload-reload cycles between 10 % and 40 % of the failure load from Step 2.
4. Calculate Poisson's ratio using Equation 4.2.

Poisson's ratio is usually around 0.20 for concrete, but will vary from 0.15 to 0.25

depending on moisture content, aggregate, compressive strength and age (Kosmatka et al., 2002). Poisson's ratio for the geopolymer ranged from 0.12 to 0.27. At the time of batching (time t = 0), the geopolymer is a liquid. Since water is incompressible, it was assumed that the geopolymer at t = 0 is incompressible and has a Poisson's ratio of 0.5. The Poisson's ratio then decreased with increasing age as illustrated in Figure 16.

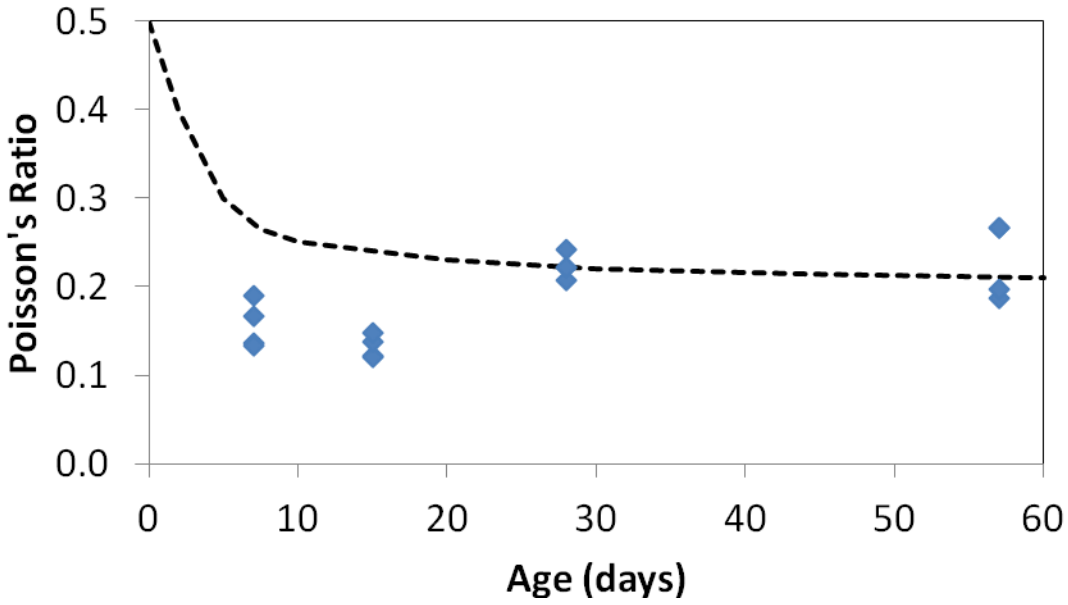

Figure 16. Poisson's ratio for 6-inch-diameter cylinders as a function of age

4.2 Flexure Tests

Eight 6-inch-wide, 24-inch-long and 4.5-inch-deep beams were saw-cut from a compacted geopolymer slab as shown in Figure 17. These beams were numbered 1 through 8 and were used to determine the modulus of rupture at different days after curing. At a given test date, beams from different locations of the slab were tested rather than adjacent beams to avoid any biases due to localized compaction in the test results.

Figure 17. Saw-cut beams used for flexure strength test numbered 1 through 8

The modulus of rupture provides a measure of the flexural strength of the geopolymer. It can be measured using a four point bending setup where the loading span is one third of the support span (Figure 18). In this case, the modulus of rupture in bending is the maximum fiber stress at failure and is found using the following formula:

$$R = PL/bd^2 \qquad (4.3)$$

where, R = modulus of rupture, kPa (psi), P = maximum applied load, N (lbf), L = span length, mm (in.), b = average width of specimen, mm (in.), and d = average depth of specimen, mm (in.).

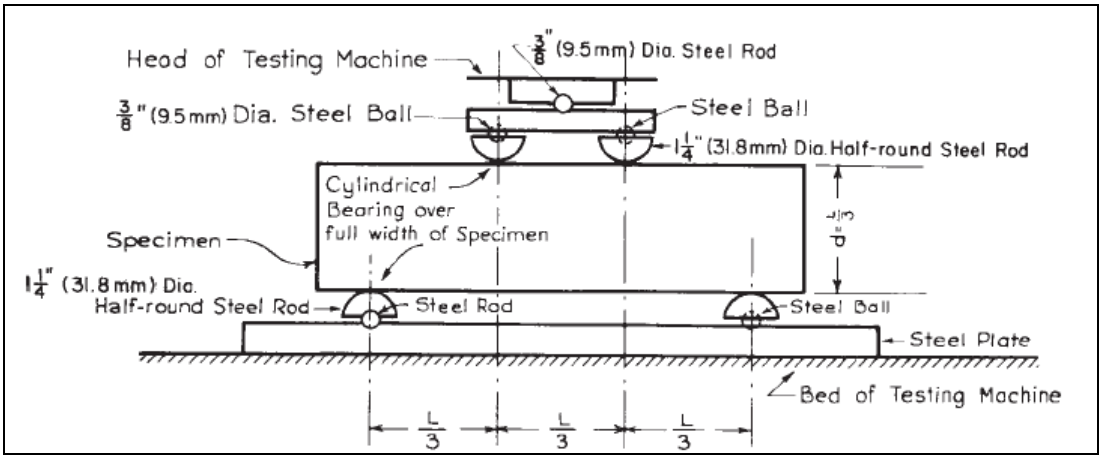

Figure 18. Four point bending setup to measure the modulus of rupture (ASTM D 1635, 2006)

The same loading frame for the unconfined compressive strength tests was used for the modulus of rupture test which is shown in Figure 19.

(a) (b)

Figure 19. Loading frame and modulus of rupture test (a) before and (b) after failure

The age, number and corresponding moduli of rupture of the eight beams are shown in Table 9.

Table 9. Modulus of rupture as a function of age

Specimen No.	Age (Days)	Modulus of Rupture (psi)
1	8	277
7	8	388
2	14	331
8	14	434
3	29	290
5	29	292
4	56	465
6	56	372

As illustrated in Figure 20, the majority of the flexural strength is acquired in the first week of curing. However, the geopolymer does continue to gain flexural strength with time. A simple hyperbolic model can be derived to fit the test data as follows:

$$R = \frac{t}{a + bt} \tag{4.4}$$

where R = modulus of rupture at age t (days), and a and b are constants. Using ordinary least squares regression, the constants were found to be a = 0.005566 and b = 0.002318.

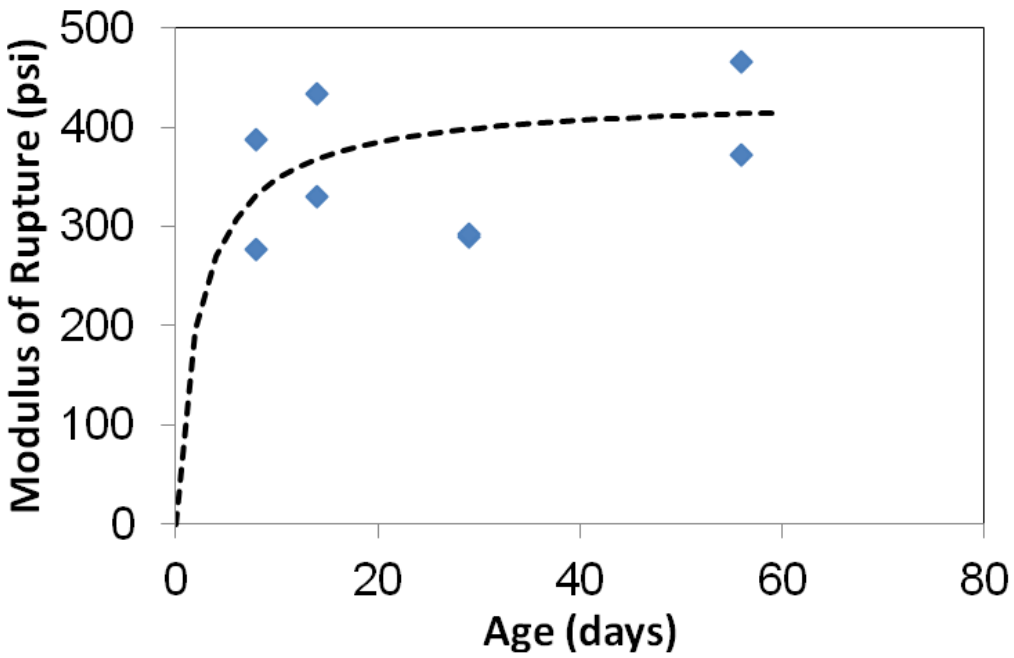

Figure 20. Variation of modulus of rupture with age

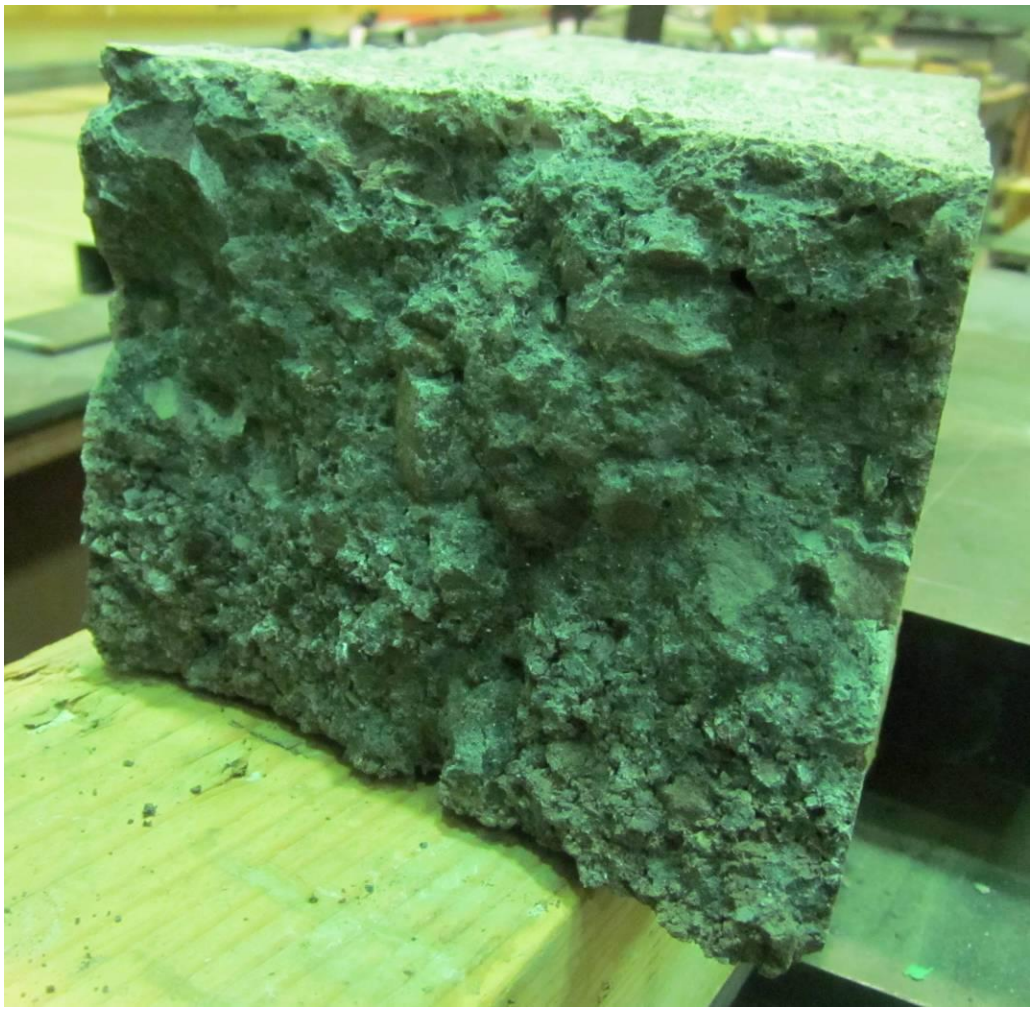

Figure 21. Broken section of a beam after flexure test. Failure occurs mostly between the aggregate and cementitious paste with no shearing through the aggregate observed.

Figure 21 shows a typical failure section of the beam specimen after the four-point bending test. It can be observed that failure occurred in the bond between the cementitious matrix and the coarse aggregate rather than through the aggregate themselves, the latter occurring when weak aggregate is used. Since the majority of the basalt aggregate was separated from the matrix rather than sheared, it can be speculated that the aggregate is of high quality and the bond between the aggregate and cementitious matrix is not particularly strong.

CHAPTER 5. MINERALOGICAL ANALYSES

5.1 Introduction

Mineralogical analyses were performed on the individual geopolymer ingredients as well as on the geopolymer itself. Analysis of the individual ingredients provides an understanding of their chemical makeup. A secondary purpose of the mineralogical analyses of the geopolymer constituents was to determine if they were "glassy" or amorphous; a "glassy" or amorphous constituent would indicate more highly reactive properties. Analysis of the geopolymer itself could provide an understanding of the resulting chemical reaction product after blending.

Mineralogical analyses performed consist of the following:

1. X-Ray fluorescence (XRF) was performed to determine the elements present and their quantities in the slag and fly ash only
2. Scanning Electron Microscopy (SEM) with Energy Dispersive Spectroscopy (EDS) was performed to identify the elements present in the individual constituents and the geopolymer and
3. X-Ray Diffraction (XRD) was performed to determine the crystalline compounds present in the individual constituents and the geopolymer.

A test matrix is provided in Table 10. SEM with EDS was performed on two constituents (slag and fly ash) and the geopolymer. SEM with EDS was not performed on all constituents separately since the (1) chemistry of lime and soda ash are known (from the manufacturer) and (2) basalt aggregate can be studied whilst performing SEM with EDS on the geopolymer. XRD analyses were performed on almost all the

ingredients. This facilitates superposition of the XRD results for the individual constituents and for the geopolymer to gauge whether the original ingredients are still present in the geopolymer.

Table 10. XRF, SEM with EDS and XRD test matrix

	Lime	Slag	Fly Ash	Soda Ash	Basalt Sand	3/4-inch Basalt Aggregate	1.5-inch Basalt Aggregate	Geopolymer
XRF	X	✔	✔	X	X	X	X	X
SEM with EDS	X	✔	✔	X	X	X	X	✔
XRD	✔	✔	✔	✔	✔	X	✔	✔

5.2 X-Ray Fluorescence

X-ray Fluorescence (XRF) analysis was performed using a Siemens SRS-303 Automated X-ray Fluorescence Spectrometer having a Rh X-ray source at 60 kV and 45 mA. XRT was performed on the slag and fly ash, both of which came in a finely pulverized form.

The basic principle of the XRF is to bombard the sample with X-rays. If the energy is sufficient to dislodge a tightly-held inner electron in an atom, an outer electron will replace the missing inner electron. As this happens, energy is released. This energy is emitted in the form of a radiation that has a lower energy than the primary incident X-rays, and is termed fluorescent radiation (Writh and Barth, 2012). The sample fluoresces with X-ray peaks at characteristic energies depending on its elemental composition. Major elements are analyzed by the methods outlined by Norrish and Chappell (1977).

5.3 Scanning Electron Microscopy with Energy Dispersive Spectroscopy

5.3.1 Equipment and Principles of the Test

SEM was performed using a JEOL JXA-8500F Hyperprobe Electron Probe Micro Analyzer or EPMA (Figure 22) on sample mounds of the slag and fly ash and polished thin sections of the geopolymer. Magnified images of the samples were captured by bombarding them with high energy electrons. The electron beam diameter is smaller than 1 micron (focused spot approximately 30 nm) with an acceleration potential of 15 keV and a spectrum current of 15 nA (nanoamperes). The electrons interact with the nuclei of the elements generating secondary electrons (SE), backscatter electrons (BSE) and X-rays. The BSE are used to provide an enlarged image of the sample; e.g., a large deflection with little energy transfer is characteristic of a nucleus having a large mass and vice versa.

Energy Dispersive Spectroscopy (EDS) spectra were obtained using a Thermo-Noran System-6 setup, with a 10 mm2 Silicon Drift Detector (SDD) having a 128 eV resolution. A finely focused electron beam allows a very small section of the sample to be analyzed.

Figure 22. Electron Probe Microanalyzer used in the SEM with EDS analyses

There are two kinds of analyses possible with the SEM with EDS: qualitative and quantitative. The wavelength and intensity of lines in the X-ray spectrum allow the elements present in the sample to be identified using EDS. Identifying the elements present in a qualitative analysis entails recording the spectrum by means of an X-ray spectrometer. It should be pointed out that EDS is not capable of detecting elements lighter than lithium including hydrogen. Also, carbon will always be detected even though it may not be in the sample because of the sample preparation process (see Section 5.3.2).

A common type of SEM image is the "dot map" or "element map". This map is produced by adjusting the brightness of the cathode-ray tube (CRT) with pulses from a spectrometer set to detect the characteristic X-rays of a particular element. Each dot in the image corresponds to one X-ray photon. In a quantitative analysis, the density of the dots is nearly proportional to the elemental concentration in that area (Reed, 1993). Multiple areas of interest can be selected from each sample to be analyzed. Depending on the elemental composition, the image is either darker or lighter. To emphasize the contrast between the primary elements present in the geopolymer, the SEM images were imported into PhotoShop and color coded as discussed later in Section 5.5.

5.3.2 Sample Preparation

Sprinkles of slag and fly ash were poured onto sample holders for SEM with EDS analyses. Also, multiple slices of geopolymer concrete were sawed off of the geopolymer beams used in the flexure tests to create thin sections, examples of which are shown in Figure 23 and Figure 24. A water concrete saw was used to make an initial ¼-inch-thick slice. This slice was then used to make a thin section. The polished petrographic, rectangular thin sections were 25 x 40 mm, with a thickness of 30 μm.

Before the samples were placed in the EPMA, the sample mounds in the case of fly ash and slag or thin sections in the case of the geopolymer were coated with a thin layer of carbon. The carbon coating removes electrical charges to provide a path for the probe current. Even though this process is necessary, it has the effect of reducing the observed X-ray intensity, partly by absorbing some of the energy of the incident electrons and also partly by decreasing the emerging X-rays. These effects may cause significant errors in a quantitative analysis (Reed, 1993). However, since carbon has a low atomic number (6), its effect on the X-ray intensities is somewhat limited (Reed, 1993) and that is why it is commonly used as a coating for SEM samples.

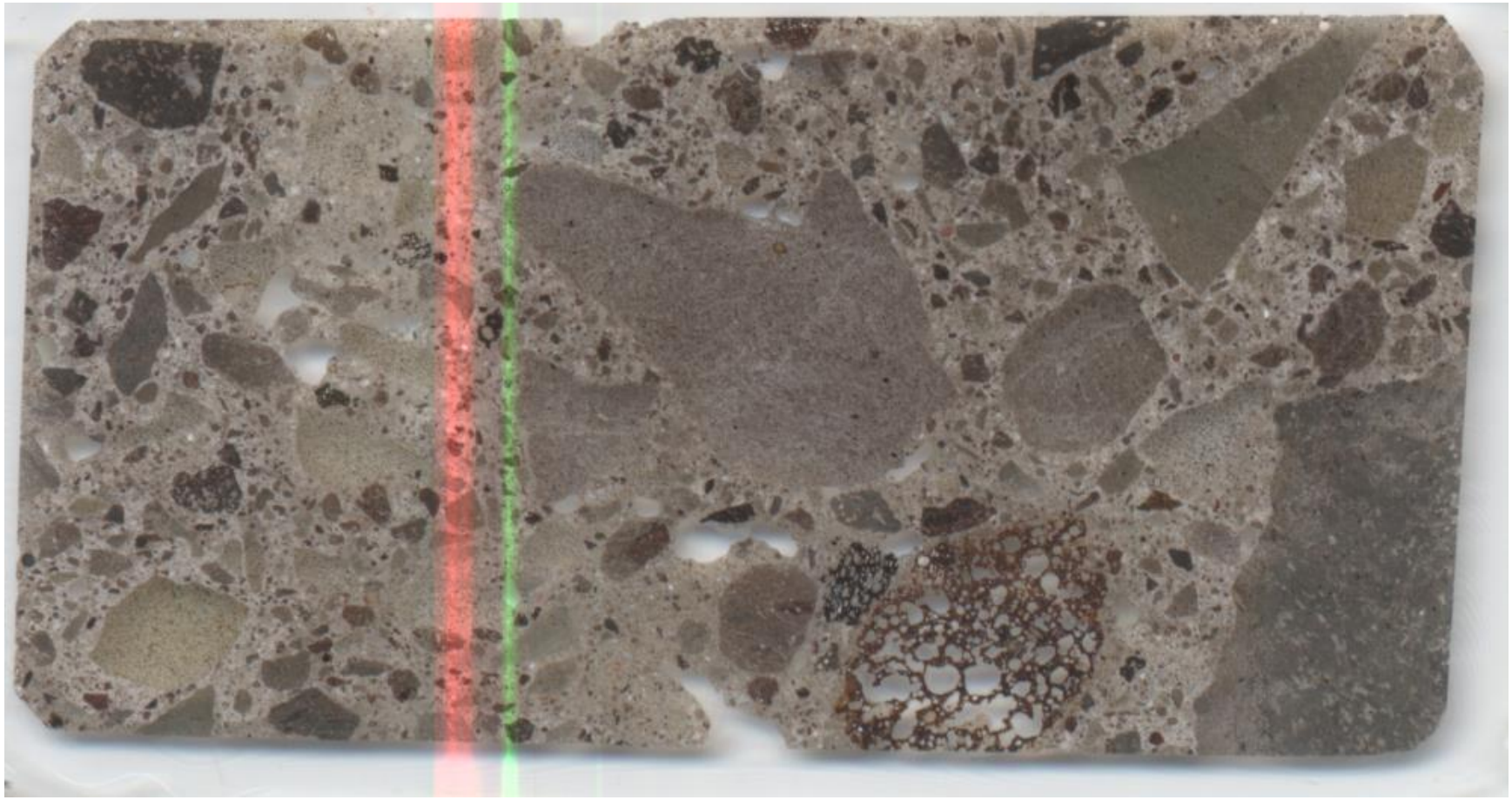

Figure 23. Polished geopolymer thin section number 79

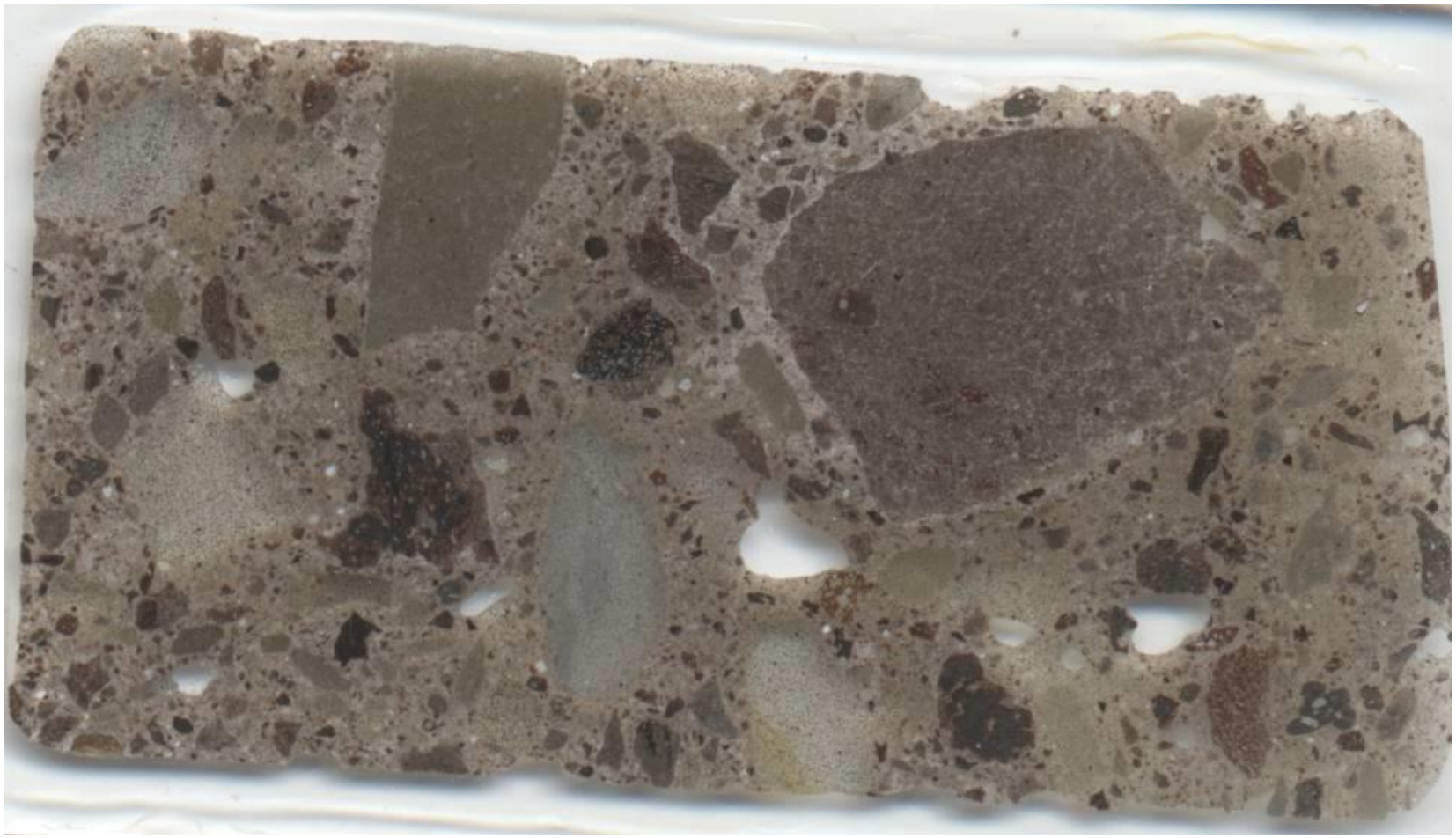

Figure 24. Polished geopolymer thin section number 80

5.4 X-Ray Diffraction

5.4.1 Equipment and Principles of the Test

XRD was performed on pulverized samples using a Bruker-Nonius Kappa CCD X-ray Diffractometer (Figure 25) housed at the University of Hawaii, Hilo. A single sample was mounted in a holder, which was then placed in a goniometer. Using a 40 kV, 40 nA power supply to heat up a copper filament, X-rays generated were fed through a beryllium window filter before impacting the sample at an angle. A detector, chilled with an Oxford Cryostream/700 Liquid Nitrogen Cryostat, received the X-rays after reflection from the sample.

The Bruker X-ray diffractometer comes equipped with EVA, a software that can be used for mining powder diffraction databases to identify compounds present in the sample. The University of Hawaii at Hilo equipment also has another software, JADE, that has a similar capability.

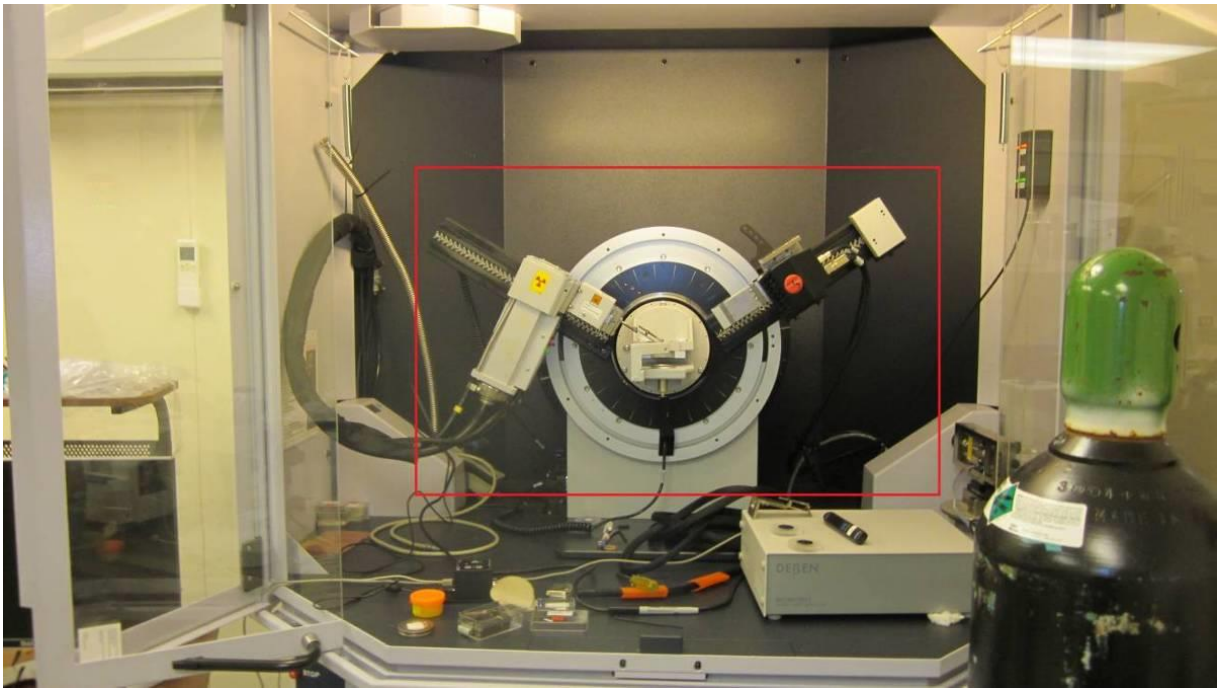

Figure 25. Bruker-Nonius Kappa CCD X-ray Diffractometer; red box highlights the goniometer.

Solid matter can be described as either amorphous or crystalline. In an amorphous state, the atoms are arranged in a random manner similar to the disorder in liquids. Glass is an example of an amorphous material. In crystalline matter, the atoms are arranged in a regular pattern, and there is a smallest volume element that by repetition in three dimensions describes the crystal (Scintag, 1999).

When an X-ray beam hits an atom, the electrons around the atom start to oscillate with the same frequency as the incoming beam. If the material is amorphous, there will be destructive interference; i.e., the combining waves are out of phase and there is no resultant energy leaving the sample. When x-rays impact a crystal however, there will be constructive interference in a few directions. Since the atoms in a crystal are arranged in a regular pattern, the waves will be in phase in these few directions where there will be well defined X-ray beams leaving the sample. This is because at a certain

angle of incidence (θ), X-rays of a given wavelength (λ) scattered by atoms in parallel planes are in phase and "reflection" occurs as shown in Figure 26. These constructive interferences at particular values of angle of incidence, θ, are detected as peak intensities on the XRD pattern (Scintag, 1999).

The results of an XRD analysis consist of a series of peak intensities for various values of 2θ. Using Bragg's law, the θ value corresponding to each peak can be related to the inter-atomic spacing, d, of the crystals forming the sample as follows:

$$n\lambda = 2d \sin\theta \qquad (5.1)$$

where n is the number of wavelengths corresponding to the path difference between rays scattered from successive layers (Reed, 1993).

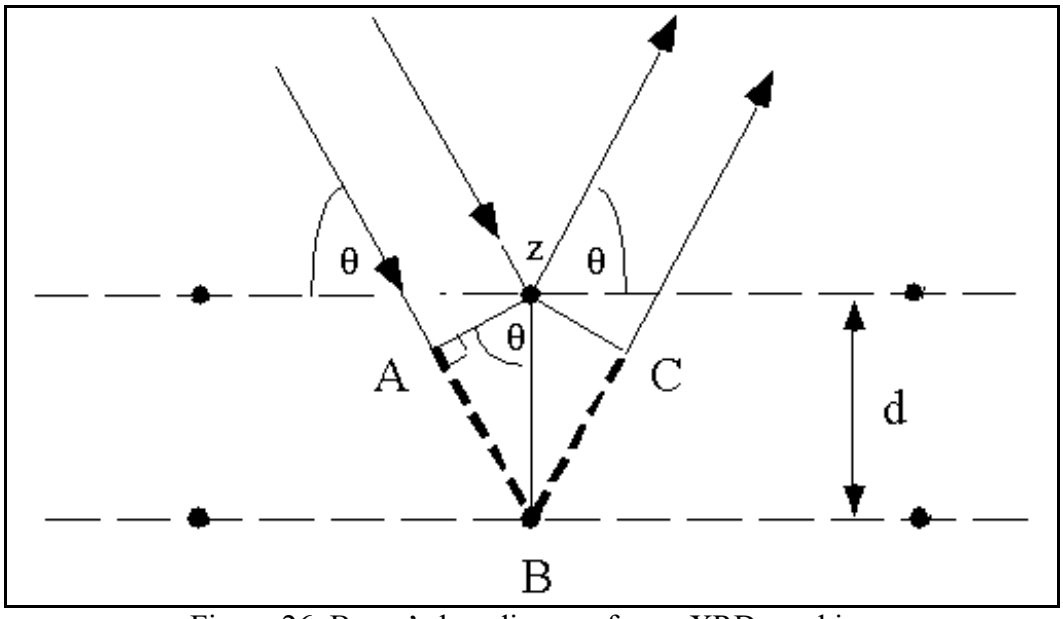

Figure 26. Bragg's law diagram for an XRD machine

5.4.2 XRD Sample Preparation

XRD specimens such as basalt sand, basalt aggregate, and geopolymer were all too large and needed to be pulverized. Soda ash, slag, and fly ash were adequately fine and did not need pulverization. Pulverization was performed using a ceramic mortar and pestle. The powdered samples were then pressed into sample holders (Figure 27) and smoothed out with the edge of a glass plate.

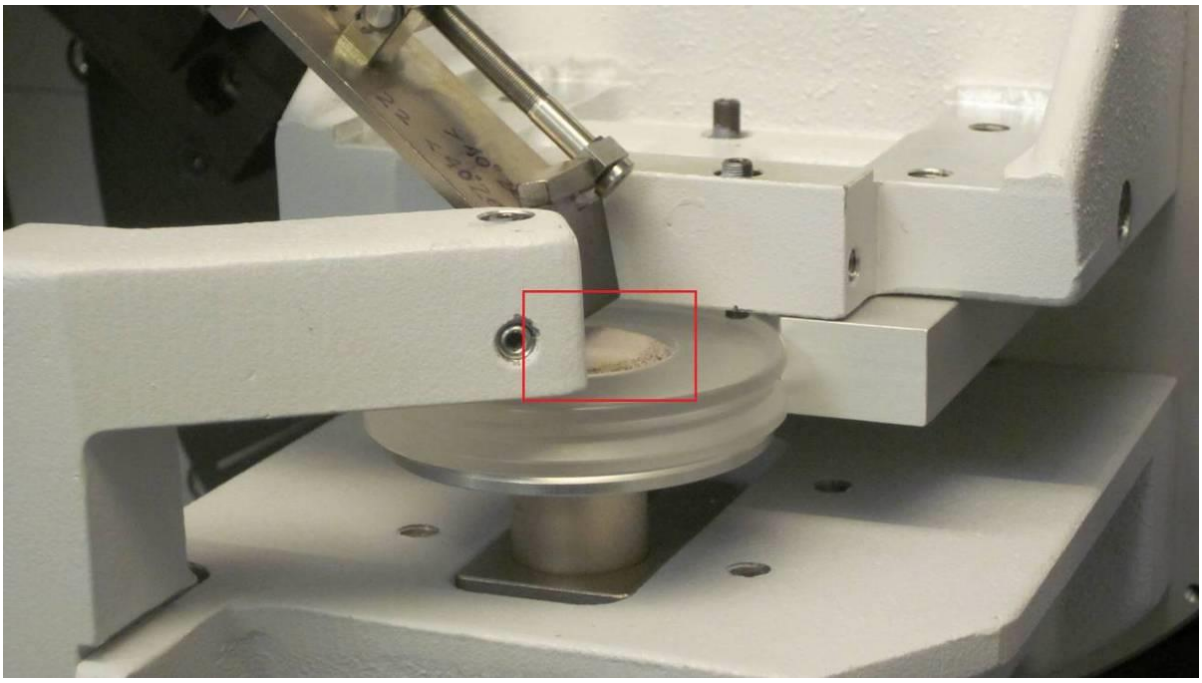

Figure 27. XRD sample placement in the goniometer, the red box encompasses the sample

5.5 Mineralogical Results for the Geopolymer Constituents

Results for the mineralogical analyses of the constituents of the geopolymer using XRF, SEM with EDS, and XRD are presented in this section.

5.5.1 Slag

Chemical composition of the slag as provided by Diversified Minerals Inc. is shown in Table 11. It can be seen that the amorphous silica constitutes a fairly large percent of the slag along with calcium compounds.

Table 11. Slag chemical composition (provided by Diversified Minerals)

Constituent	**Weight (%)**
Amorphous Silica, Hydrated	30-45
Calcium Compounds	30-45
Magnesium Compounds	8-15
Aluminum Compounds	5-15
Sulfur	0-4
Iron Compounds	0-1
Titanium Compounds	0-1
Manganese Compounds	0-1
Potassium Compounds	0-1
Crystalline Silica	0-0.2

5.5.1.1 XRF

Results of XRF analysis on the slag are summarized in Table 12. Comparing Table 11 and Table 12, the XRF results are consistent with the supplier's values except for MgO. Measured values of MgO is slightly lower.

5.5.1.2 SEM with EDS

Figure 28a and Figure 29a show magnified images of two slag particles that were then subjected to elemental composition analyses, the results of which are shown in Figure 28b and Figure 29b. Multiple, 13 in total, single-point shots of the slag revealed two

different types of elemental composition from the EDS analyses. One set contained both high sulfur and calcium peaks with traces of silicon and aluminum as seen in Figure 28b. The other had high levels of aluminum and silicon with traces of calcium and potassium as seen in Figure 29b. Both sets of EDS results contained oxygen in significant quantities.

Table 12. XRF analysis results of slag

SAMPLE	SiO_2	TiO_2	Al_2O_3	Fe_2O_3	MnO	MgO	CaO	Na_2O	K_2O	P_2O_5	SUM	LOI (loss on ignition)
MC-SLAG-A	32.65	0.6	14.72	0.41	0.26	5.88	43.16	0	0.33	0	98.01	0
MC-SLAG-B	32.74	0.6	14.76	0.42	0.27	5.88	43.18	0	0.33	0	98.18	0
MC-SLAG-C	32.54	0.59	14.67	0.41	0.27	5.82	42.99	0	0.33	0	97.62	0

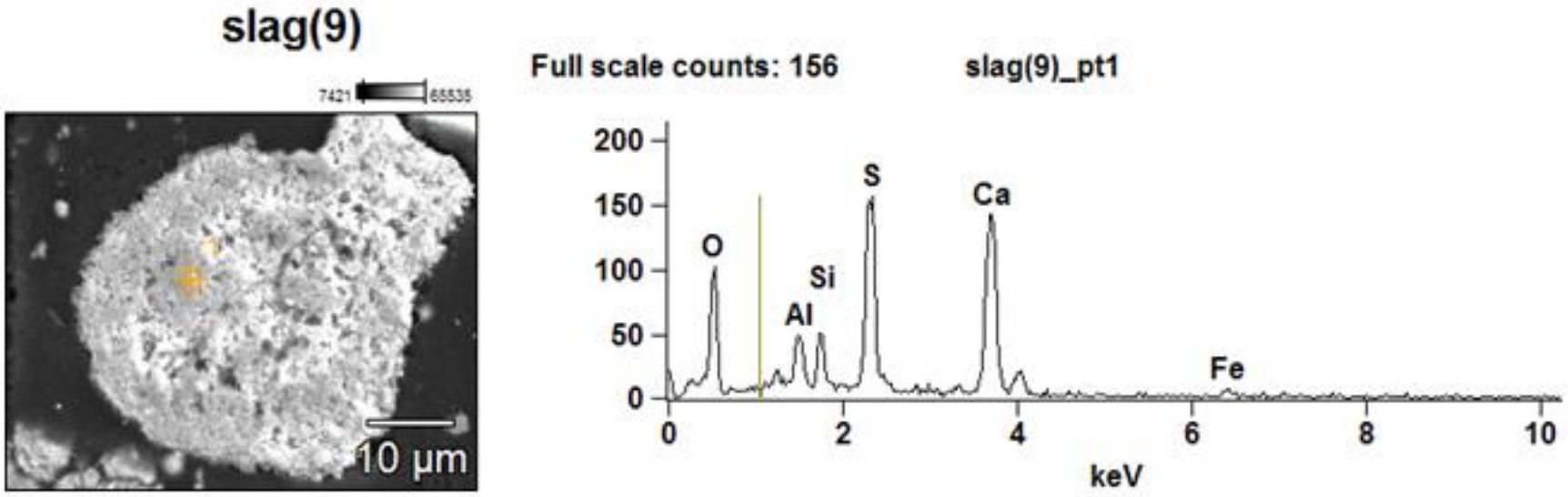

(a) (b)

Figure 28. (a) Backscatter electron image of slag (b) Sulfur and calcium dominate elemental composition of slag

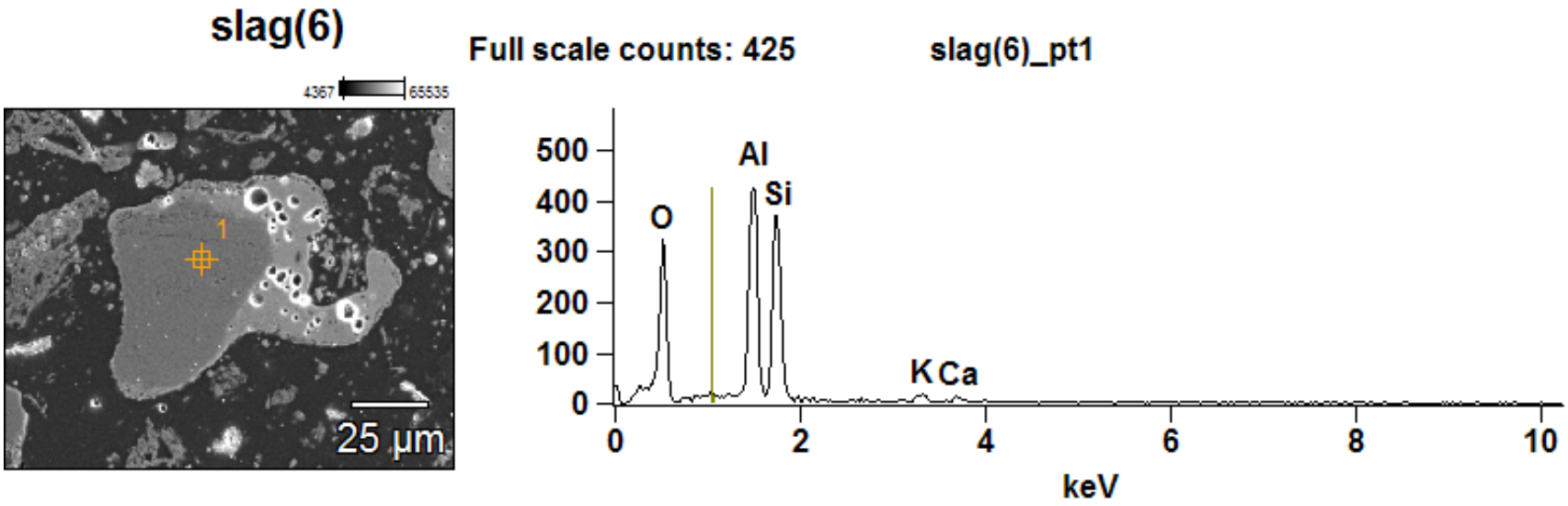

(a) (b)

Figure 29. (a) Backscatter electron image of slag (b) Aluminum and silicon dominate elemental composition of slag

5.5.1.2 XRD Results

The raw XRD result for slag is shown in Figure 30. It can be seen that the slag is definitely glassy as characterized by the low gentle hump when 2θ is approximately 31˚. The XRD signature also contains one dominating peak and a few lesser peaks within and outside the amorphous hump. Prior to compound identification, the background signatures were removed from the raw XRD results. The smoothing process resulted in the loss of the amorphous hump when compared to the raw XRD image as shown in Figure 31. Based on this figure and the XRD mineralogical identification software, it was determined that the most distinct slag peak is that of calcium sulfate and the smaller peaks suggest the presence of calcium sulfate hydrate compounds. However, the calcium sulfate peak does not account for many of the elements in the slag. The amorphous hump suggests that amorphous compounds that are present cannot be identified by XRD, which can only detect crystalline materials. The SEM with EDS results also indicate the presence of aluminum with silicon and oxygen possibly suggesting the presence of a form of calcium alumino-silicate. Since slag is known to be rich in silicates, this result is not unreasonable. The calcium alumino-silicate cannot be detected by the XRD most likely because it is amorphous.

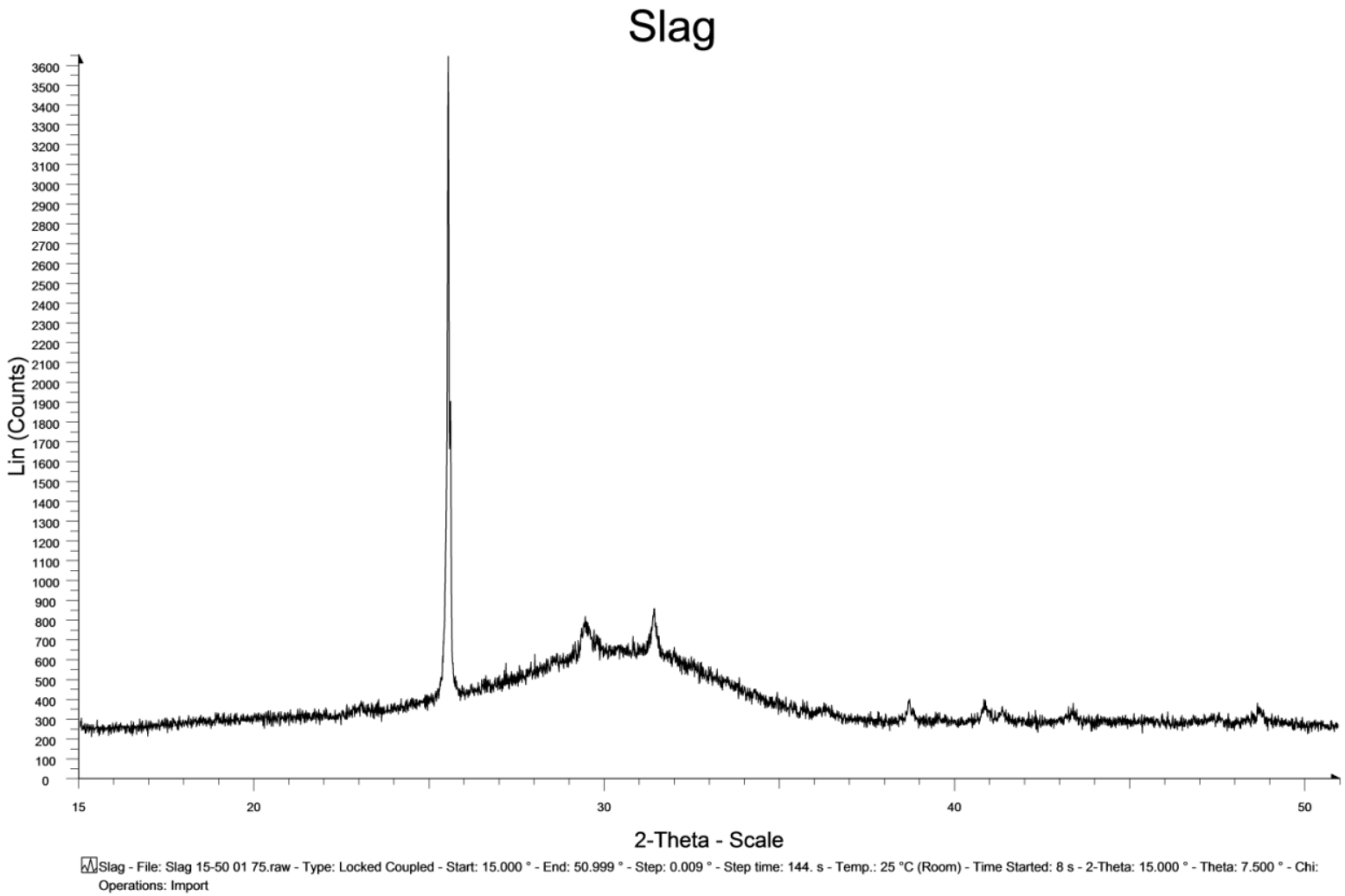

Figure 30. Raw XRD image of slag with the amorphous hump

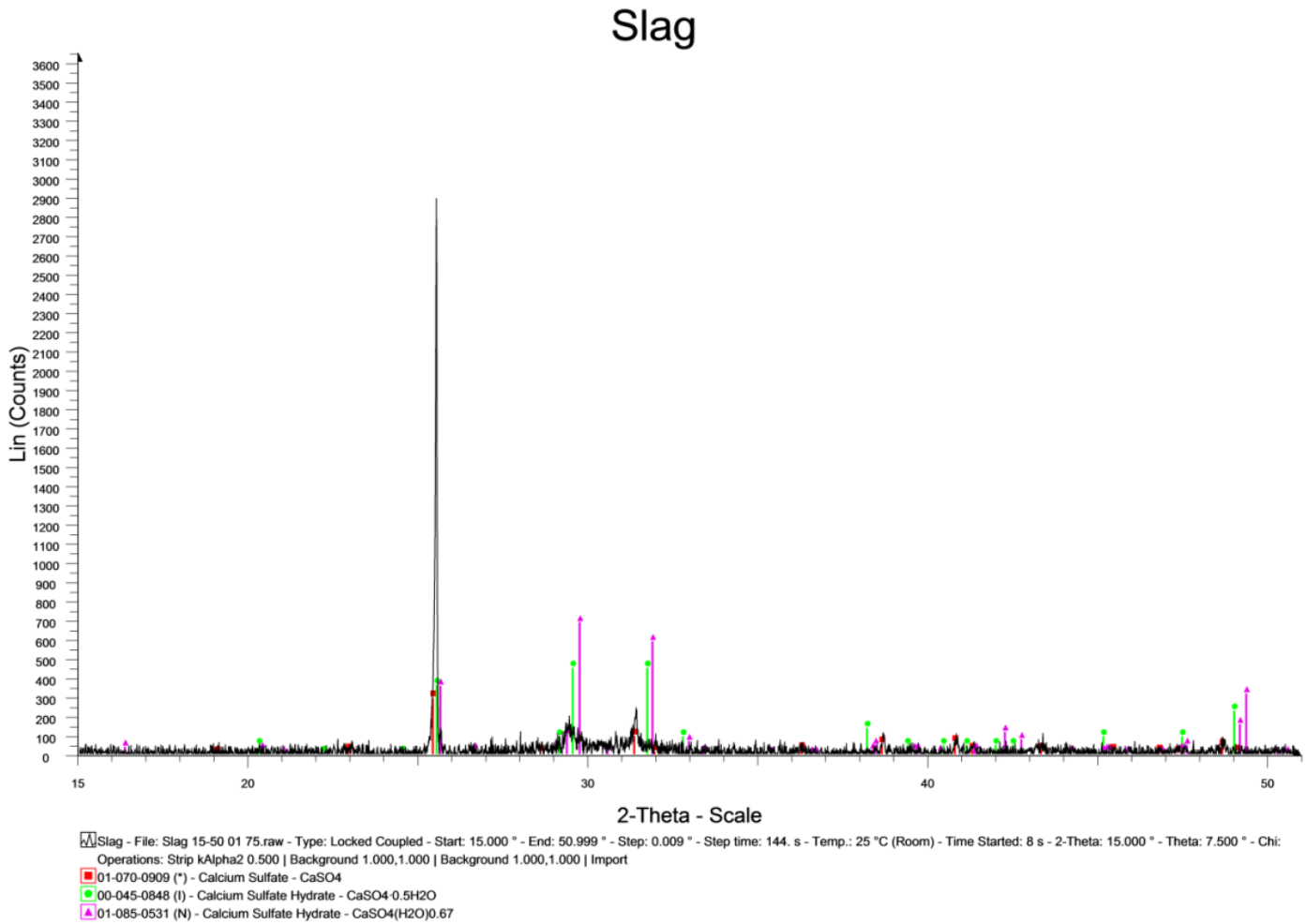

Figure 31. Smoothed XRD image of slag with calcium sulfate, calcium sulfate hydrate, and calcium sulfate hydrate mineralogical identifications

5.5.2 Fly Ash

The chemical composition of AES Corporation's fly ash from their coal plant on the island of Oahu is summarized in Table 13.

Table 13. Fly ash chemical composition (provided by AES Corporation)

Constituent	**Weight (%)**
Alumina (Al_2O_3)	11-15
Calcium Oxide (CaO)	5-22
Iron Oxide (Fe_2O_3)	2-5
Silica (SiO_2)	59-63
Magnesium Oxide (MgO)	Trace
Potassium Oxide (K_2O)	Trace
Calcium Sulfate ($CaSO_4$)	Trace

5.5.2.1 XRF Results

Results of XRF analysis on the fly ash are summarized in Table 14. Comparing Table 13 and Table 14, the XRF results are consistent with AES' values except for SiO_2 (measured is much lower), Al_2O_3 (measured is slightly higher) and Fe_2O_3 (measured is slightly higher).

5.5.2.2 SEM with EDS Results

Multiple points of the fly ash in the SEM image were studied using EDS and overall, there were generally two different classes of elemental compositions observed as shown in Figure 32 and Figure 33b. Figure 32b shows a high calcium content with traces of magnesium. Points 1 and 2 in the image have this similar elemental composition. Figure 33b shows the composition for Point 3 in the SEM image. This composition is very different with high levels of silicon, aluminum, calcium and magnesium with a trace of manganese. Points 3, 4, and 5 all have similar compositions. Overall, the SEM with EDS results indicate that the fly ash is very heterogeneous.

Table 14. XRF analysis results of fly ash

SAMPLE	SiO_2	TiO_2	Al_2O_3	Fe_2O_3	MnO	MgO	CaO	Na_2O	K_2O	P_2O_5	SUM	LOI (loss on ignition)
FLY-A	39.76	0.88	18.76	6.76	0.03	1.19	22	0	1.02	0.5	90.9	3.527%
FLY-B	39.58	0.88	18.68	6.57	0.03	1.18	22.46	0	0.99	0.5	90.87	3.527%

5.5.2.3 XRD Results

Figure 34 depicts the raw XRD results of fly ash. It can be seen that the fly ash is also amorphous with a gentle middle hump. The smoothed XRD image of fly ash shown in Figure 35 confirms that the major peak is that of silicon dioxide (quartz), which corroborates the second set of SEM and EDS results. Another significant mineralogical compound identified in the fly ash XRD is calcium oxide, which is consistent with the first set of SEM with EDS results and also consistent with the fact that the fly ash is known to have 5-22% CaO based on Table 13 and about 22% based on the XRF results.

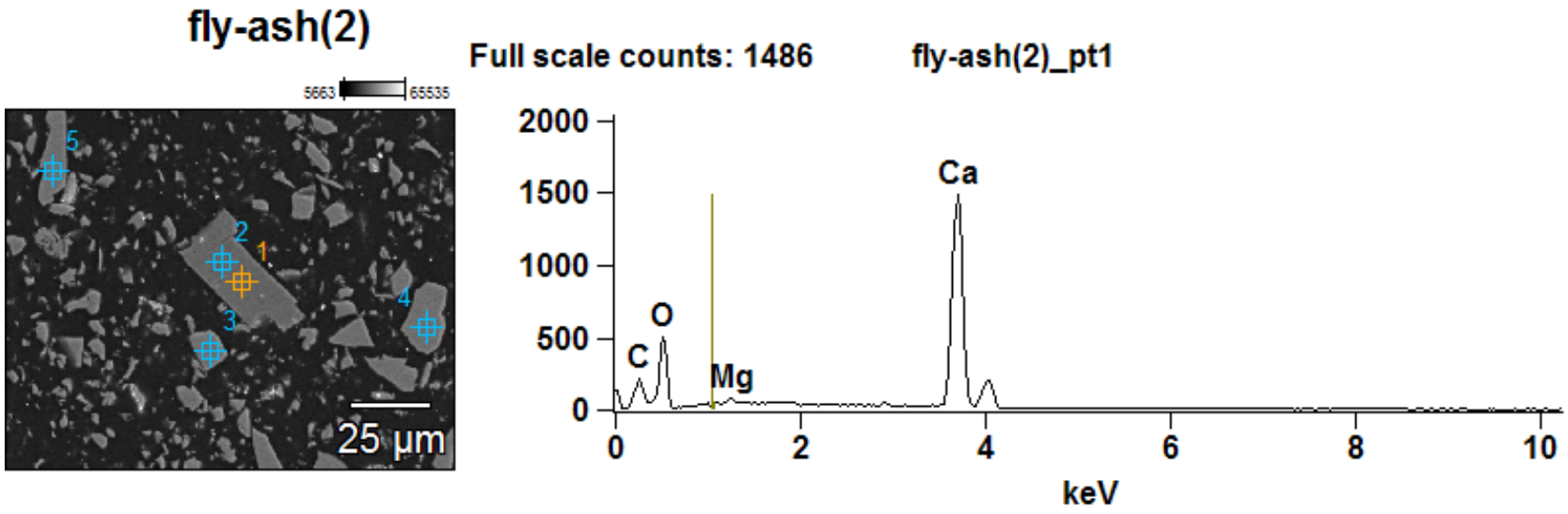

(a) (b)

Figure 32. (a) Backscatter electron image of fly ash (b) Elemental composition of fly ash points 1. Point 2 has similar elemental composition

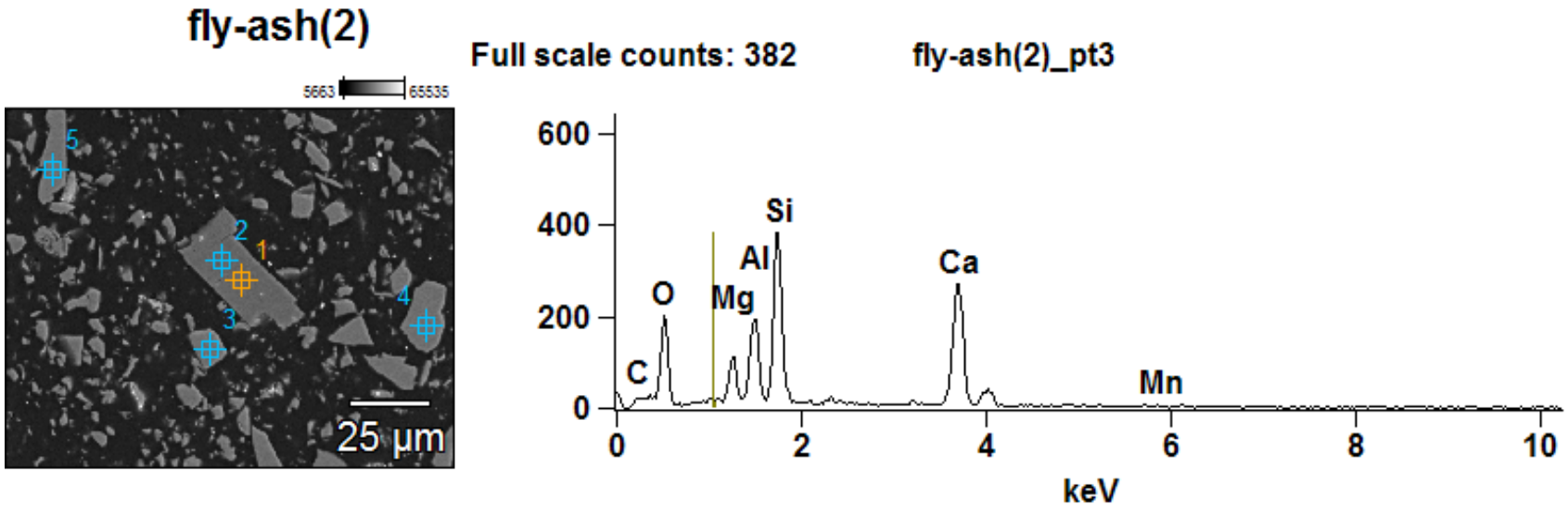

(a) (b)

Figure 33. (a) Backscatter electron image of fly ash (b) Elemental composition of fly ash point 3. Points 4 and 5 have similar elemental composition

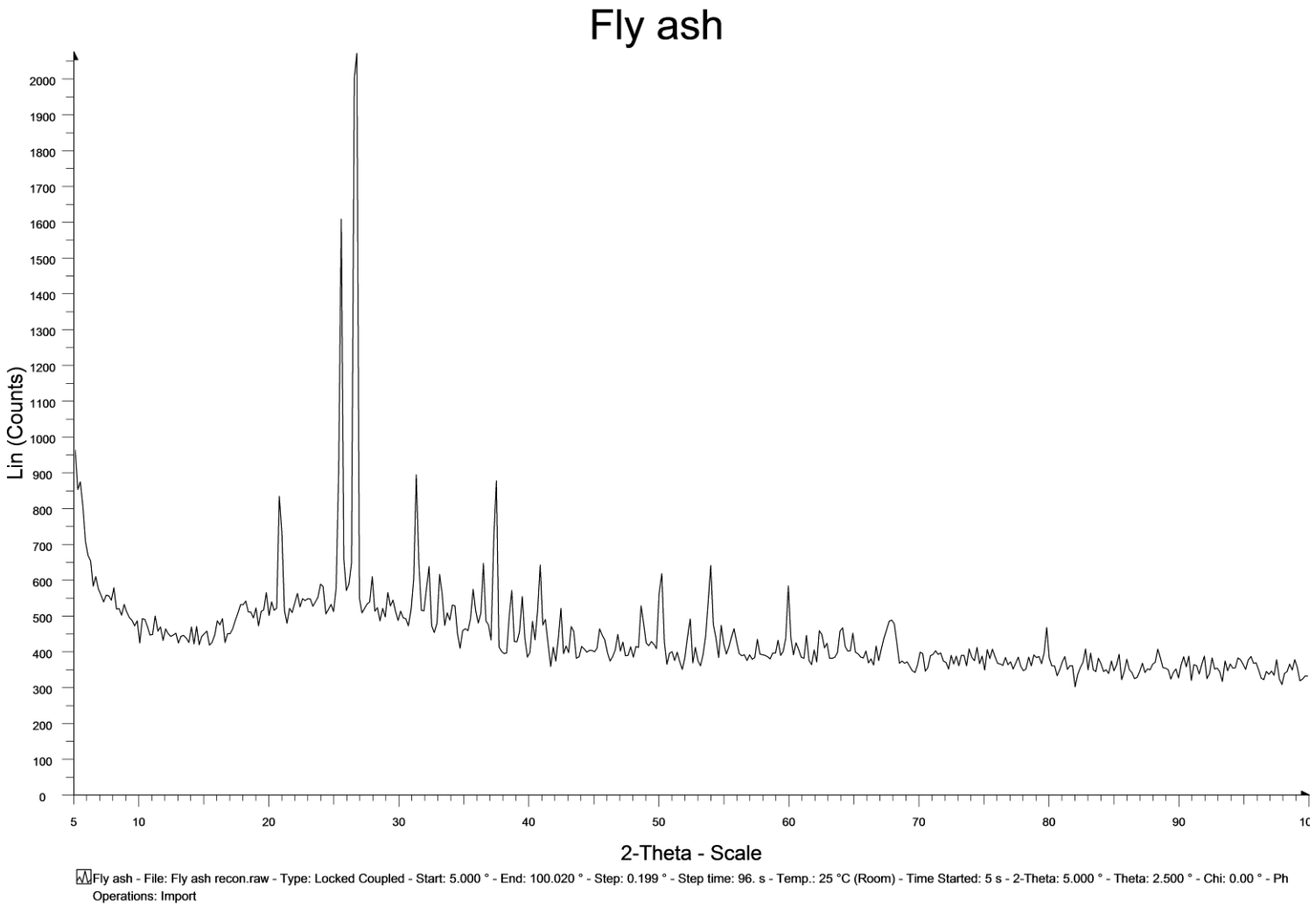

Figure 34. Raw XRD image of fly ash

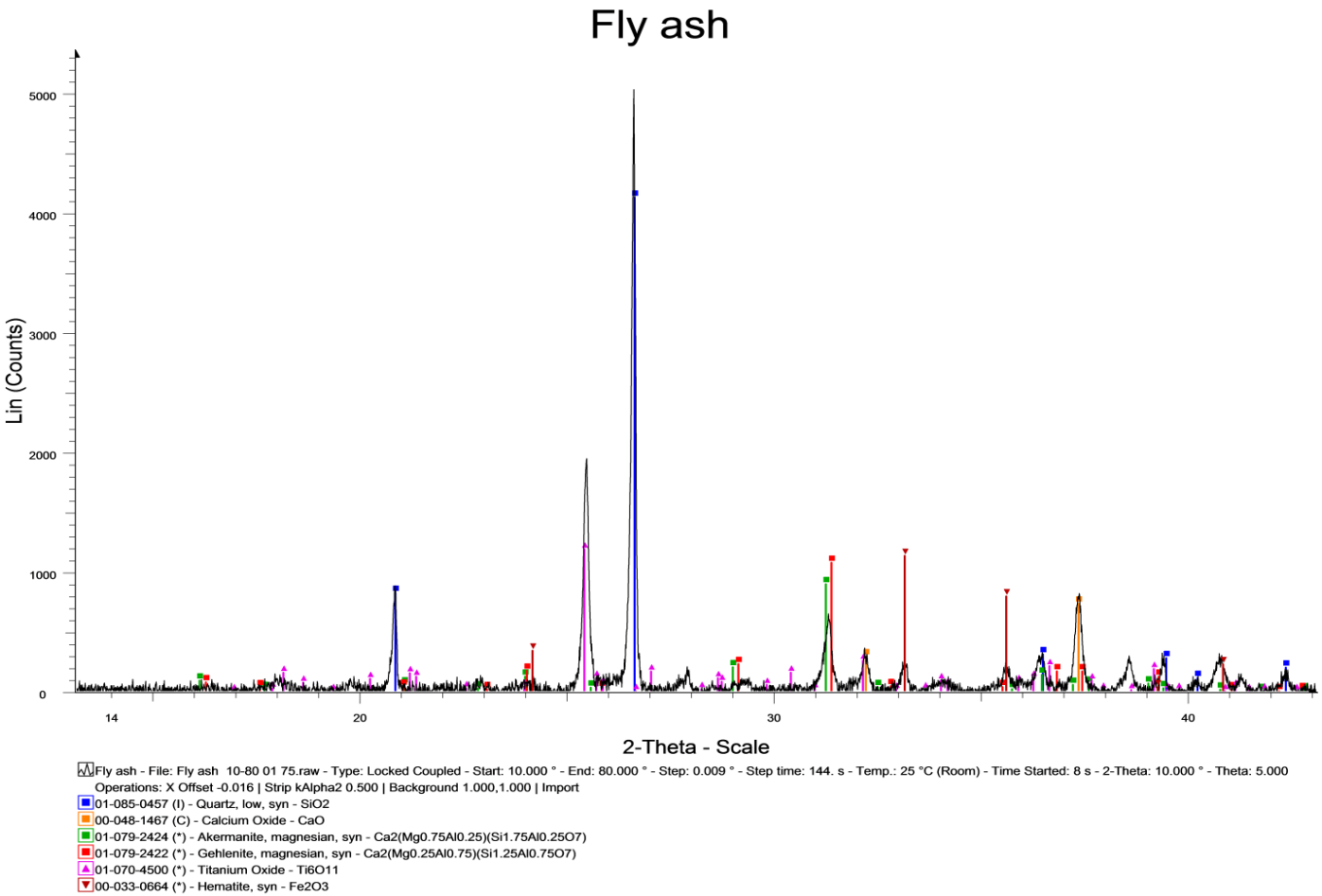

Figure 35. Smoothed XRD image of fly ash with quartz and calcium oxide

5.5.3 Lime

Only XRD was performed on the lime. The XRD image for lime, Figure 36, shows the presence of two mineralogical compounds: calcium oxide (CaO) and portlandite ($Ca(OH)_2$), both of which are rich in calcium. The lime, slag, and fly ash XRD signatures, all have calcium-rich peaks. The slag and fly ash are also silicon-rich. The presence of calcium- and silicon-rich compounds lend themselves well to the formation of calcium silicate hydrates in the presence of water.

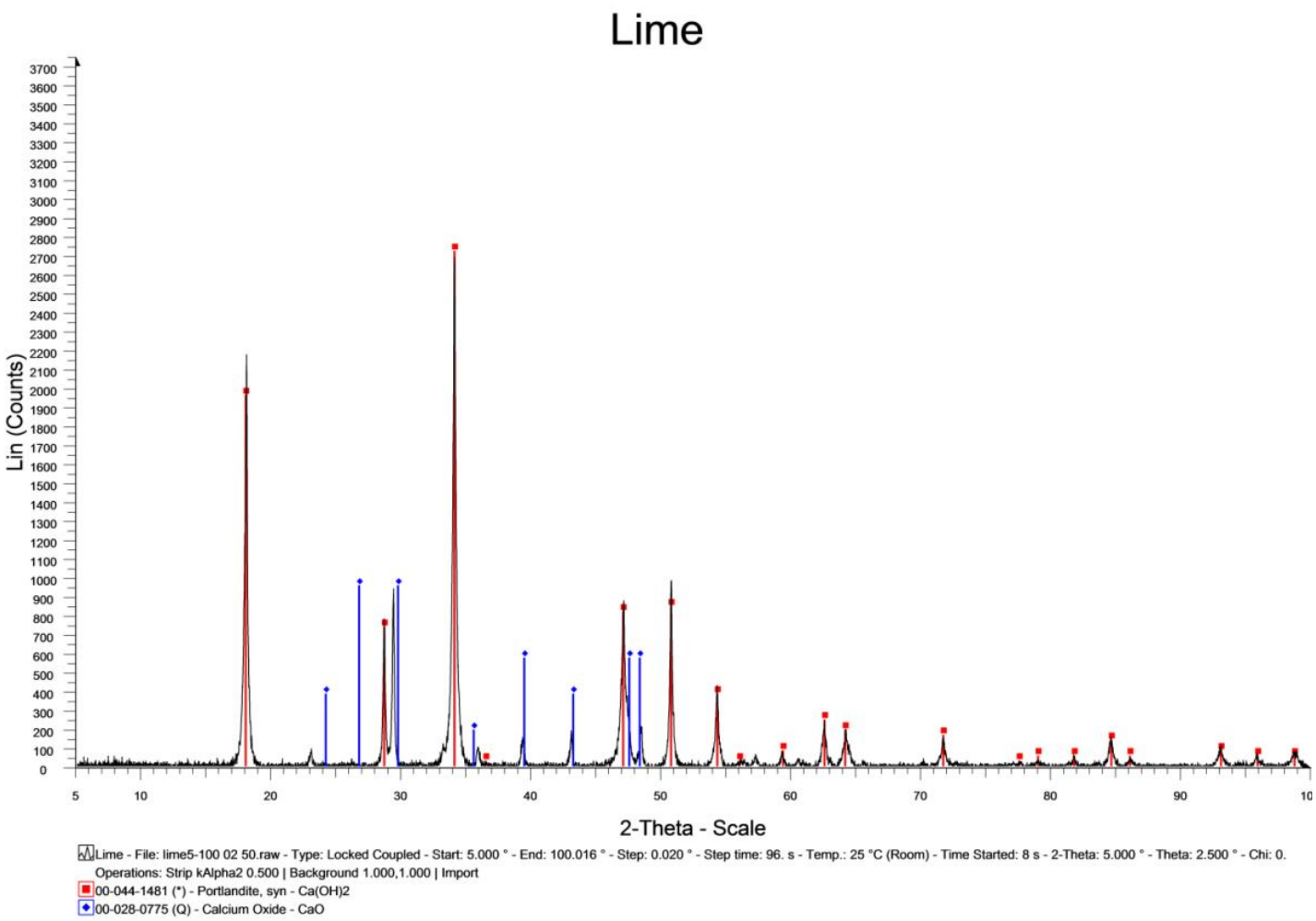

Figure 36. Smoothed XRD image of lime with calcium and portlandite mineralogical identification

5.5.4 Basalt

5.5.4.1 Basalt Petrography

The basalt portion of the thin sections of the geopolymer was observed using: (1) a microscope to conduct a petrographic analysis; and (2) SEM with EDS (see Section 5.6.1). The results indicate that the majority of the basalt fragments were plagioclase with some olivine and pyroxene.

5.5.4.2 Basalt Sand

Only XRD was performed on pulverized basalt sand. The raw XRD test results for the basalt sand are shown in green in Figure 37. Superimposed on the sample plot in black for comparison are those for a glassy basalt, that is not from this project. As seen in this figure, there is no glassy hump for the basalt sand from this project but there are rather many distinct peaks. On the other hand, the glassy basalt has a small hump. Thus, it can be concluded that the basalt sand does not have amorphous properties.

The mineralogical identities of the compounds present are indicated in Figure 38. The majority of the peaks are identified as anorthite sodian, augite and iron magnesium oxide. Anorthite is found in plagioclase, which belongs to the feldspar group whereas augite is a monoclinic pyroxene. Both the pyroxenes and feldspars are silicate minerals.

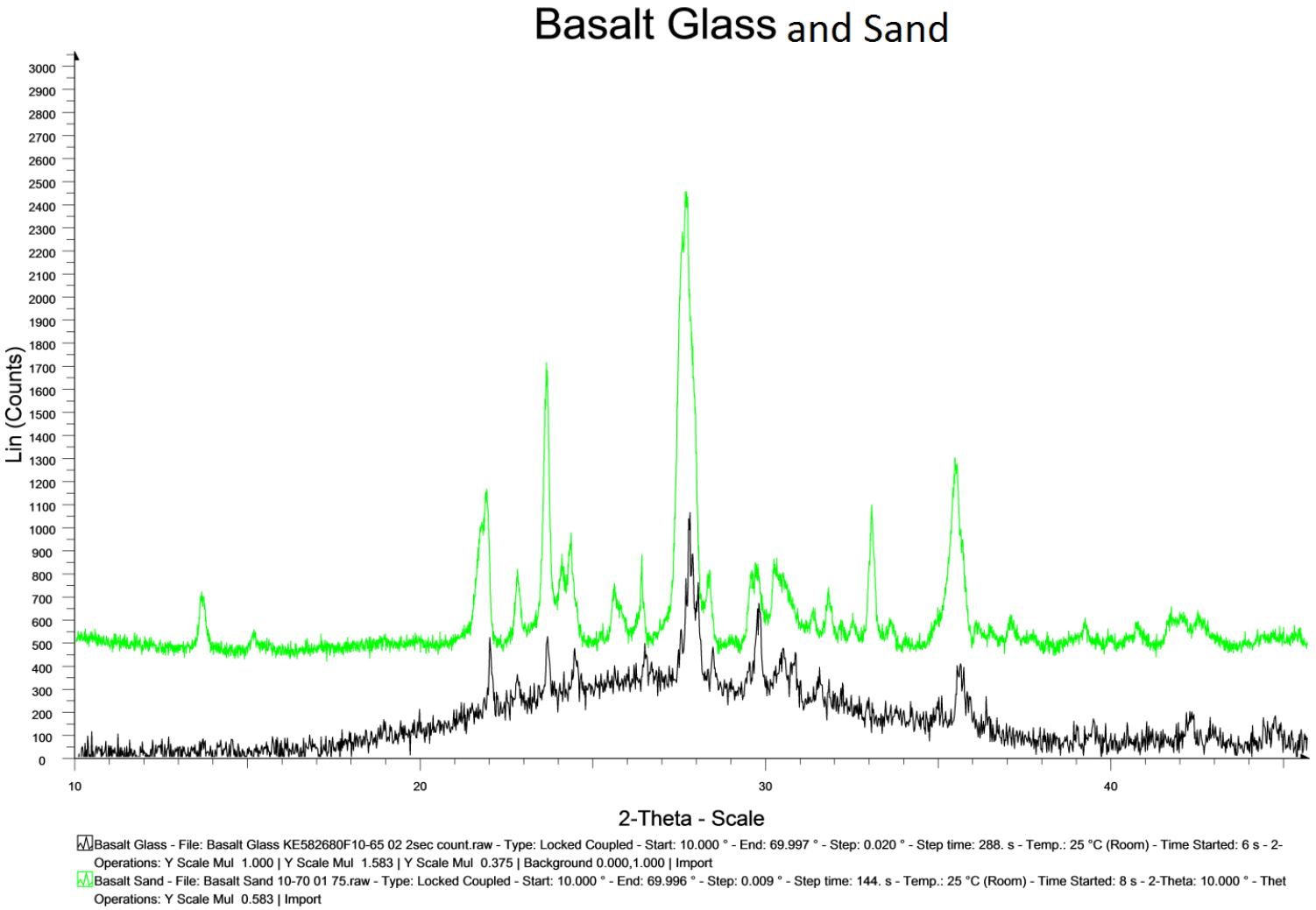

Figure 37. Raw XRD image of basalt sand and basalt glass

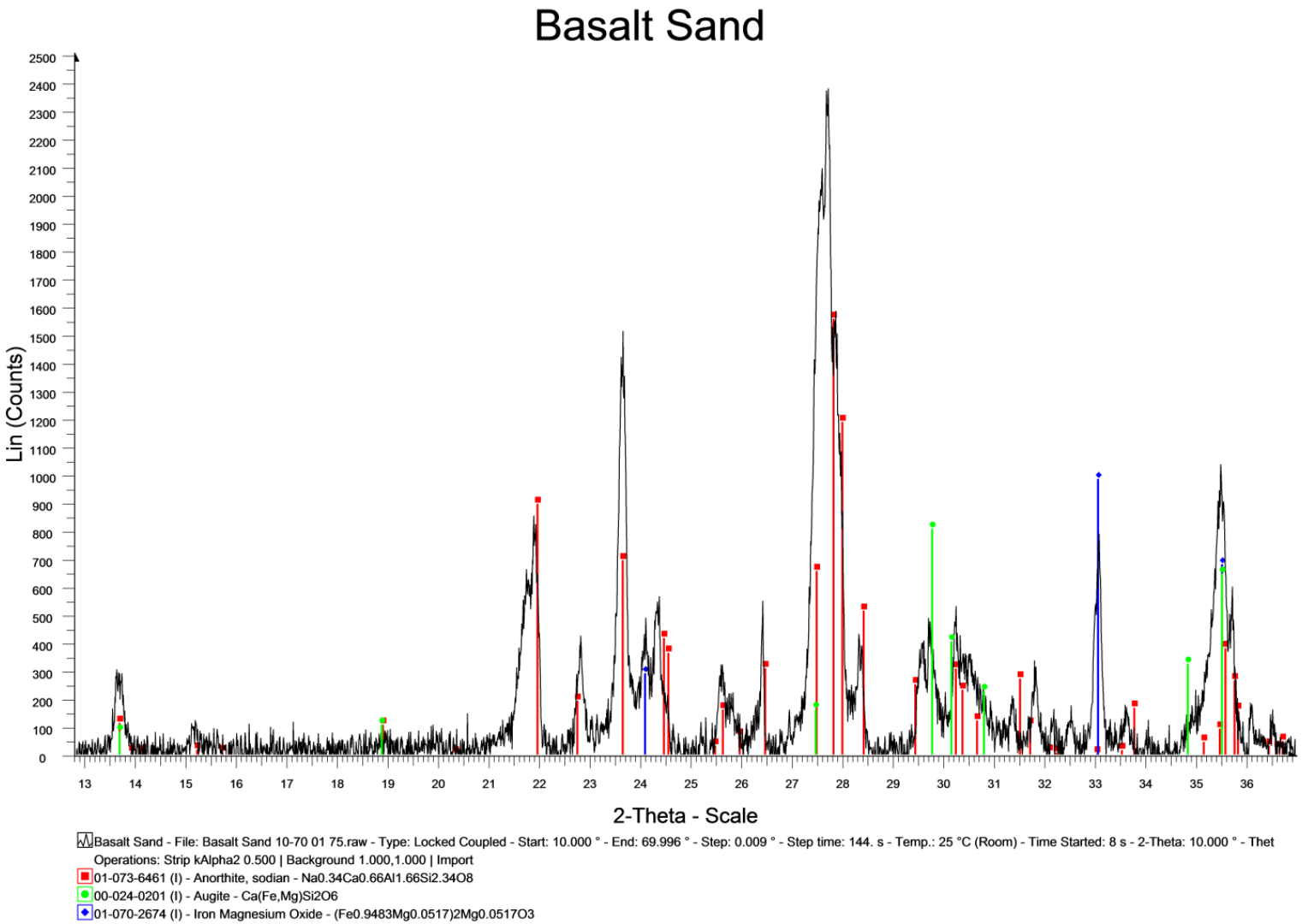

Figure 38. Smoothed XRD image of basalt sand with mineralogical identification

5.5.4.3 Basalt 1.5-inch Aggregate

Only XRD was performed on pulverized piece of a 1.5-inch basalt aggregate. The XRD results for this basalt aggregate are superimposed on those for the basalt sand from the preceding section in Figure 39. The graphs are slightly offset from each other, but the peaks are very similar. From Figure 39, it can be concluded that the basalt aggregate is almost identical to the basalt sand in terms of mineralogy.

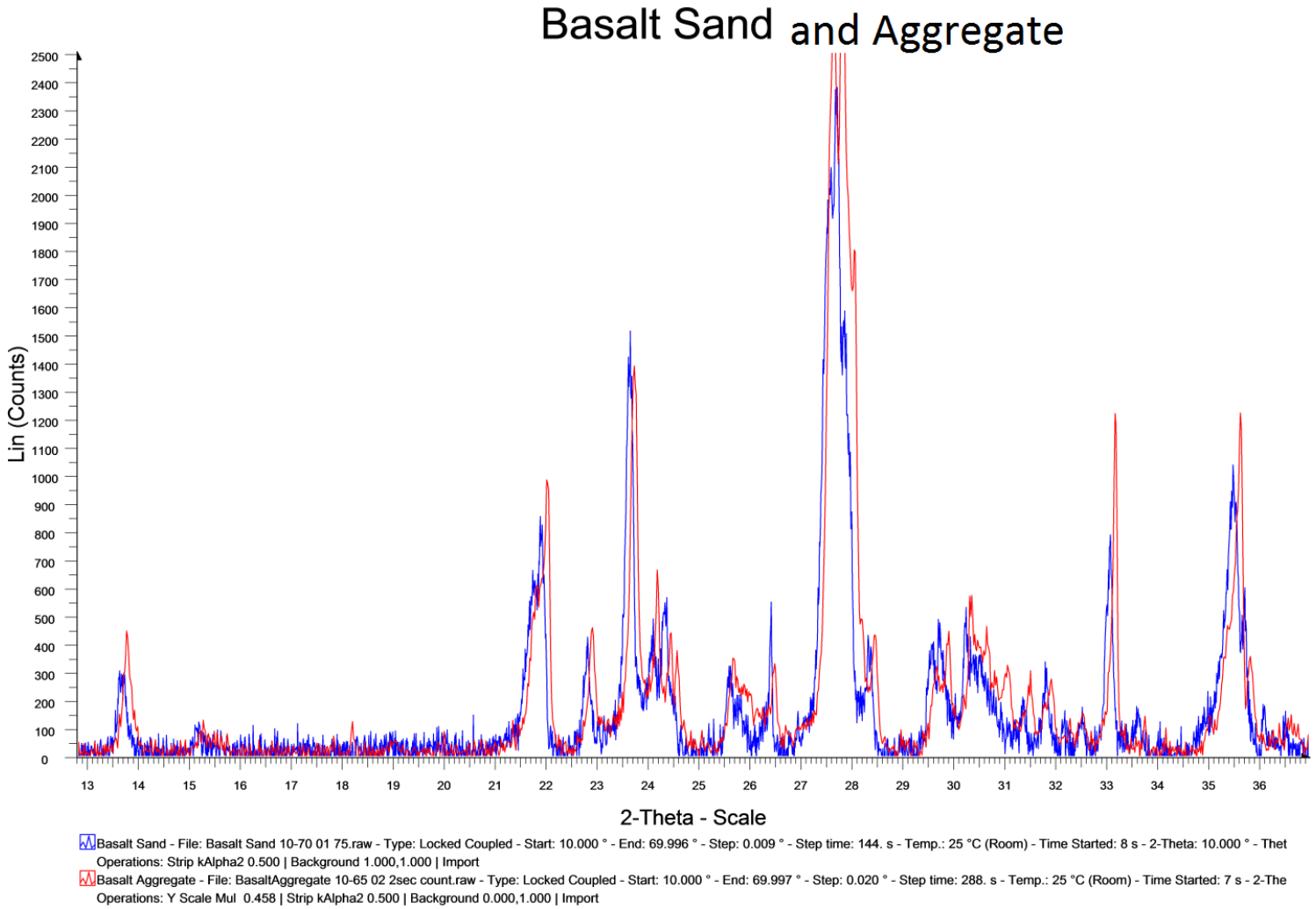

Figure 39. Smoothed XRD image of basalt sand and basalt aggregate

5.6 Mineralogical Results for the Geopolymer

Results of SEM with EDS and XRD analyses of the geopolymer are presented in this section.

5.6.1 SEM with EDS

SEM with EDS was conducted on both the basalt aggregate portion and the cementitious matrix portion of the geopolymer. Then, SEM with EDS results for the geopolymer as a whole are presented highlighting the three dominant compositional elements.

5.6.1.1 Basalt Aggregate

The SEM with EDS results for three points in the basalt aggregate in Thin Section No. 79 (Figure 23) are shown in Figure 40 through Figure 42. Figure 40 shows oxygen, iron and titanium present with traces of manganese and aluminum. No silicon was detected. Without the trace elements, this material is characteristic of an ulvöspinel. Figure 41 shows the presence of oxygen, iron, silicon and magnesium, suggesting that it may be olivine. Figure 42 shows oxygen, silicon, aluminum, sodium and calcium, which is characteristic of plagioclase.

5.6.1.2 Cementitious Matrix

The results for three regions of the cementitious matrix in Thin Section 79 are illustrated in Figure 43 through Figure 46 which contain both the SEM images and the elements detected using EDS. The elements dominantly present in Figure 43 include calcium, oxygen, and silicon. Figure 44 shows that the elemental composition is predominantly oxygen and silicon. In Figure 45, the dominant elements present include

calcium, oxygen, silicon and aluminum. Figure 46 shows that the elemental composition is primarily composed of silicon, calcium, oxygen and aluminum. These results suggest a cementitious matrix rich in calcium silicate hydrate and possibly some alumino-silicates.

5.6.1.3 Geopolymer

Based on the EDS results for the basalt and the cementitious matrix, it can be concluded that the three most common elements in the geopolymer other then oxygen are iron, silicon and calcium. The SEM images have varying grey intensities. Each intensity represents a different element present. The three minerals iron, silicon, and calcium had their own intensities that can be switched to a red, green or blue color in Photoshop. To investigate whether the basalt aggregate reacted with the lime/slag/fly ash mixture, the SEM images of Thin Section 80 (Figure 24) were imported into Photoshop and color coded to show these three dominant elements as follows: Red = iron, Green = silicon, Blue = calcium. These RGB images are shown in Figure 47 through Figure 52. In Figure 47 through Figure 49, a dark film surrounding the basalt aggregate is observed. Upon first glance it was thought that the dark film was due to some kind of reaction between the plagioclase in the basalt and the compounds present in the cementitious matrix. However, upon close examination, the iron-titanium oxide grains (red specks in the color images) within the basalt aggregate were not present in the band of dark film. If the basalt aggregate had reacted, the iron titanium oxide grains should still be visible in the dark film. Therefore, it was inconclusive as to what this film may be. One possible explanation is that the dark film is a result of how the thin section was polished. The basalt is a hard material and easy to polish whereas the matrix is soft and

could have smeared during polishing.

While a few RGB colored images showed a dark film around the basalt aggregate edges, there were some that had no such dark borders. In Figure 50 through Figure 52, there were clear and distinct border lines between the basalt and the cementitious matrix. These images conclusively show that the basalt and the cementitious matrix did not react with each other.

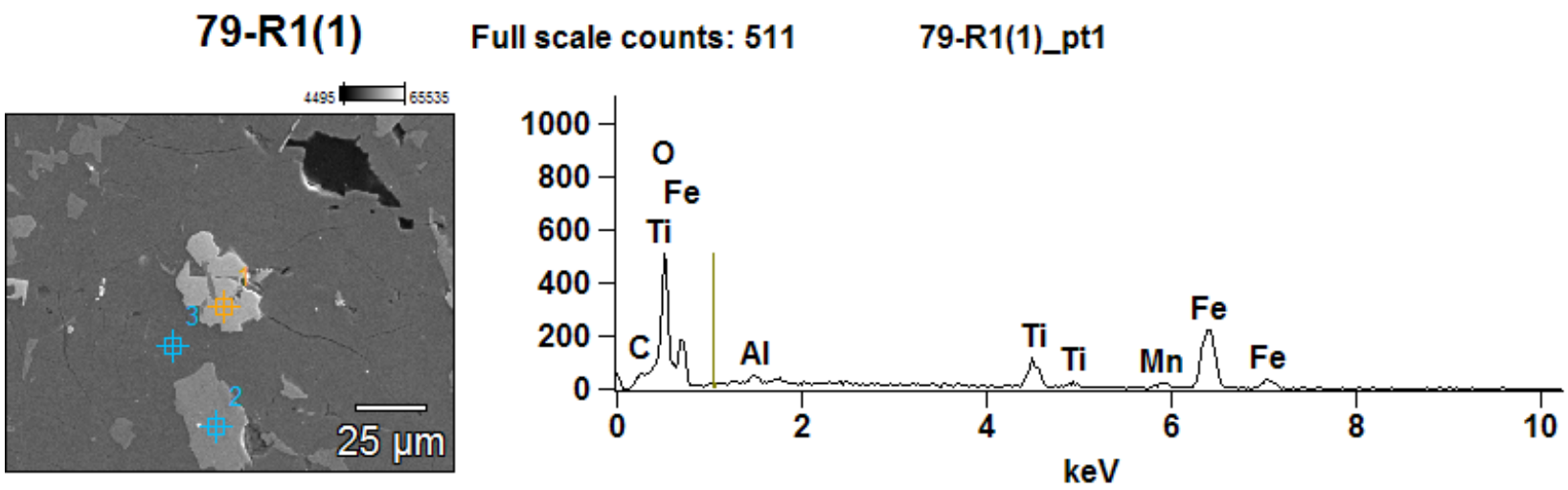

(a) (b)

Figure 40. (a) Backscatter electron image of basalt in the geopolymer (b) elemental composition of point 1 consisting predominantly of oxygen, titanium and iron suggesting and ulvöspinel.

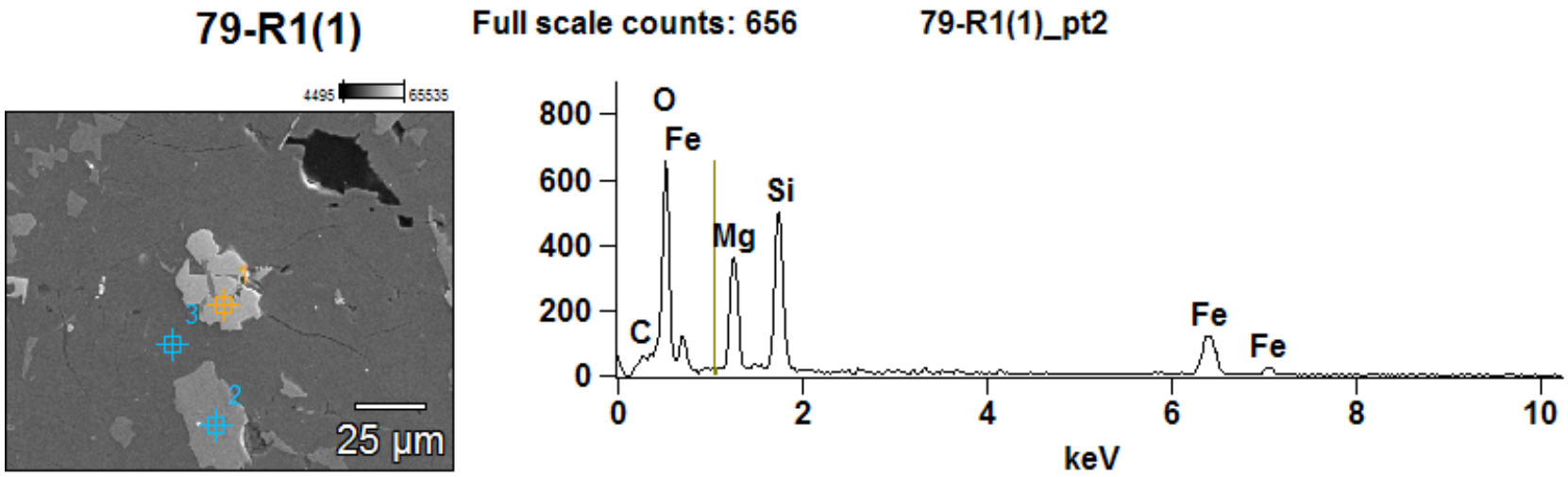

(a) (b)

Figure 41. (a) Backscatter electron image of basalt in the geopolymer (b) Elemental composition of point 2 consisting predominantly of oxygen, silicon, and magnesium and iron suggesting an olivine.

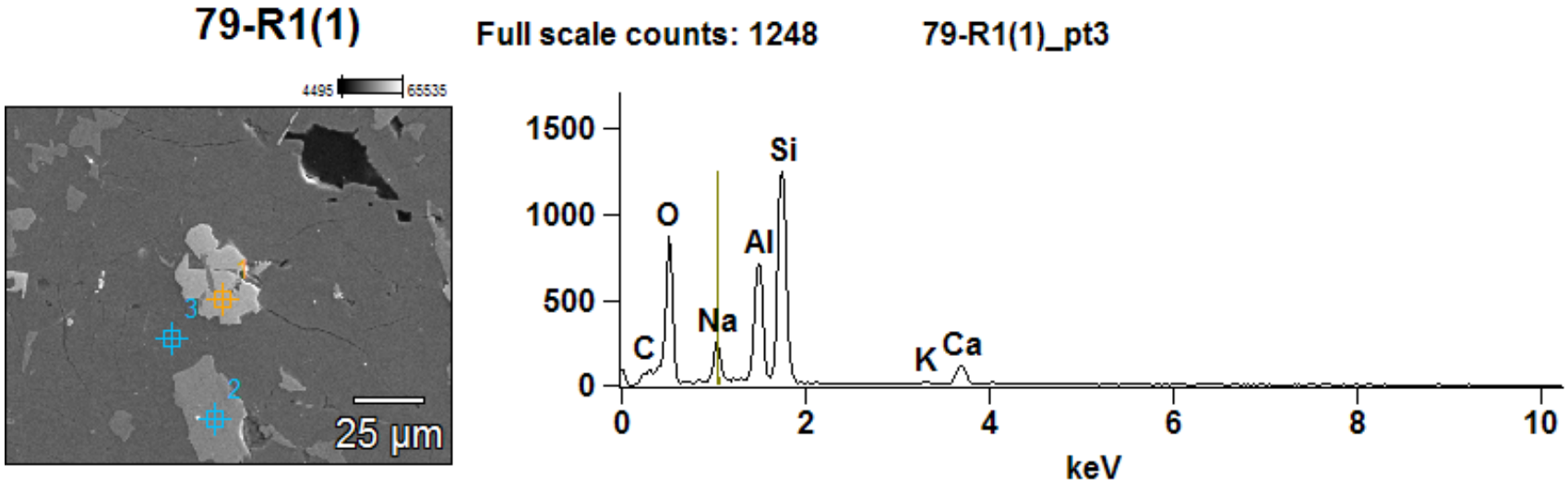

(a) (b)

Figure 42. (a) Backscatter electron image of basalt in the geopolymer (b) Elemental composition of point 3 consisting predominantly of oxygen, silicon, aluminum and sodium suggesting plagioclase.

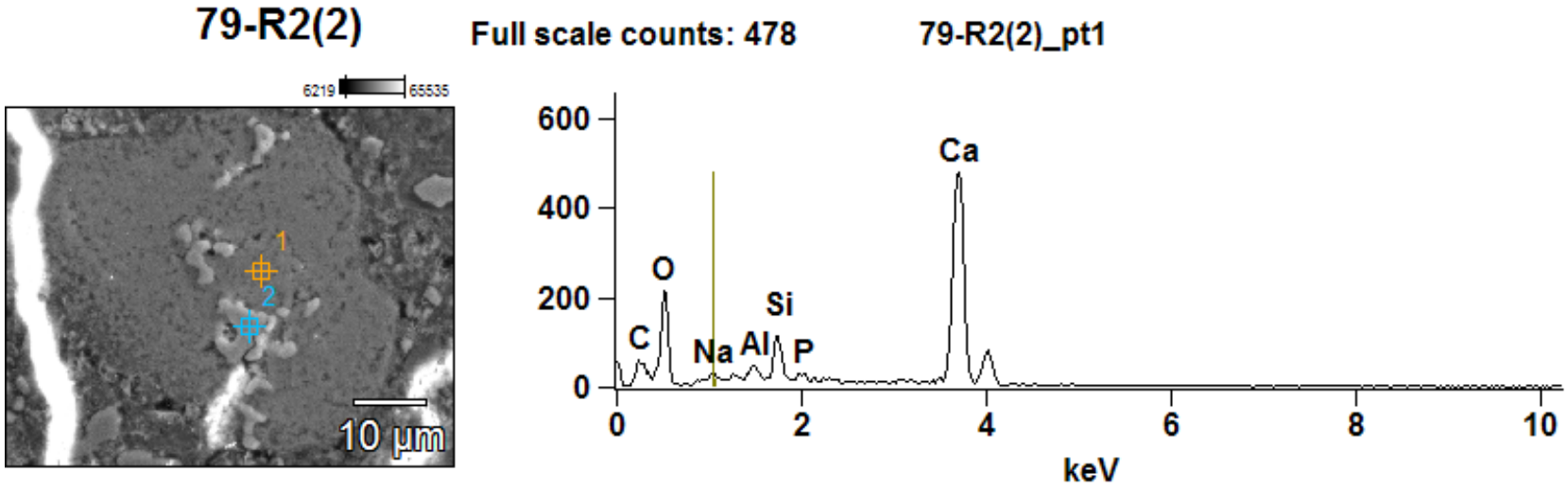

(a) (b)

Figure 43. (a) Backscatter electron image of cementitious matrix in the geopolymer (b) Elemental composition consisting predominantly of oxygen, calcium and silicon

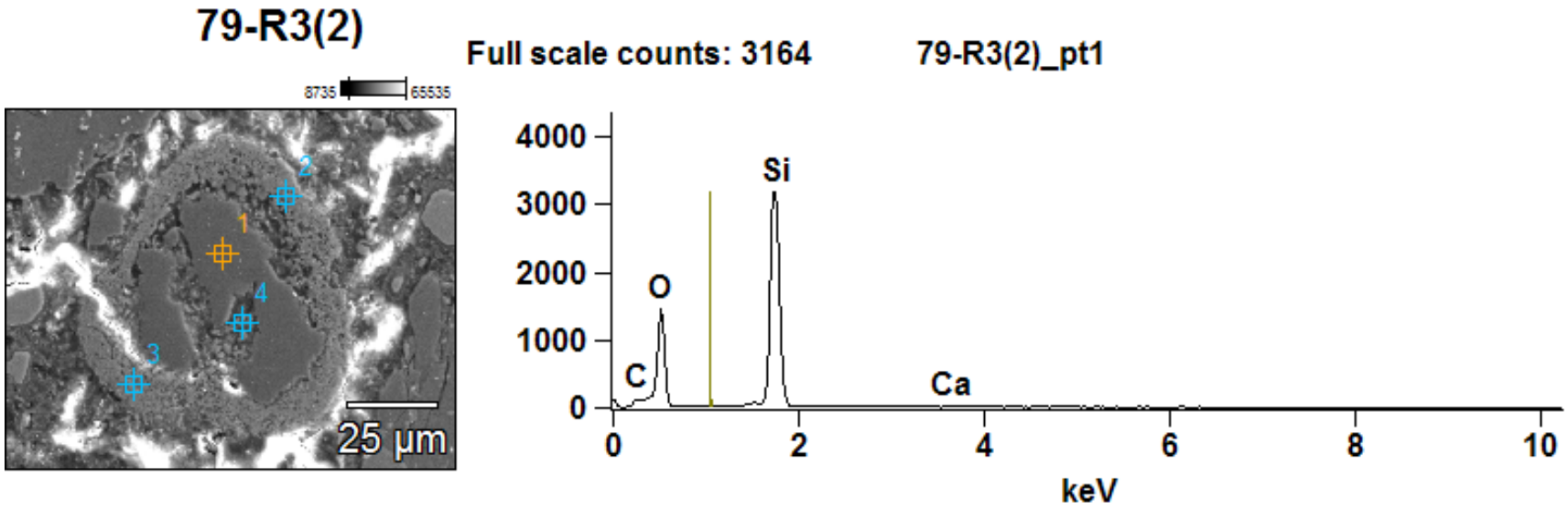

(a) (b)

Figure 44. (a) Backscatter electron image of cementitious matrix in the geopolymer (b) Elemental composition consisting predominantly of oxygen and silicon.

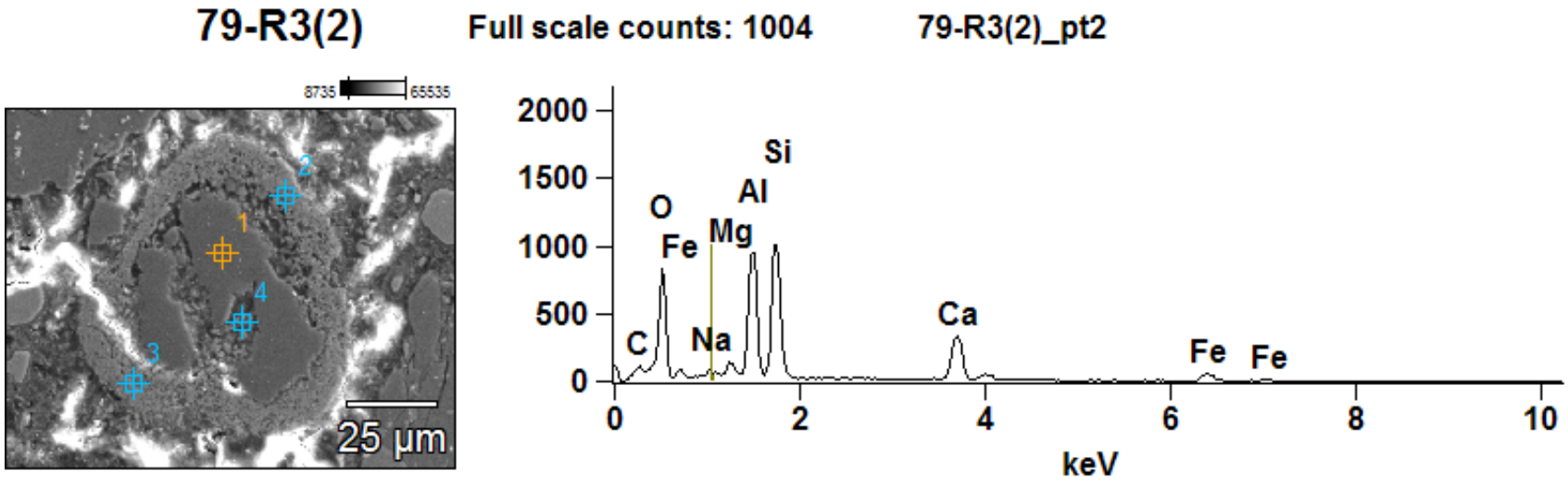

(a) (b)

Figure 45. (a) Backscatter electron image of cementitious matrix in the geopolymer (b) Elemental composition consisting predominantly silicon, aluminum, oxygen and calcium.

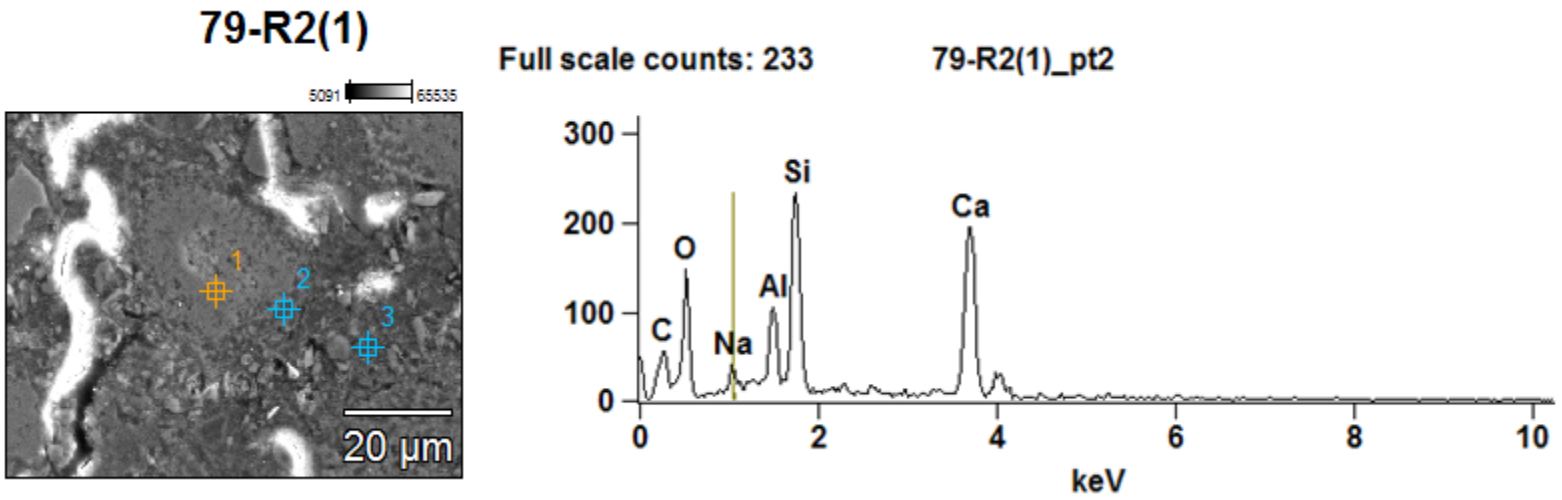

(a) (b)

Figure 46. (a) Backscatter electron image of cementitious matrix in the geopolymer (b) Elemental composition consisting predominantly of oxygen, silicon, calcium, and aluminum

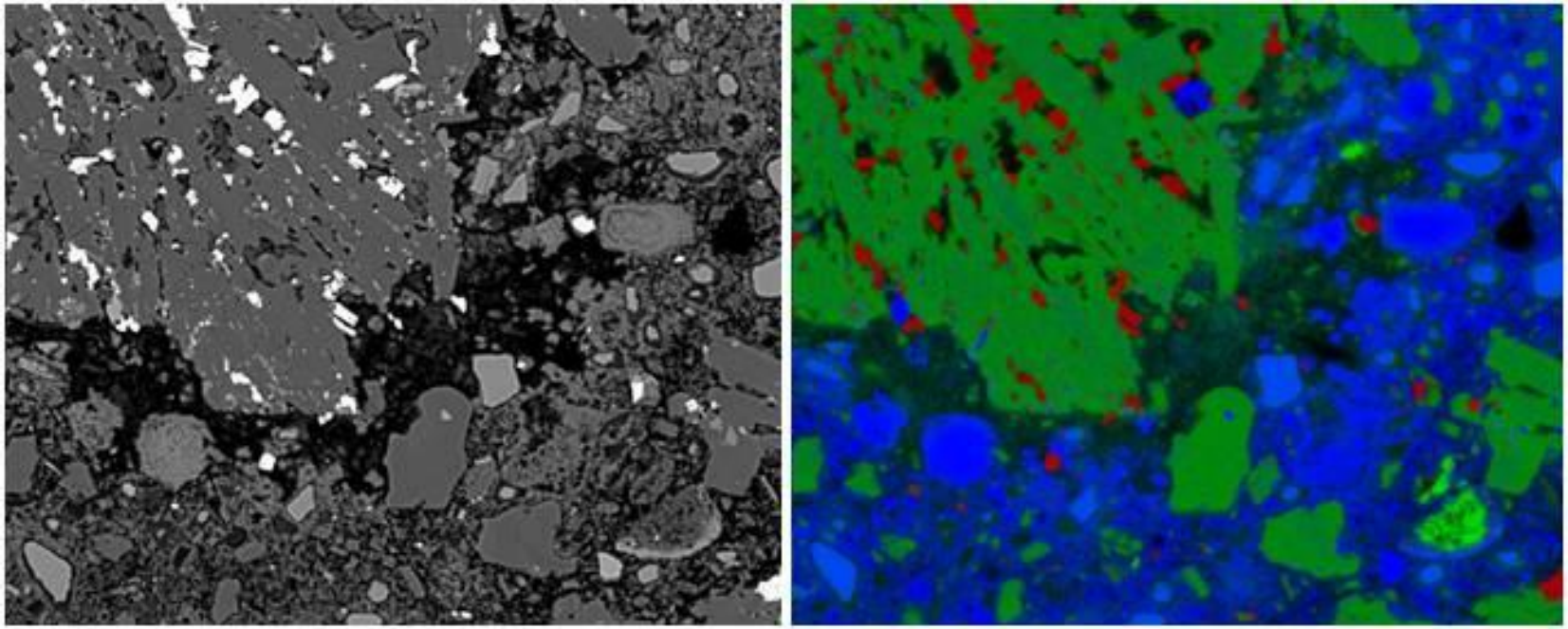

(a) (b)

Figure 47. (a) Backscatter electron image of geopolymer Thin Section No. 80 Region 1 (b) RGB colored image of geopolymer with dark film surrounding the basalt aggregate in green. The width of the image is 200 µm

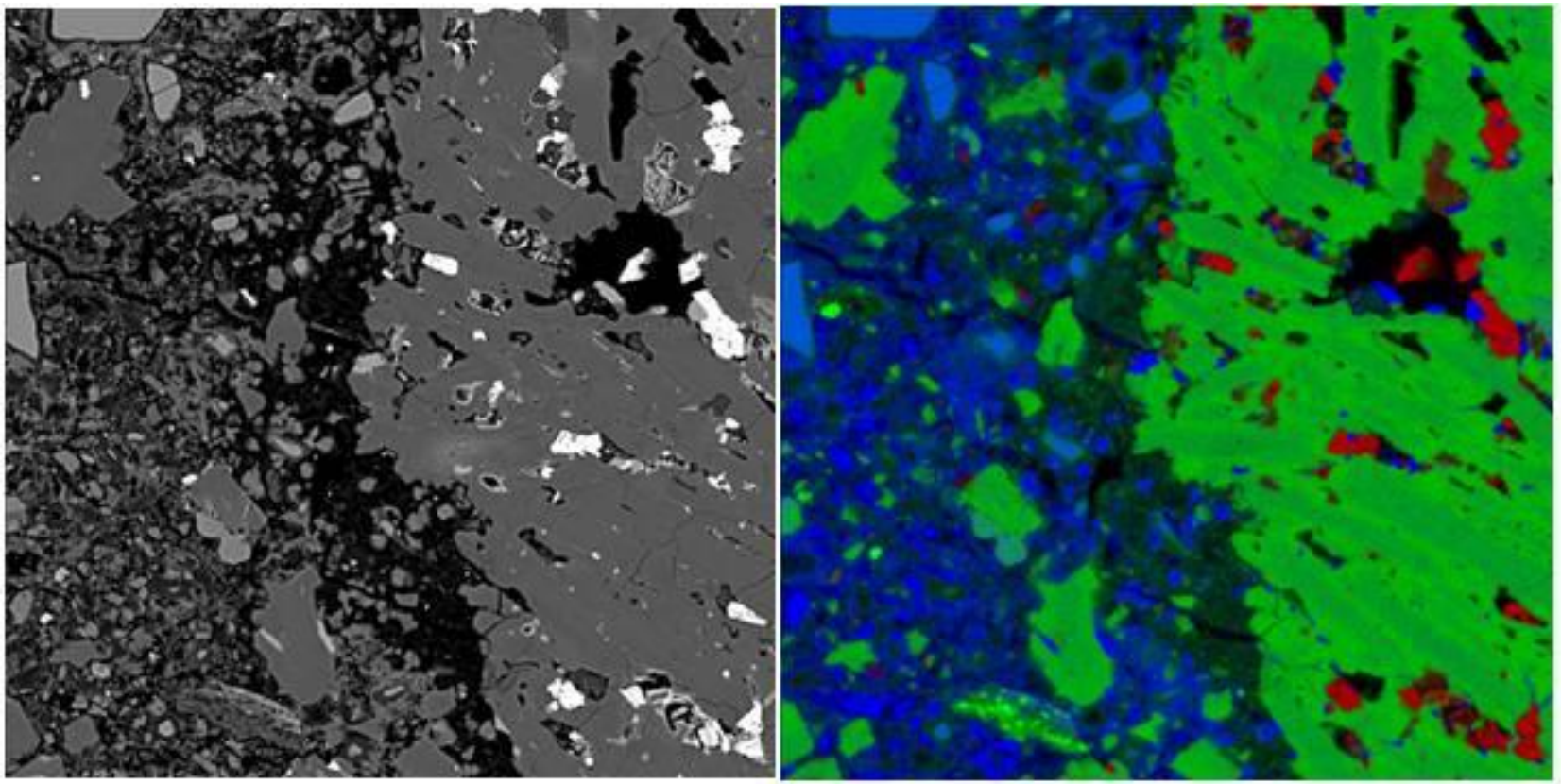

(a) (b)

Figure 48. (a) Backscatter electron image of geopolymer Thin Section No. 80 Region 2 (b) RGB colored image of geopolymer with dark film surrounding the basalt aggregate. The width of the image is 200 µm

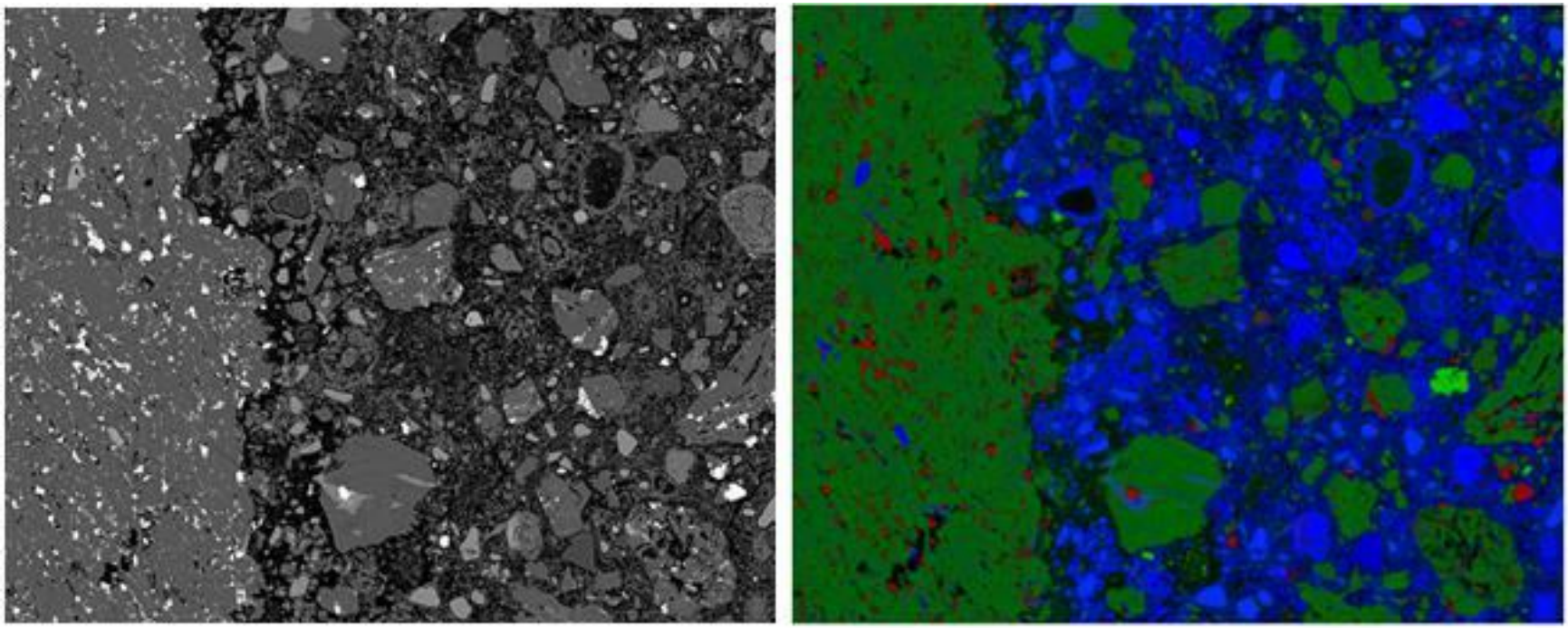

(a) (b)

Figure 49. (a) Backscatter electron image of geopolymer Thin Section No. 80 Region 3 (b) RGB colored image of geopolymer with dark film surrounding the basalt aggregate. The width of the image is 500 µm

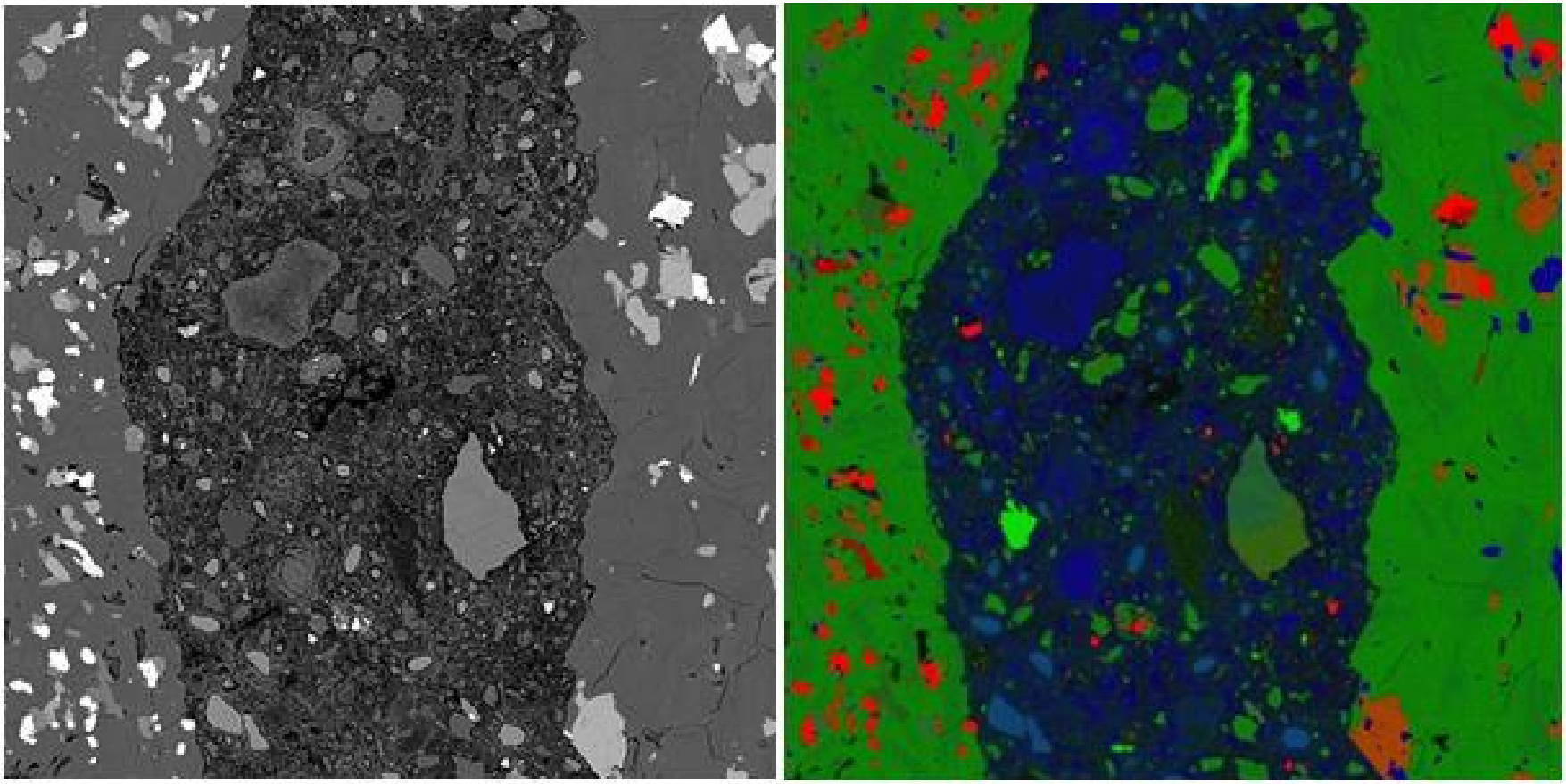

(a) (b)

Figure 50. (a) Backscatter electron image of geopolymer Thin Section No. 80 Region 4 (b) RGB colored image of geopolymer with no dark film around the edge of the basalt. The width of the image is 400 μm

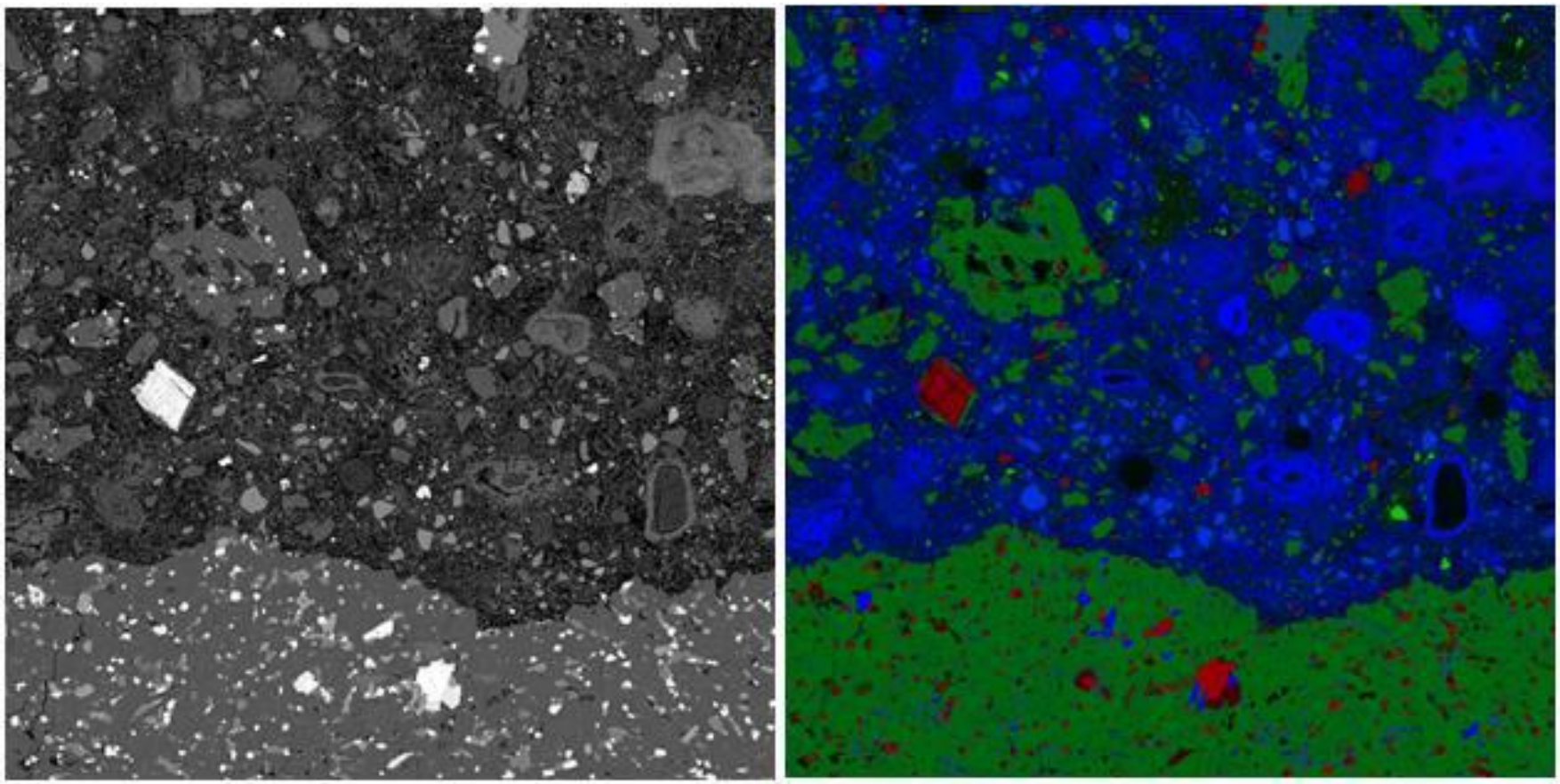

(a) (b)

Figure 51. (a) Backscatter electron image of geopolymer Thin Section No. 80 Region 5 (b) RGB colored image of geopolymer with no dark film around the edge of the basalt. The width of the image is 700 µm

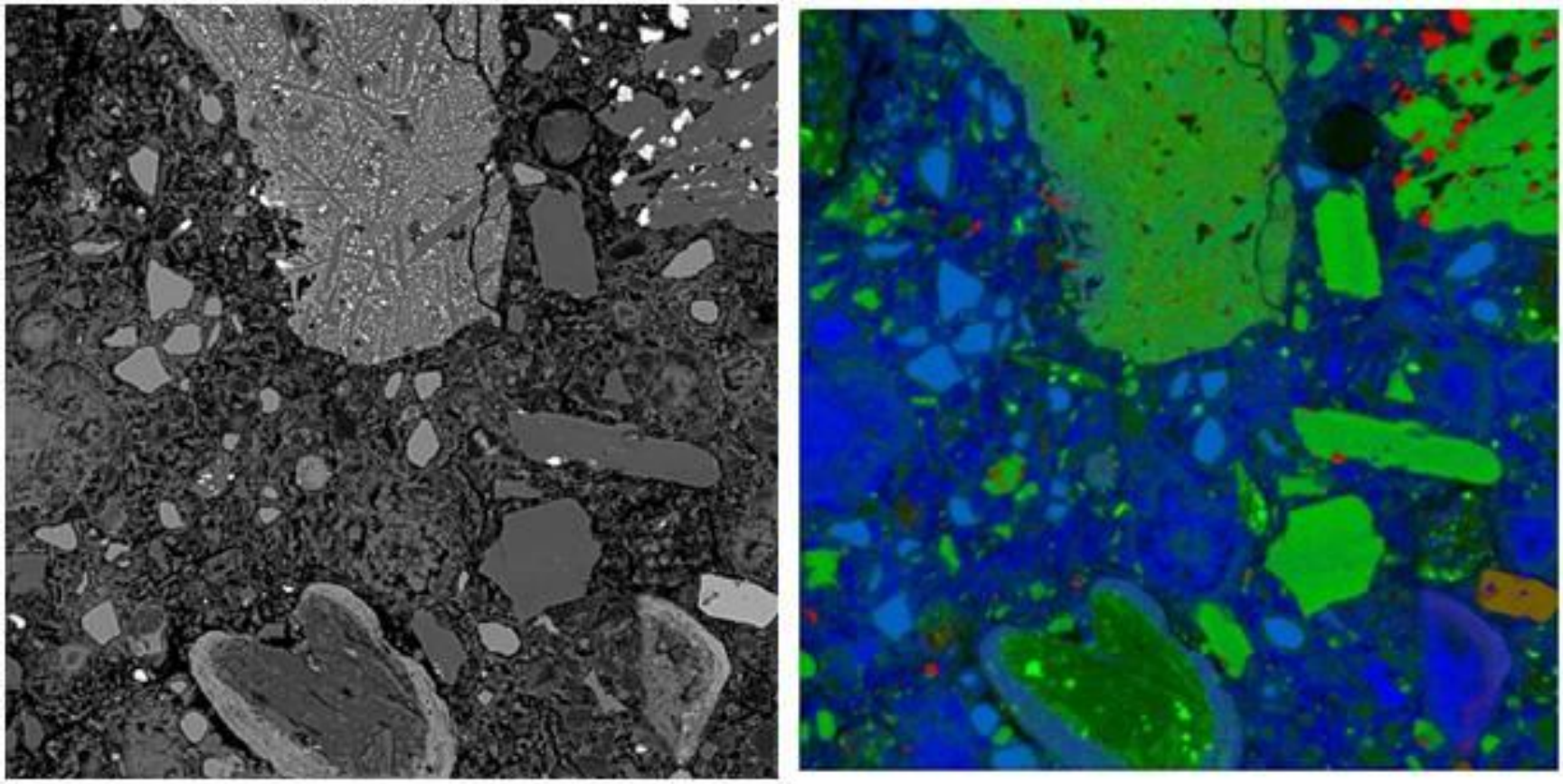

(a) (b)

Figure 52. (a) Backscatter electron image of geopolymer Thin Section No. 80 Region 6 (b) RGB colored image of geopolymer with no dark film around the basalt. The width of the image is 240 μm

5.6.2 XRD

Figure 53 shows the raw XRD results for the geopolymer. Since the chemicals have already reacted, there is no more amorphous hump that was observed in the slag and fly ash.

In Figure 54, the main three mineralogical compounds identified in the geopolymer include calcite, aragonite, and anorthite sodian highlighted in red, green, and blue respectively. Calcite and aragonite are forms of calcium carbonate and is an expected hydration product of the cementitious reaction involving the geopolymer ingredients. An expected major geopolymer hydration product is calcium silicate hydrate, which is amorphous and not detectable by XRD. Anorthite is the primary component in basalt.

Figure 55 shows the similarity of the peaks between the geopolymer (blue) and the basalt sand (red). This figure emphasizes that the basalt aggregate and sand are the primary constituents in the geopolymer. The peaks that were not accounted for by the basalt sand match very closely with those of calcite as shown in Figure 56.

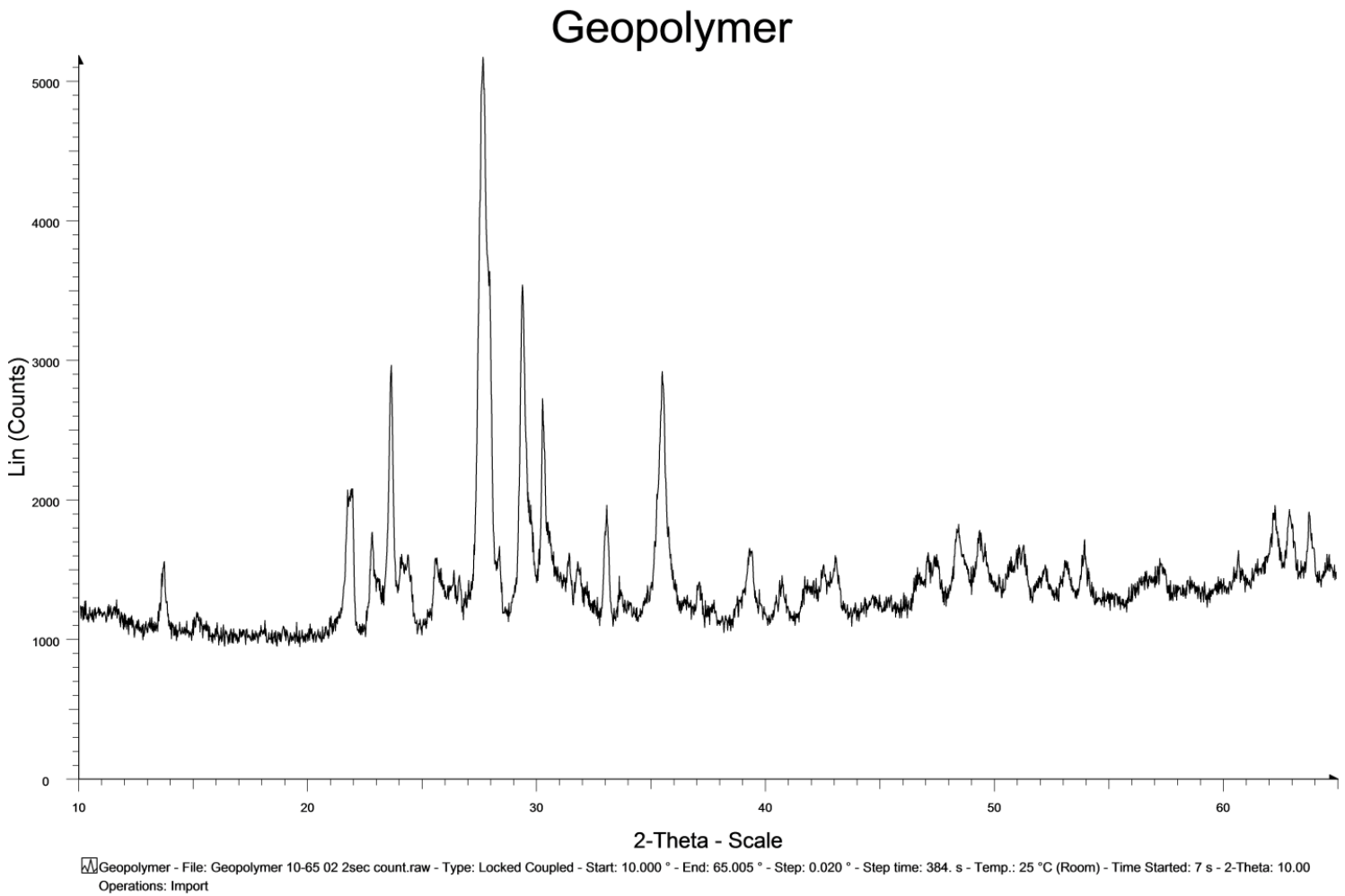

Figure 53. Raw XRD image of geopolymer

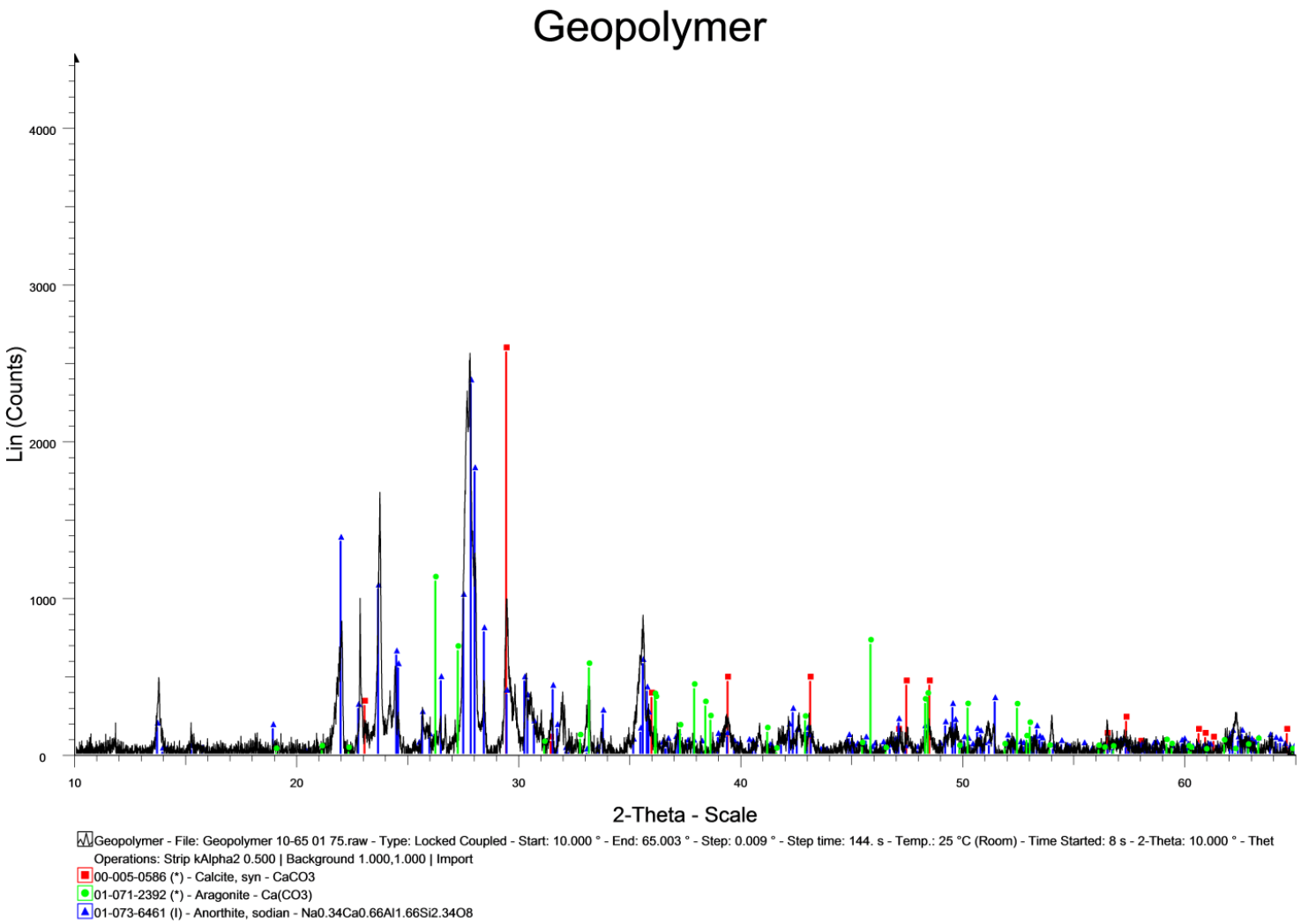

Figure 54. Smoothed XRD image of geopolymer with calcite, aragonite, anorthite, sodian mineralogical identifications

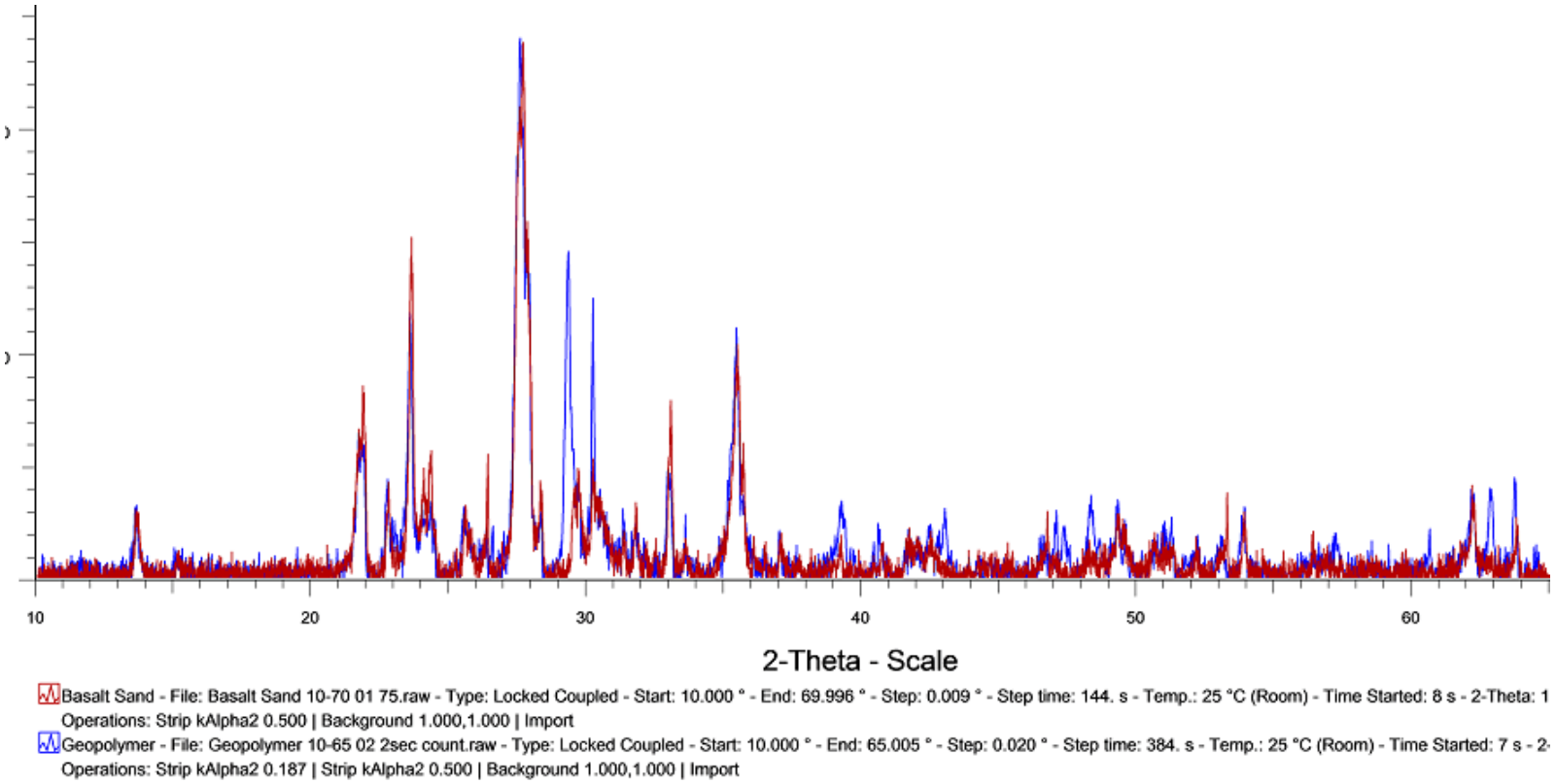

Figure 55. XRD image of geopolymer overlaid with XRD image of basalt sand

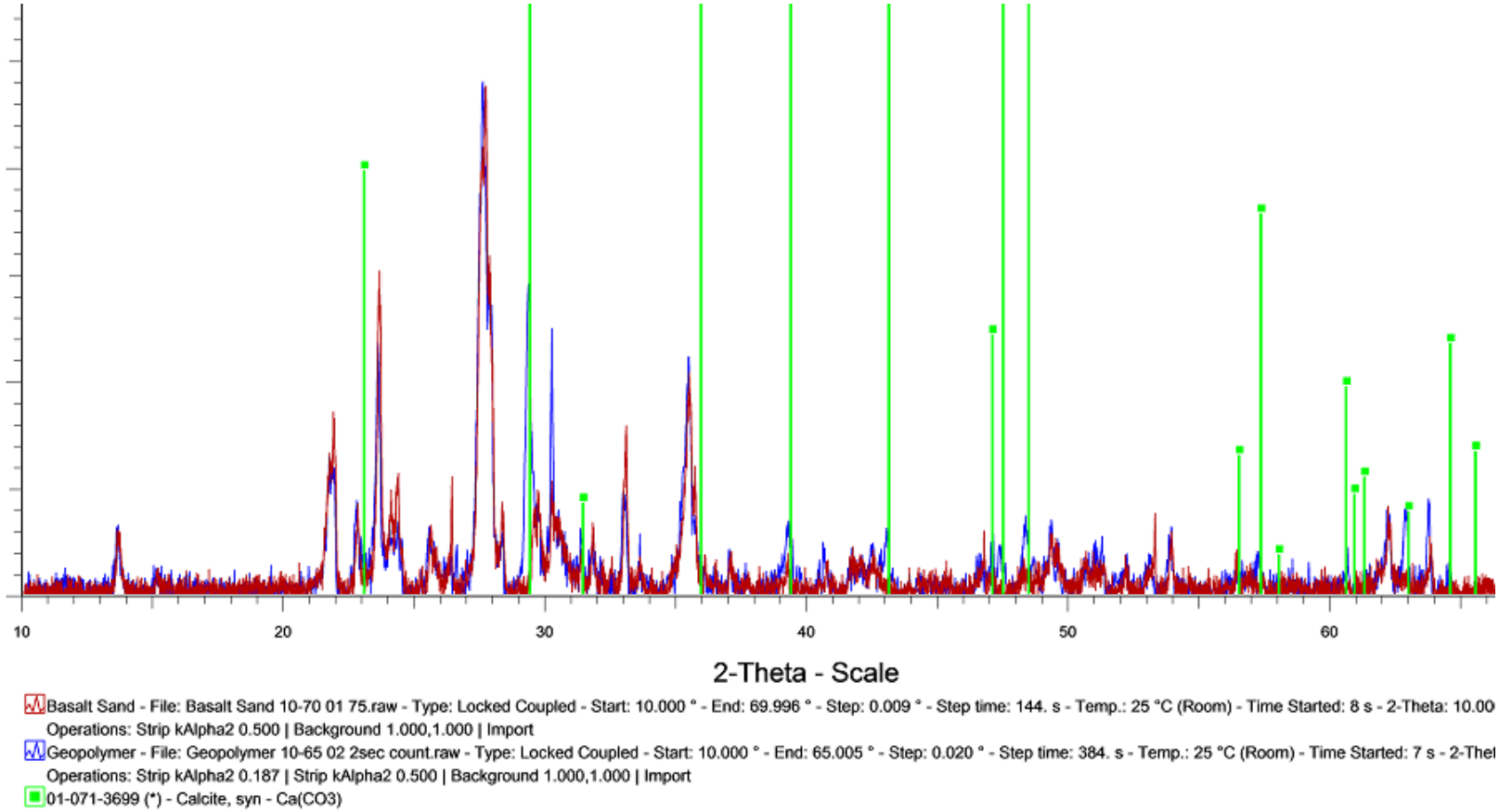

Figure 56. XRD images of geopolymer and basalt sand overlaid with calcite mineralogical identification

5.7 Conclusions

In order to understand the mineralogical make-up of the geopolymer concrete and to determine if there was any reaction between the basalt aggregate and the cementitious matrix, XRF was performed on the slag and fly ash, SEM with EDS was performed on slag, fly ash and thin sections of the geopolymer, and XRD analysis was performed on slag, fly ash, lime, soda ash, basalt sand, basalt aggregate and the geopolymer. From these analyses the following conclusions are offered.

1. XRF analyses indicate that the slag and fly ash are rich in CaO, SiO_2 and Al_2O_3 with the following percent composition:

	Slag	Fly Ash
CaO	43%	22%
SiO_2	33%	40%
Al_2O_3	15%	19%

2. The major crystalline compounds of the geopolymer and ingredients detected using XRD are summarized below.

Material	Primary Crystalline Compounds
Slag	Calcium sulfate and calcium sulfate hydrates
Fly ash	Silicon dioxide and calcium oxide
Basalt	Anorthite, augite and iron magnesium oxide
Geopolymer	Calcite, aragonite and anorthite

   XRD cannot detect amorphous compounds such as calcium alumino-silicate if present in the slag or calcium silicate hydrate if present in the geopolymer.

3. XRD results indicate that the slag and fly ash are amorphous or glassy as characterized by the presence of a low gentle hump in the XRD signature. However, the basalt sand and aggregate obtained from the island of Hawaii for this project are completely crystallized (not glassy or amorphous), consisting

of common basaltic minerals such as plagioclase, pyroxene and iron magnesium oxide. This is reinforced by the RGB images of the thin sections where there was no sign of reactivity at the border of the basalt and cementitious matrix.

4. Calcium, silicon and oxygen were detected in the cementitious matrix via EDS. These results suggest the presence of a calcium silicate hydrate with calcite or aragonite in the mix.
5. There was no evidence of a reaction between the basalt aggregate and the cementitious matrix. Typically, there is also no such reaction occurring in Portland cement concrete either. Should such a reaction occur, it is possible that it could be alkali-silica-reaction (ASR), which is highly undesirable as it can compromise the later strength of the geopolymer.

CHAPTER 6. SUMMARY AND CONCLUSIONS

The following summarizes the findings for the basalt aggregate index tests.

- Based on the specific gravity and absorption tests, the fine aggregate has lower specific gravities and higher absorptions than the coarse aggregate. The results also meet the State of Hawaii Department of Transportation or HDOT (2005) specifications requirement that for coarse aggregate used in concrete mixes, the maximum absorption should be 6%. HDOT has no absorption requirements for fine aggregate.
- The L.A. abrasion values for gradings A and B were 30.3% and 26.8%, respectively. This meets the State of Hawaii Department of Transportation (2005) specifications requirement that for aggregate used in concrete mixes, the maximum L.A. abrasion should be 40%.
- The minimum and maximum dry unit weights of the basalt are 16.8 and 20.3 kN/m^3, respectively.
- The SE value for the basalt sand and aggregate was measured to be 72%. This meets the State of Hawaii Department of Transportation (2005) specifications minimum SE requirement for fine aggregate used in concrete mixes of 70%. This high SE value indicates a high percentage of sand and silt size particles in the finer grained portion of the basalt.
- The uncompacted void content provides an indication of the aggregates' angularity, sphericity, and the surface texture. The average uncompacted

void content was 47.5%.

The following summarizes the results of the strength and flexural tests.

- 28-day compressive strengths of the 6-inch diameter geopolymer cylinders ranged from 1154 to 2618 psi with an average of 1926 psi. This strength range represents 29% to 65% with an average of 48% of regular construction grade concrete having a 28-day design compressive strength of 4000 psi.
- 29-day compressive strengths of the 2.25-inch diameter geopolymer cylinders ranged from 1889 to 2136 psi with an average of 2013 psi. This strength range represents 47% to 53% with an average of 50% of regular construction grade concrete having a 28-day design compressive strength of 4000 psi.
- Measured Poisson's ratio for the geopolymer ranged from 0.12 to 0.27.
- 29-day flexural strength of the geopolymer beams ranged from 290 to 292 psi.

The following summarizes the results of the mineralogical analyses.

- XRF analyses indicate that the slag and fly ash are rich in CaO, SiO_2 and Al_2O_3 with the following percent composition:

	Slag	Fly Ash
CaO	43%	22%
SiO_2	33%	40%
Al_2O_3	15%	19%

- The major crystalline compounds of the geopolymer and the ingredients detected using XRD are summarized below.

Material	Primary Crystalline Compounds
Slag	Calcium sulfate and calcium sulfate hydrates
Fly ash	Silicon dioxide and calcium oxide
Basalt	Anorthite sodian, augite and iron magnesium oxide
Geopolymer	Calcite, aragonite and anorthite sodian

XRD cannot detect amorphous compounds such as calcium alumino-silicate if present in the slag or calcium silicate hydrate if present in the geopolymer.

- XRD results indicate that the slag and fly ash are amorphous or glassy as characterized by the presence of a low gentle hump in the XRD signature. However, the basalt sand and aggregate obtained from the island of Hawaii for this work are completely crystallized (not glassy or amorphous), consisting of common basaltic minerals such as plagioclase, pyroxene and iron magnesium oxide. This is reinforced by the RGB images of the thin sections where there was no sign of reactivity at the border of the basalt and cementitious matrix.
- Calcium, silicon and oxygen were detected in the cementitious matrix via EDS. These results suggest the presence of a calcium silicate hydrate with calcite or aragonite in the mix.

The following are the overall conclusions:

1. The slag and fly ash contain amorphous compounds with low and gentle humps observed in the XRD signature.
2. The basalt sand and aggregate are crystalline since there was no hump in their XRD signatures. It should be noted that the basalt was obtained one

ridge over from the PTA. The basalt from the actual PTA site should be studied in a similar manner as this one.

3. Based on the SEM images, there was little or no reaction between the crystalline basalt aggregate and the cementitious matrix. Typically, there is also no such reaction occurring in Portland cement concrete either. Should such a reaction occur, it is possible that it could be alkali-silica-reaction (ASR), which is highly undesirable as it can compromise the later strength of the geopolymer
4. Based on the L.A. abrasion test, the basalt aggregate had L.A. abrasion values that meet HDOT specification requirements for basalt used in concrete mixes. Therefore, the basalt aggregate is of reasonably high quality.
5. The 28-day geopolymer unconfined compressive strengths average about 2000 psi. Whether this is satisfactory depends on the weight and frequency of vehicles using the road as well as the thickness of the improved basalt.

CHAPTER 7. REFERENCES

Bijen J, Waltje H. "Alkali activated slag-fly ash cements. Fly ash, Silica fume, Slag and Natural Pozzolans in Concrete. Proceedings of the Third International Conference, Trondheim, Norway (1989) SP114-76 (1989), p 1566-78.

Davidovits, J. (2008) "Geopolymer Chemistry and Applications." *Institut Geopolymere,* 2nd Ed.

Fournier, B. (2010) "Alkali-Aggregate Reactions in Concrete: Types of Reactions, Testing of Aggregate and Methods of Prevention – A Review." *52th Brazilian Concrete Congress,* Fortaleza, Ceara, Brazil, October, 2010.

Kosmatka, S.H.; Kerkhoff, B. and Panarese, W.C. (2002) "Design and Control of Concrete Mixtures." *Portland Cement Association,* EB001, 14th edition, Skokie, Illinois, USA.

Kumar, S., Kumar, R. and Mehrotra, S.P. (2009) "Influence of granulated blast furnace slag on the reaction, structure and properties of fly ash based geopolymer." *Springer Science + Business Media,* Vol. 45: 607-615, October.

Norrish K. and Chappell B.W. (1977) *X-ray fluorescence spectrometry, in Physical Methods in Determinative Mineralogy*, 2nd Ed., J. Zussman, ed., 201-272, Academic Press, London.

Puertas, F. and Fernandez-Jimenez, A. (2003) "Mineralogical and Microstructural Characterization of Alkali-Activated Fly Ash/Slag Pastes." *Cement & Concrete Composites,* Vol. 25, No. 3, 287-292.

Puertas F., Martinez-Ramirez S., Alonso S. and Vazquez T. (2000). Alkali-activated fly ash/slag cements. Strength behavior and hydration products. *Cement and Concrete Research*; Vol. 12(8): 1625-1632.

Reed, S.J.B. (1993) "Electron Microprobe Analysis." *Press Syndicate of the University of Cambridge*, ed., 2nd, Cambridge University Press.

Shi, C., Krivenko, P. and Roy, D. (2006) "Alkali-Activated Cements and Concretes." *Taylor and Francis*.

Scintag, Inc. (1999) "Chapter 7:Basics of X-Ray Diffraction." California, USA, pp. 4-10, www.scintag.com.

Smith MA, Osborne GJ. “Slag/fly ash cements.” *World Cement Technology* 1977:223-33

State of Hawaii Department of Transportation Highways Division. (2005). "Hawaii Standard Specifications for Road and Bridge Construction.

U.S. Department of Transportation. “Portland Cement Concrete Testing Manual.” *Federal Highway Administration*. http://isddc.dot.gov/OLPFiles/FHWA/013716.pdf.

Ward, C. and French, D. (2005) “Relation between Coal and Fly Ash Mineralogy, Based on Quantitative X-Ray Diffraction Methods.” *2005 World of Coal Ash (WOCA),* April 11-15, 2005, Lexington, Kentucky, USA.

Wirth, K., & Barth, A. (2012, February 16). *Geochemical Instrumentation and Analysis*. Retrieved May 5, 2012, from Integrating Research and Education: http://serc.carleton.edu/research_education/geochemsheets/techniques/XRF.html

CHAPTER 8. APPENDIX

Pictures of the failed beams and cylinders are presented herein.

BEAMS

Figure 57. Beam 1

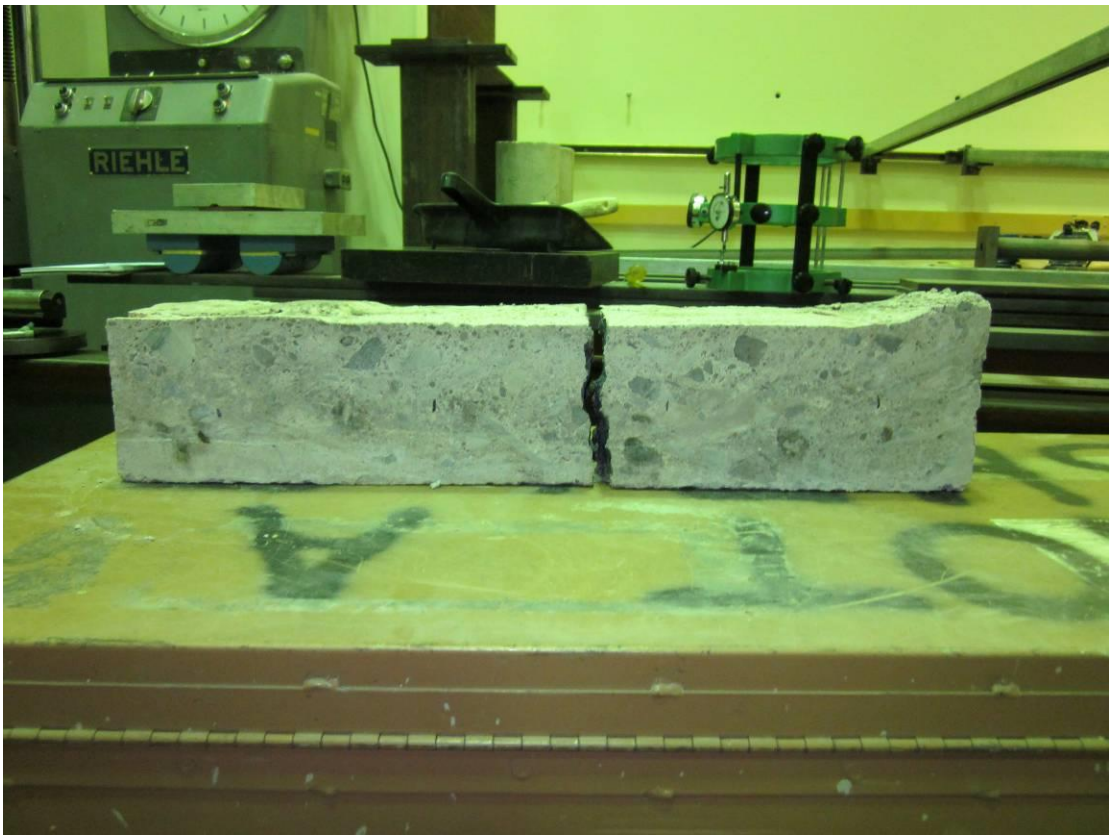

Figure 58. Beam 2

Figure 59. Beam 3

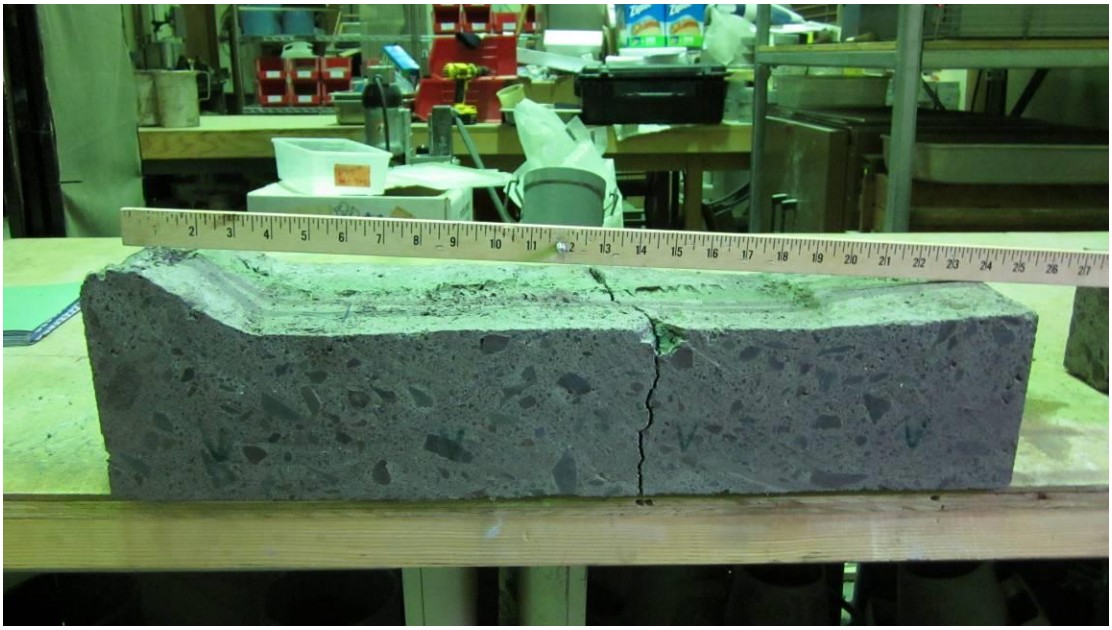

Figure 60. Beam 4

Figure 61. Beam 5

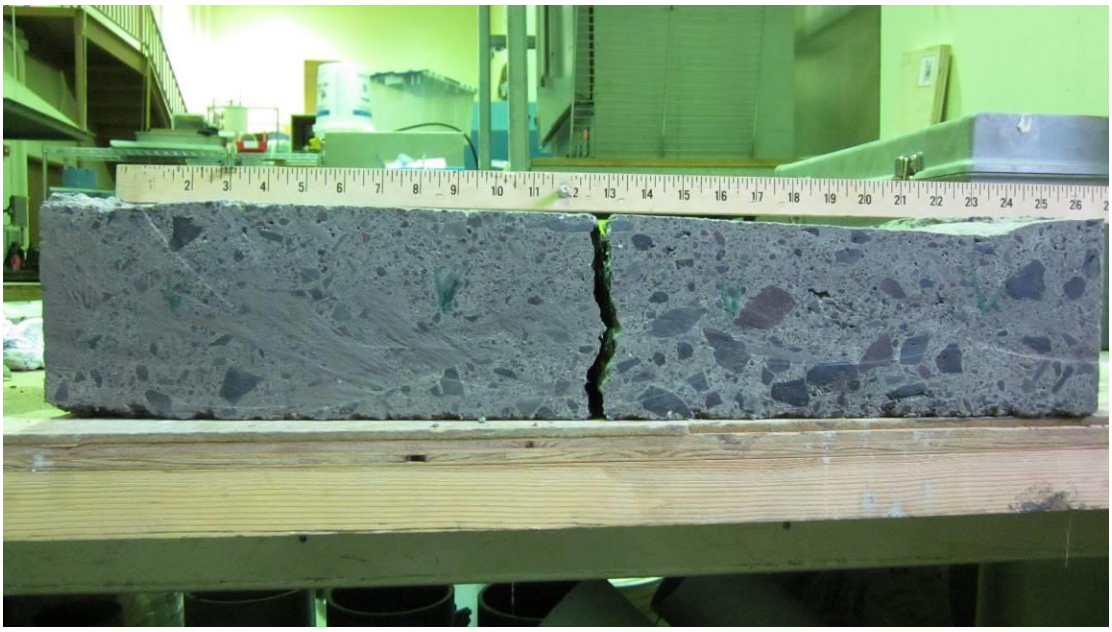

Figure 62. Beam 6

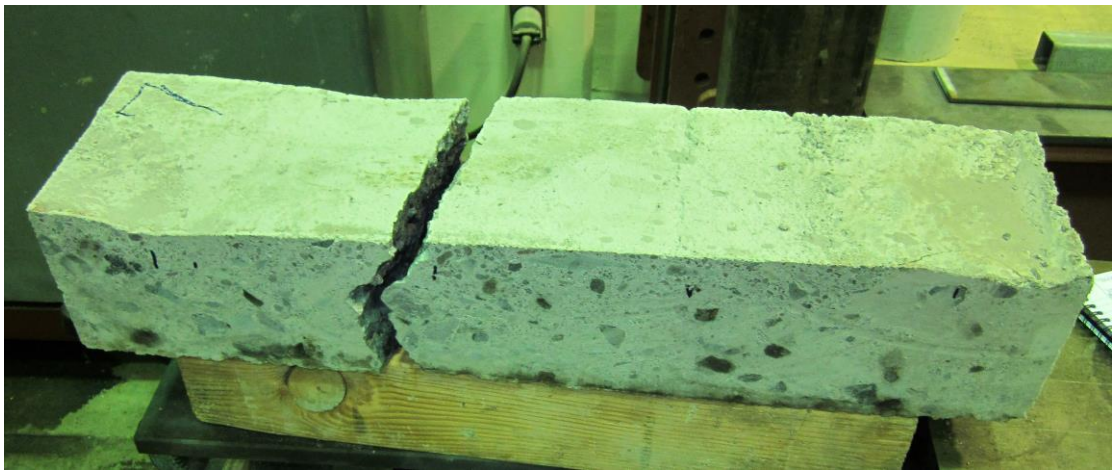

Figure 63. Beam 7

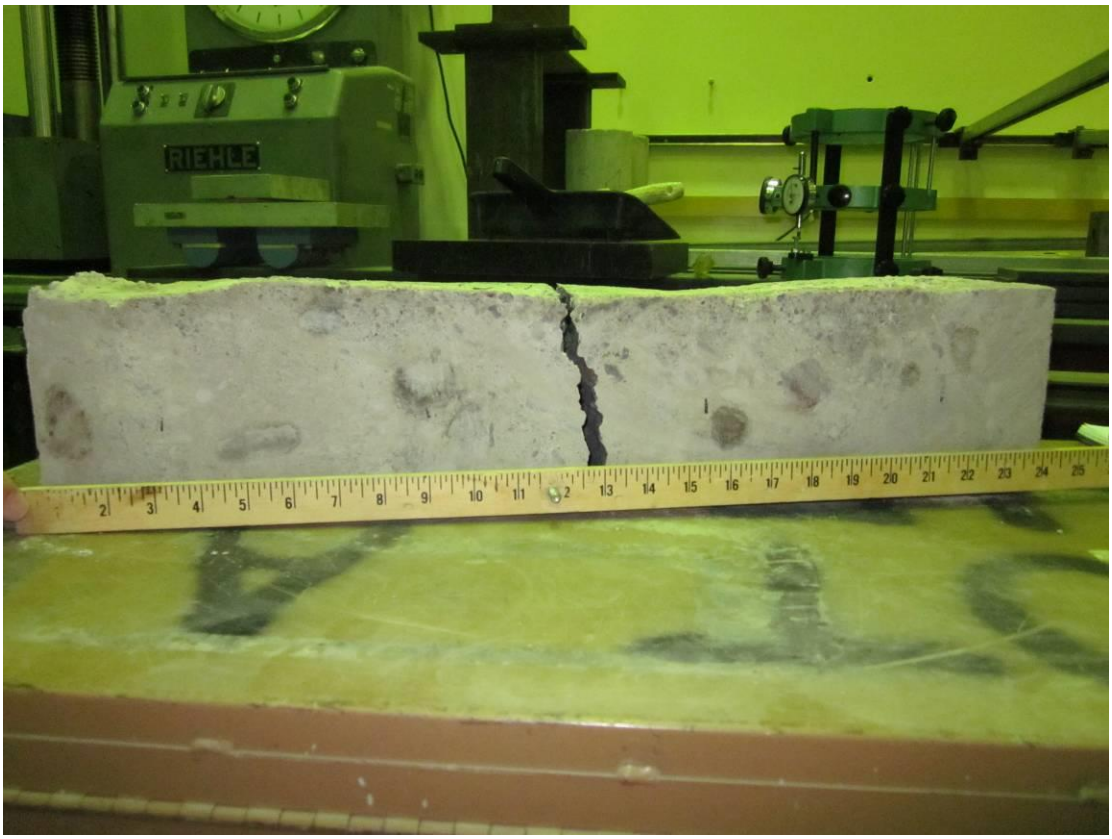

Figure 64. Beam 8

2.25-INCH-DIAMETER CYLINDERS

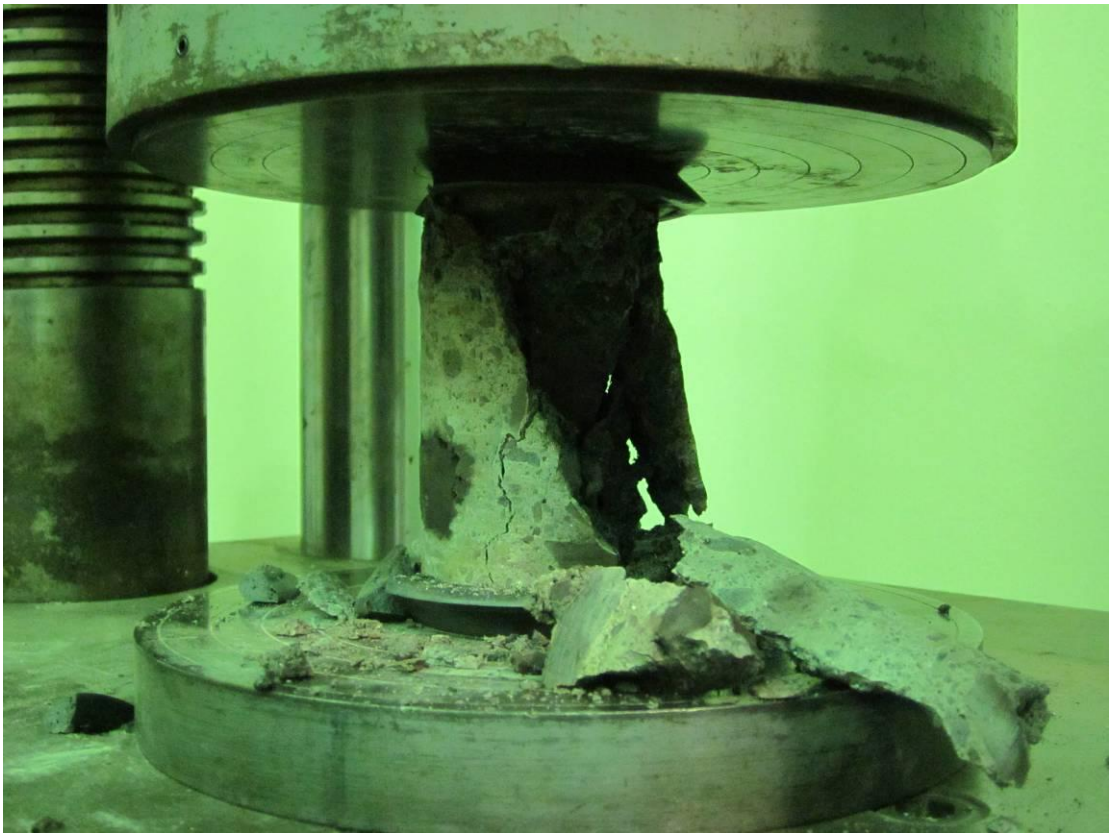

Figure 65. 2.25-inch-diameter Cylinder 1

Figure 66. 2.25-inch-diameter Cylinder 2

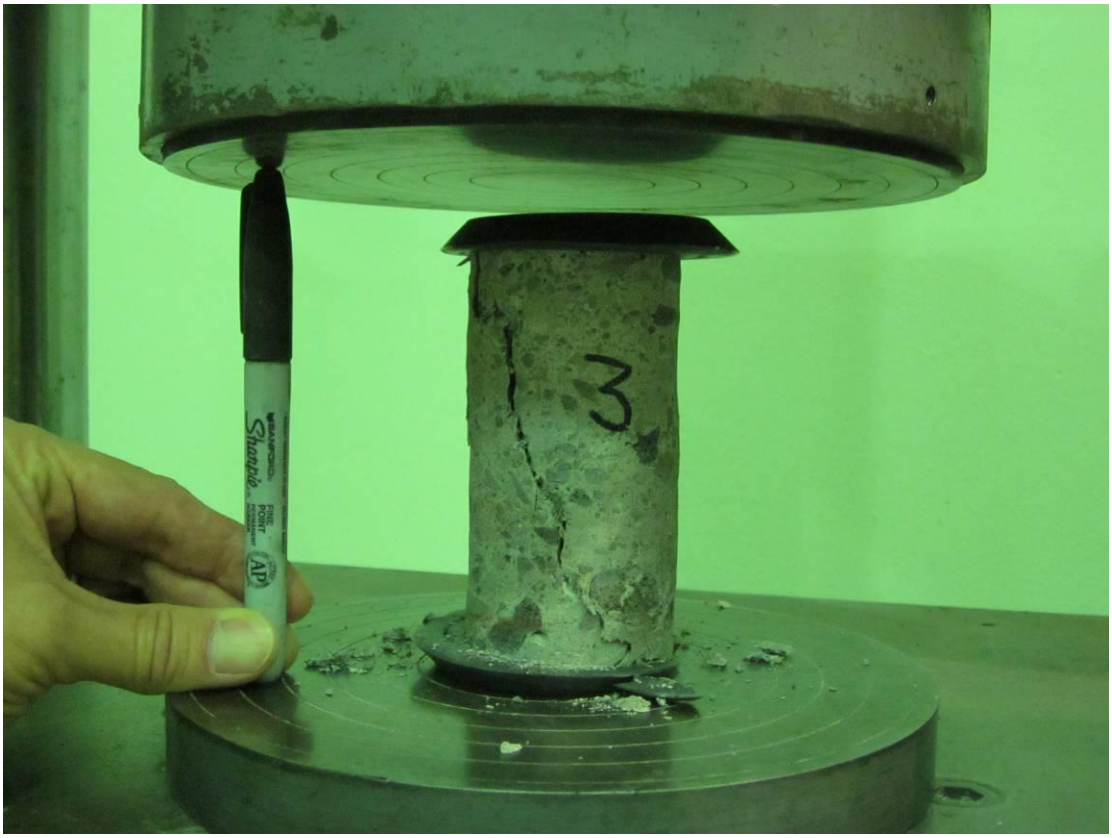

Figure 67. 2.25-inch-diameter Cylinder 3


Figure 68. 2.25-inch-diameter Cylinder 4

Figure 69. 2.25-inch-diameter Cylinder 5

Figure 70. 2.25-inch-diameter Cylinder 6

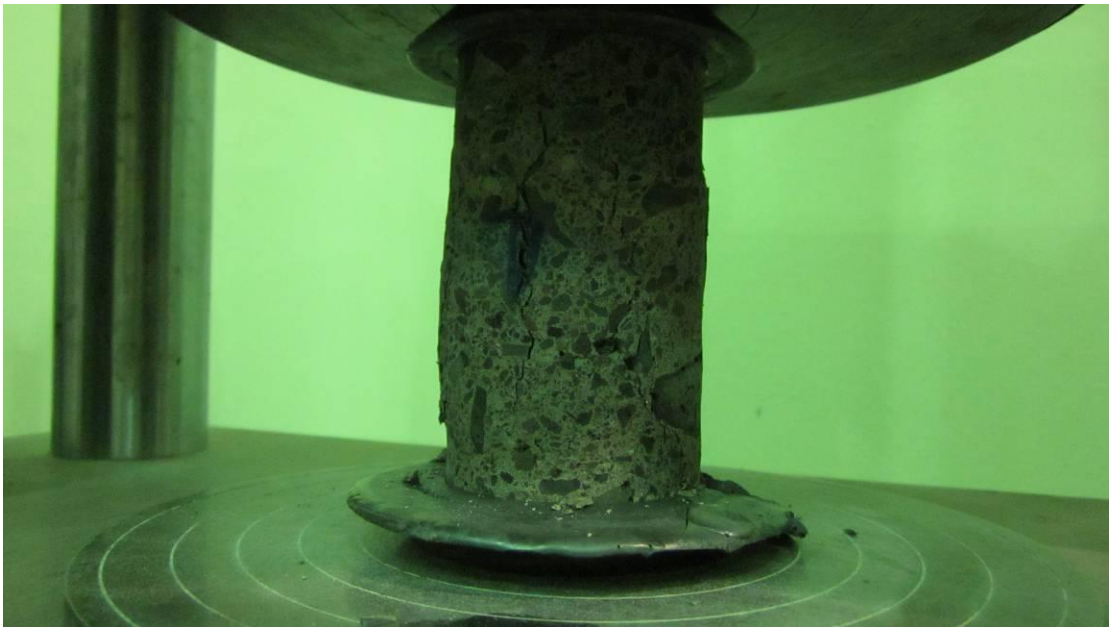

Figure 71. 2.25-inch-diameter Cylinder 7

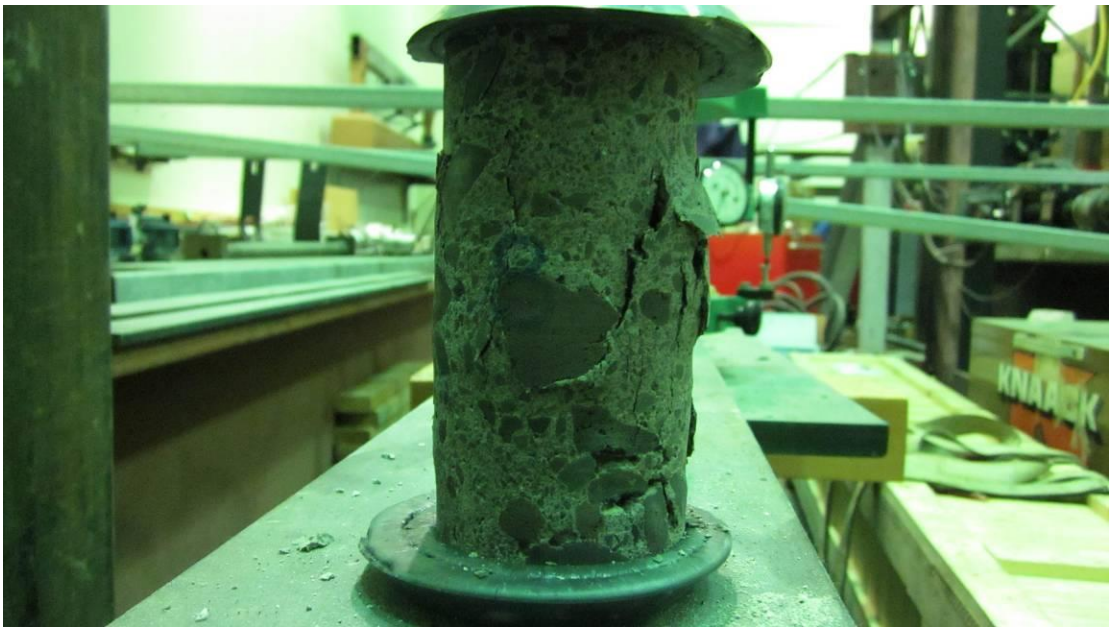

Figure 72. 2.25-inch-diameter Cylinder 8

6-INCH-DIAMETER CYLINDERS

Note: Pictures for cylinders 7, 8 and 9 are not available.

Figure 73. 6-inch-diameter Cylinder 1

Figure 74. 6-inch-diameter Cylinder 2

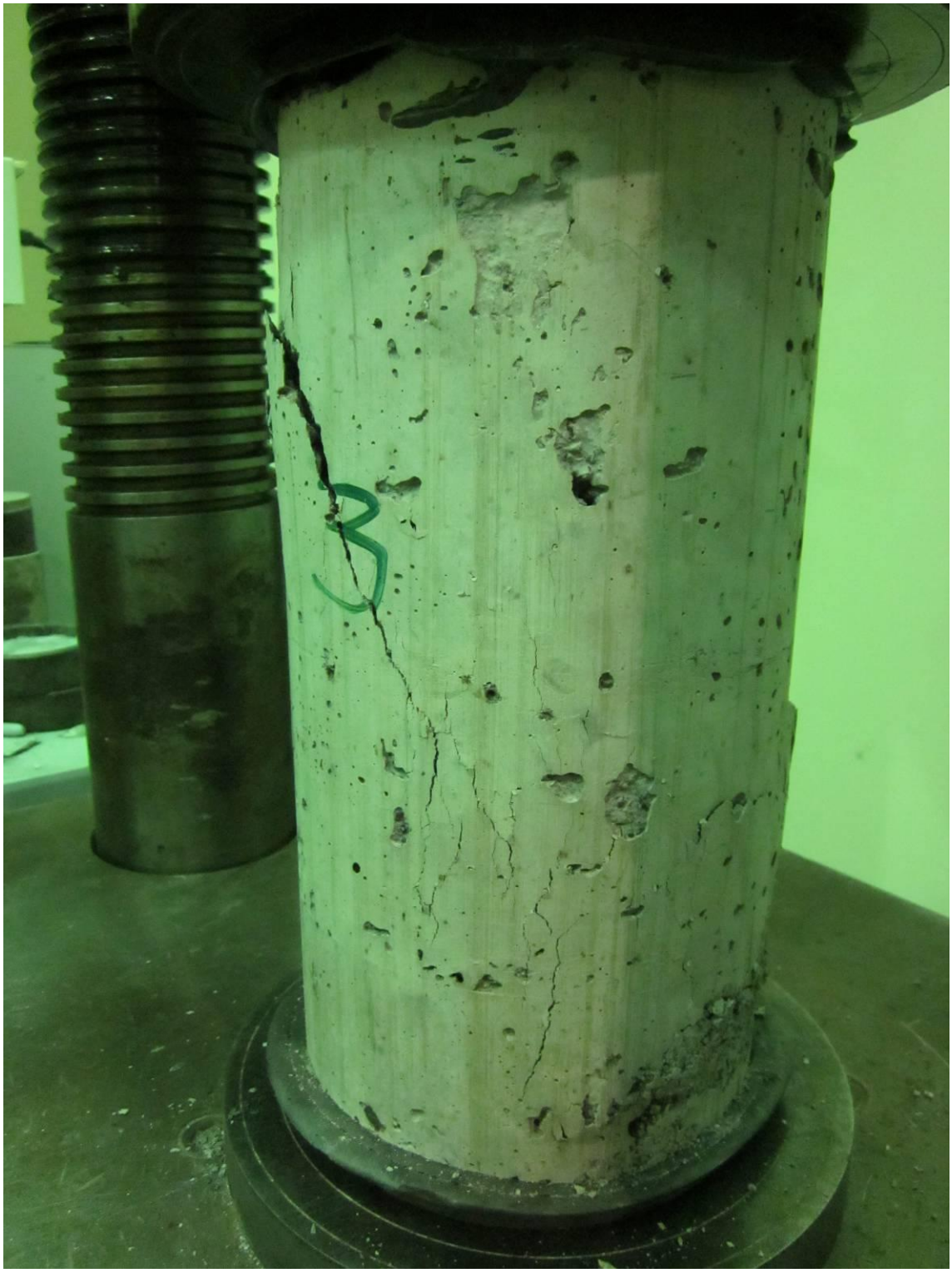

Figure 75. 6-inch-diameter Cylinder 3

Figure 76. 6-inch-diameter Cylinder 4

Figure 77. 6-inch-diameter Cylinder 5

Figure 78. 6-inch-diameter Cylinder 6

Figure 79. 6-inch-diameter Cylinder 10

Figure 80. 6-inch-diameter Cylinder 11

Figure 81. 6-inch-diameter Cylinder 12

REPORT DOCUMENTATION PAGE

Form Approved
OMB No. 0704-0188

1. REPORT DATE *(DD-MM-YYYY)*	2. REPORT TYPE	3. DATES COVERED *(From - To)*
April 2018	Final	

4. TITLE AND SUBTITLE

Laboratory Investigation of Natural Cementation Road Surfacing for Corrosion Control of Aluminum on Army Vehicles: Contractor's Supplemental Report for Project F10-AR06

5a. CONTRACT NUMBER
W9132T-09-2-0022

5b. GRANT NUMBER

5c. PROGRAM ELEMENT NUMBER

6. AUTHOR(S)
Phillip S.K. Ooi and Michelle K. Coskey

5d. PROJECT NUMBER

5e. TASK NUMBER

5f. WORK UNIT NUMBER

7. PERFORMING ORGANIZATION NAME(S) AND ADDRESS(ES)
University of Hawai'i at Manoa
Department of Civil and Environmental Engineering
2540 Dole Street
Honolulu, HI 96822

8. PERFORMING ORGANIZATION REPORT NUMBER

9. SPONSORING / MONITORING AGENCY NAME(S) AND ADDRESS(ES)
U.S. Army Engineer Research and Development Center
Construction Engineering Research Laboratory
P.O. Box 9005
Champaign, IL 61826-9005

10. SPONSOR/MONITOR'S ACRONYM(S)
ERDC-CERL

11. SPONSOR/MONITOR'S REPORT NUMBER(S)
ERDC/CERL CR-18-1

12. DISTRIBUTION / AVAILABILITY STATEMENT
Approved for public release; distribution is unlimited.

13. SUPPLEMENTARY NOTES

14. ABSTRACT

The Department of Defense (DoD) operates a massive fleet of ground vehicles in many corrosive environments. Rutting and erosion of unpaved roadways in training areas damage vehicles and contribute to dust brownouts. Moisture, soil, and grit deposits on surfaces and undercarriages accelerate corrosion and increase maintenance requirements. These problems could be greatly mitigated by advanced road stabilization materials and practices. A geopolymer material was studied for demonstration and validation on unpaved military roads at Pohakuloa Training Area (PTA), HI, under DoD Corrosion Prevention and Control Project F10-AR06. To support that work, the University of Hawai'i at Manoa performed a series of laboratory tests to characterize the geopolymer and its constituent materials, such as fly ash and slag, and the resulting cementitious material when blended with lime, soda ash, basalt aggregate, and water.

Material characterization and mechanical testing was performed to characterize the basalt aggregate. Geopolymer mechanical properties were then characterized in unconfined compression and four-point bending tests. Microstructural and mineralogical characteristics of the constituents and geopolymer were characterized using x-ray fluorescence, scanning electron microscopy with energy dispersive spectroscopy, and x-ray diffraction. The 28-day geopolymer unconfined compressive strengths averaged about 2,000 psi and the modulus of rupture averaged about 290 psi.

15. SUBJECT TERMS
Dirt roads–Dust control; Soil stabilization; Basalt; Vehicles, Military; Aluminum–Corrosion; Geopolymers

16. SECURITY CLASSIFICATION OF:			17. LIMITATION OF ABSTRACT	18. NUMBER OF PAGES	19a. NAME OF RESPONSIBLE PERSON
a. REPORT	b. ABSTRACT	c. THIS PAGE			19b. TELEPHONE NUMBER *(include area code)*
Unclassified	Unclassified	Unclassified	UU	132	